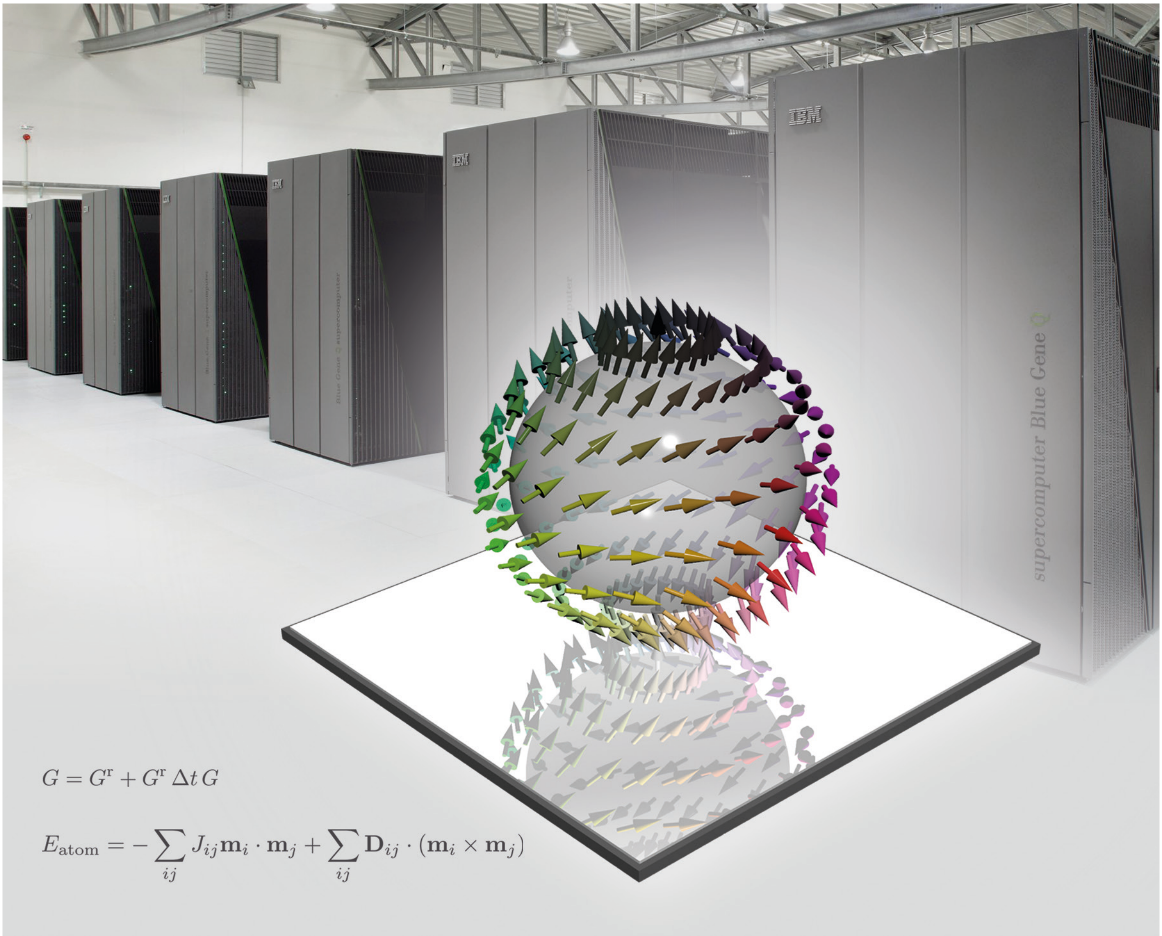

Large-scale Investigations of Non-trivial Magnetic Textures in Chiral Magnets with Density Functional Theory

Marcel Bornemann

Schlüsseltechnologien / Key Technologies
Band / Volume 195
ISBN 978-3-95806-394-5

Mitglied der Helmholtz-Gemeinschaft

JÜLICH
Forschungszentrum

Schriften des Forschungszentrums Jülich
Reihe Schlüsseltechnologien / Key Technologies Band / Volume 195

Forschungszentrum Jülich GmbH
Peter Grünberg Institut (PGI)
Quanten-Theorie der Materialien (PGI-1/IAS-1)

Large-scale Investigations of Non-trivial Magnetic Textures in Chiral Magnets with Density Functional Theory

Marcel Bornemann

Schriften des Forschungszentrums Jülich
Reihe Schlüsseltechnologien / Key Technologies Band / Volume 195

ISSN 1866-1807 ISBN 978-3-95806-394-5

Bibliografische Information der Deutschen Nationalbibliothek.
Die Deutsche Nationalbibliothek verzeichnet diese Publikation in der Deutschen Nationalbibliografie; detaillierte Bibliografische Daten sind im Internet über http://dnb.d-nb.de abrufbar.

Herausgeber und Vertrieb: Forschungszentrum Jülich GmbH
Zentralbibliothek, Verlag
52425 Jülich
Tel.: +49 2461 61-5368
Fax: +49 2461 61-6103
zb-publikation@fz-juelich.de
www.fz-juelich.de/zb

Umschlaggestaltung: Grafische Medien, Forschungszentrum Jülich GmbH

Druck: Grafische Medien, Forschungszentrum Jülich GmbH

Schriften des Forschungszentrums Jülich
Reihe Schlüsseltechnologien / Key Technologies, Band / Volume 195

D 82 (Diss., RWTH Aachen University, 2019)

ISSN 1866-1807
ISBN 978-3-95806-394-5

Abstract

The large-scale Density Functional Theory (DFT) code KKR`nano` allows one to perform *ab initio* simulations for thousands of atoms. In this thesis an extension of KKR`nano` is presented and utilized which facilitates the investigation of exotic non-collinear magnetic textures in bulk materials on huge length scales. Such an undertaking inevitably involves the utilization of High Performance Computing (HPC) which is itself a scientific field. The work in this context includes the adaptation of new coding paradigms and the optimization of codes on constantly changing hardware architectures. In KKR`nano`, the runtime of a simulation scales linearly with the number of atoms due to an advanced Korringa-Kohn-Rostoker (KKR) scheme that is applied, in which the sparsity of the matrices in the multiple-scattering equations is exploited. This enables us to investigate phenomena that occur on a length scale of nanometers involving thousands of atoms.

The main purpose of this thesis was to generalize the KKR formalism in KKR`nano` in such a way that a non-collinear alignment of the atomic spins can be treated. In addition to this, the relativistic coupling of spin and orbital degrees of freedom, which arises from the Dirac equation, was introduced to the code. This coupling gives rise to the Dzyaloshinskii-Moriya interaction (DMI) from which the formation of non-collinear magnetic textures usually originates. Other methodological features that were added to KKR`nano` or were re-established in the context of this thesis are the Generalized Gradient Approximation (GGA), Lloyd's formula and a semi-core energy contour integration. GGA is known to be a better approximation to the exchange-correlation energy in DFT than the still very popular Local Density Approximation (LDA), Lloyd's formula allows to determine the charge density exactly, despite the angular momentum expansion of all quantities, and the semi-core energy contour integration facilitates the treatment of high-lying electronic core states. Furthermore, an experimental port of the multiple-scattering solver routine to Graphics Processing Unit (GPU) architectures is discussed and the large-scale capabilities of KKR`nano` are demonstrated by benchmark calculations on the supercomputer JUQUEEN that include more than 200.000 atoms.

The new version of KKR`nano` is used to investigate the magnetic B20 compounds B20-MnGe and B20-FeGe as well as alloys of B20-$\text{Mn}_{1-x}\text{Fe}_x\text{Ge}$ type with varied concentration of Mn and Ge. These compounds are well-known for exhibiting helical states. Recently reported observations of topologically protected magnetic particles, also known as skyrmions, make them promising candidates for future spintronic devices. Initially, the known pressure-induced transition from a high-spin to a low-spin state in B20-MnGe is reproduced with KKR`nano` and an examination of the magnetocrystalline anisotropy yields unexpected results. Different non-collinear magnetic states are then

analyzed with both an extended Heisenberg model Hamiltonian and KKR`nano`. The parameters for the model Hamiltonian are extracted with the KKR method. The advantage of such a model is that micromagnetic quantities can be derived from it, which provide information on the helical wavelength of a magnetic texture, and that the Curie temperature can be estimated from the isotropic model parameters. Furthermore, the model parameters can be fed into an Atomistic Spin Dynamics (ASD) simulation package. The subsequent simulations show that skyrmions and anti-vortices are metastable in B20-MnGe. The calculations with KKR`nano` lead to the conclusion that helical states are stable in B20-MnGe, if the chosen lattice parameter is larger than the experimentally reported one.

Contents

Conventions and Abbreviations

In this thesis, we try to stick to the following conventions in mathematical expressions:

Symbol		Explanation
$\vec{r}$	arrow head	3-dimensional vector (containing Cartesian components)
$\hat{r}$	hat	normalized 3-dimensional vector
$\underline{c}$	underline	general vector
$\underline{\underline{M}}$	double underline	general matrix
$\mathcal{S}$	calligraphic symbol	operator (in basis-independent form)

The following abbreviations are used:

Abbr.	Meaning
ASA	Atomic Sphere Approximation
ASD	Atomistic Spin Dynamics
AVX	Intel's Advanced Vector Extensions
bcc	Body-centered Cubic
BCP	Block-circulant Preconditioning
BG/Q	IBM Blue Gene/Q Supercomputer
BLAS	Basic Linear Algebra Subprograms
BP	Bloch Point
CPA	Coherent Potential Approximation
CPU	Central Processing Unit
DDR-RAM	Double Data Rate Dynamic Random Access Memory
DMI	Dzyaloshinskii-Moriya Interaction
DRAM	Dynamic Random-access Memory
ES	Electrostatics
ESSL	IBM's Engineering and Scientific Subroutine Library

Abbr.	Meaning
ESSLSMP	Multi-threaded ESSL
fcc	Face-centered Cubic
FLOP	Floating Point Operation
FM	Ferromagnetic
FP	Full Potential Calculation
FPU	Floating Point Unit
GEA	Gradient-expansion Approximation
GGA	Generalized Gradient Approximation
GMRES	Generalized Minimal Residual Method
GNEB	Geodesic Nudged Elastic Band Method
GPFS	IBM General Parallel File System
GPU	Graphics Processing Unit
HPC	High Performance Computing
IEEE	Institute of Electrical and Electronics Engineers
KKR	Korringa-Kohn-Rostoker
KNL	Intel's Knights Landing CPU
LDA	Local Density Approximation
LLG	Landau-Lifshitz-Gilbert Equation
LSD	Local Spin Density Approximation
LSGF	Locally Self-consistent Green Function Method
LSMS	Locally Self-consistent Multiple Scattering
MA	Magnetocrystalline Anisotropy
MCE	Magnetocrystalline Anisotropy Energy
MCDRAM	Multi-Channel DRAM
MPI	Message Passing Interface
MPS	Multi-process Service for GPUs
OpenMP	Open Multi-Processing
PAC	Linear Algebra Package
QMR	Quasi-Minimal Residual Algorithm
RAM	Random-access memory
RKKY	Ruderman-Kittel-Kasuya-Yosida Interaction
SIMD	Single Instruction, Multiple Data
SMT	Simultaneous Multithreading
SOC	Spin-orbit Coupling
SRA	Scalar Relativistic Approximation
TB-KKR	Tight-binding Korringa-Kohn-Rostoker Method
TD-DFT	Time-dependent DFT
TFQMR	Transpose-Free Quasi-Minimal Residual Algorithm
VCA	Virtual Crystal Approximation
WS	Wigner-Seitz Cell

1

Introduction

The origin of modern solid state physics dates back to the 20s and the beginning of the 30s of the last century. This period of time is characterized by remarkable progress that was made with regards to the theoretical description of matter. Fundamentally new physical concepts were introduced that constituted the emergent field of *quantum mechanics*. Erwin Schrödinger and Paul Dirac derived equations that describe the motion of elementary particles while taking into account their inherent wave-particle duality [1, 2]. Felix Bloch extended this concept to crystal lattices [3]. Their work and the work of others laid the ground that enabled scientists to commence exploring the rich quantum theory of materials. The fundamental problem in quantum mechanics has always been the exponentially increasing computational complexity of finding solutions to its equations. The advent of quantum computing could potentially provide the means to circumvent this problem in the future [4]. A solid consists of a huge number of atoms. In view of the fact that solving the quantum mechanical problem for solids has been and still is out of reach, schemes were devised that reduce the computational complexity while not sacrificing too much of the quantum mechanical nature of the problem at hand. The density functional formalism, which is part of this effort and the foundation stone of this thesis, was first suggested by Hohenberg and Kohn in 1964 [5] and its importance to the field of quantum chemistry can hardly be overestimated. Walter Kohn became a Nobel laureate in chemistry for his work in 1998 and today almost 20.000 scientific publications per year are related to Density Functional Theory (DFT) in one way or another [6]. The areas of application of DFT range from the calculation of band-gaps to molecular dynamics [7, 8] and magnetic materials. A large section of contemporary research, as well as the work that is presented in this thesis, revolves around the latter.

In 1988 Grünberg and Fert independently discovered the giant magnetoresistance effect in magnetic layers [9, 10]. This gave rise not only to an unimagined increase of hard disk storage capacity but also sparked a new field of research that is called *spintronics*. In this context much emphasis was recently put on the investigation of novel magnetic phases in solids. For instance, spin spirals with a unique rotational sense were first predicted theoretically and later observed in experiment [11, 12]. Even more promising in terms of application potential are skyrmionic textures. The term *skyrmion* traces back to the British physicist Tony Skyrme [13], who proposed a concept of topologically protected particles, i.e. they cannot be annihilated by a continuous deformation, to explain hadrons in nuclear physics. However, it turned out that such particles can also be found in chiral magnets [14–16]. In the medium term, skyrmions are the most promising candidates for serving as information carriers in nanoscale spintronic devices, although there still lie many challenges ahead, e.g. achieving functionality at room temperature [17]. The fact that the functionality of memory devices is at the center of much of today's fundamental research in many fields can be ascribed to the ever increasing global need for data storage. By the year 2025 this need is predicted to add up to 163 zettabytes, i.e. a trillion gigabytes [18]. Fulfillment of this demand will become increasingly difficult with present-day technology, even if additional optimizations can, at least to some degree, further increase data density in devices. Hence, some new ideas are here needed.

The work that was done during the formation process of this thesis is two-fold: It comprised method development in the context of DFT and the application of DFT and atomistic spin dynamics (ASD) codes to shed light on the origins of exotic magnetic phases in solids. At the centre of the former stands the first principles DFT code KKR`nano` which was designed to allow a linearly scaling treatment of up to a million atoms [19]. In this project, technology of today, i.e. state-of-the-art supercomputers, is exploited to pave the way for future innovations in materials science. A main aspect of the work that was done in the context of this thesis was to extend KKR`nano` in such a way that the investigation of non-collinear magnetism in conjunction with spin-orbit coupling effects becomes feasible. This is a prerequisite for examining materials that have the chiral magnetic properties to host skyrmionic textures. An undertaking like this necessarily takes place at the interface of physics and computational science as in every work step both aspects regarding physical accuracy and computational performance need to be taken into consideration. With the advent of exascale computing, super large-scale simulations that have been deemed impossible before, will soon be within reach [20]. In order to be granted sufficient computing time from leading supercomputing facilities for such projects, great emphasis must be put on adjusting the code to the local hardware. The hardware components can differ substantially between different machines, and it is to be ensured that the provided resources are used efficiently. The current standard method to simulate systems containing thousands of magnetic spins is ASD. It is based on a strong simplification of the physical description, i.e. the quantum mechanical many-body Hamiltonian is replaced by a spin Hamiltonian that only includes the most prominent magnetic interactions. An approach based on first principles, as implemented in KKR`nano`, represents by construction a more comprehensive description and is therefore superior to the ASD method, if ground state properties are to be investigated. Nevertheless, it is instructive to compare results obtained with both methods as first principles calculations for large systems are costlier in terms of required computational resources. A calculation featuring a few thousand magnetic atoms with ASD can easily be conducted on a laptop while a similar calculation with KKR`nano` is only feasible on supercomputers. A well-working

ASD model that yields results which are similar to a DFT calculation should therefore not be discarded but used for counterchecking the DFT results as it is done in the context of this thesis. Apart from KKR`nano`, the juKKR code [21, 22] was used for extracting atomistic model parameters and the SPIRIT code [23] was used for ASD simulations.

The materials that are central to the work presented in the following are the noncentrosymmetric B20 compounds, namely the B20 germanides MnGe and FeGe as well as alloys of the form $\mathrm{Mn}_{1-x}\mathrm{Fe}_x\mathrm{Ge}$. The lack of inversion symmetry in their crystal structure gives rise to spin-orbit coupling effects, a requirement for the existence of most chiral magnetic textures [24]. The first observation of skyrmions in any material was made by Mühlbauer et al. in the B20 compound MnSi in 2009 [15]. Both B20-MnGe and B20-FeGe feature a relatively broad helical phase with a magnetic ordering temperature of $T_C = 170$ K [25] and $T_C = 278$ K [26], respectively, which makes them interesting materials for room-temperature memory devices. Furthermore, there seems to be a prevalence for exotic novel magnetic phases in them. In a recent theoretical and experimental investigation of thin films of B20-FeGe, a new type of localized particle-like object, named the *chiral bobber*, was discovered [27]. In another study for B20-MnGe, experimentalists found by means of transmission electron microscopy that bulk samples exhibit a cubic lattice of skyrmions with a very short period of $\approx$ 3 nm [28]. This is a length scale which can be treated by KKR`nano` which is why B20-MnGe, out of all B20 materials, is in the focus of our attention. Especially for B20-MnGe, the physical origin of the observed chiral textures is still under debate. While some experts in the field attribute their existence to the competition between ferromagnetic interaction and Dzyaloshinskii-Moriya interaction [29], others emphasize Ruderman–Kittel–Kasuya–Yosida (RKKY) interaction, i.e. magnetic frustration, as a key factor [30]. It was the aim of this PhD project to develop the necessary tools that can throw light on such unsolved questions.

The thesis is structured in the following manner:

In **Chapter 2** the concepts behind Density Functional Theory (DFT) are introduced. The Hohenberg-Kohn theorems, which form the basis of DFT, are given and the essential Kohn-Sham equation is derived. This is followed by an explanation of spin-dependent DFT that is vital to the treatment of magnetic materials and a brief description of how exchange-correlation effects are approximated in DFT.

Chapter 3 builds upon this and serves to introduce the Korringa-Kohn-Rostoker (KKR) method as a Green function-based DFT formalism. Its essential attribute is the rigid distinction between the *single-site scattering problem* and the *multiple-site scattering problem*. Furthermore, important methodological achievements that have been accomplished in Jülich and are utilized in KKR`nano`, e.g. the full-potential screened KKR treatment, are discussed. The chapter concludes with a recipe for obtaining a self-consistent solution for the Kohn-Sham potential which is the main variational quantity in our scheme. Understanding the KKR formalism is crucial in order to apprehend what distinguishes KKR`nano` from other DFT codes.

In **Chapter 4** a thorough explanation of KKR`nano` and its linear-scaling capabilities is given. Another topic that is extensively covered is the optimization of KKR`nano` for High Performance Computing (HPC). Different homogeneous and heterogeneous hardware architectures are discussed and the parallelization scheme used in KKR`nano` is explained. GPUs are destined to become the backbone of future HPC architectures and HPC research in this field is therefore of high importance. As part of this PhD project KKR`nano` was equipped with an extension that allows to solve the multiple-scattering problem on a GPU. Performance results as well as architecture-related challenges are elaborated on in the corresponding section. A detailed performance analysis on the supercomputer JUQUEEN in Jülich allows to demonstrate KKR`nano`'s linear-scaling behaviour but also reveals potential computational bottlenecks. Finally, other methodological improvements that were added to KKR`nano` are discussed. These are the newly added support for the more elaborate GGA exchange-correlation functionals, the re-established Lloyd's formula for exact charge densities and a special treatment of semi-core states, which can neither be attributed to the group of valence states nor to the group of core states.

A major part of this PhD project was the implementation of non-collinear magnetism in conjunction with relativistic effects in KKR`nano`. The algebraic concepts behind these extensions are presented in **Chapter 5** and the calculation of the magnetocrystalline anisotropy energy of $\mathrm{IrMn_3}$ is given as an example to illustrate the enhanced understanding of magnetic effects which a non-collinear relativistic simulation can provide. Finally, methodological improvements that were added to KKR`nano` are discussed. These are the newly added support for the more elaborate GGA exchange-correlation functionals, the re-established Lloyd's formula for exact charge densities and a special treatment of semi-core states, which can neither be attributed to the group of valence states nor to the group of core states.

Chapter 6 is intended to be a brief introduction to the concept of atomistic spin dynamics (ASD). The Landau-Lifshitz-Gilbert equation that describes the precession of an atomic magnetic moment in a magnetic field is derived and the constituents of the extended Heisenberg model are discussed. Subsequently, it is shown how these constituents, in particular the isotropic exchange term and the Dzyaloshinskii-Moriya interaction term, can be extracted from a KKR calculation.

The focus of **Chapter 7** is on the results that could be obtained with both the KKR and the ASD method for the non-noncentrosymmetric B20 materials. In this chapter the B20-MnGe and B20-FeGe compounds as well as B20-$\mathrm{Mn}_{1-x}\mathrm{Fe}_x\mathrm{Ge}$ alloys with a variable ratio of Mn and Fe are scrutinized. The known pressure-induced high-spin/low-spin transition of B20-MnGe [31] is confirmed in a KKR`nano` calculation. Furthermore, atomistic and micromagnetic parameters are extracted and analyzed. These parameters can be used in ASD simulations, where meta-stable skyrmionic objects are observed. KKR`nano` is utilized to investigate the energetics of different magnetic states, from the trivial ferromagnetic state to the complex 3D-hedgehog lattice. This investigation is then extended to layered systems and a generalization of the crystallographic space group. Subsequently, similar investigations are conducted for B20-FeGe and B20-$Mn_{1-x}Fe_xGe$ alloys.

2

Density Functional Theory

The point of departure in Density Functional Theory (DFT) is the recognition that the ground state of a system of electrons can be determined by the knowledge of the electron density distribution alone as shown by Hohenberg and Kohn in the 1960s. [5] They provided a proof for the assumption that the total energy in a quantum system exposed to an external potential is a unique functional of the electron density within the system. This built the foundation for a story of success which followed and has still not reached its peak, making DFT a widely-applied method for research in condensed matter physics and also in other fields, e.g. quantum chemistry [6].

Theoretically, DFT provides an exact solution of the quantum many-body problem, if there was an analytical form of the exchange-correlation potential. Since this is not the case, one must resort to approximate functionals like the Local Density Approximation (LDA) or the Generalized Gradient Approximation (GGA). More elaborate schemes apply many-body perturbation theory to extract certain physical quantities more precisely, e.g electron band gaps can be very precisely calculated by using the GW approximation.

A growing interest in non-collinear magnetic textures asks for the consideration of relativistic effects in DFT calculations which are derived from the Dirac equation. Indeed, primarily the inclusion of spin-orbit coupling has triggered a whole new field of physics ranging from e.g. anisotropy effects in ferromagnets or skyrmions to topological insulators that is investigated with the help of DFT codes [32].

This chapter is meant to reproduce the important constituents of DFT and follows the structure and derivations of other elaborations, in particular the ones by Thieß (cf. [33]) and Lounis (cf. [34]).

2.1. Born-Oppenheimer Approximation

Electronic structure methods often neglect the kinetic energy contribution of the atomic nuclei to the Hamiltonian. In the Born-Oppenheimer approximation it is assumed that the slowly moving nucleus does not influence the electronic behavior because the electrons adjust their positions adiabatically according to the nucleus' movement. Thus the electronic problem and the nuclear problem can be separated due to their inherently different timescales. In low-temperature physics, where phononic interactions do not need to be taken into account, lattice vibrations are neglected completely and the fixed nuclei contribute to the Hamiltonian solely via their electromagnetic potential [35]. In the following all notations are given in atomic units ($\hbar = 1$; $m_e = \frac{1}{2}$; $e^2 = 2$; energies in Rydberg , $1Ry = 13.6058$ eV; lengths in units of Bohr radii)

2.2. Hohenberg-Kohn Theorems

There are two theorems called the Hohenberg-Kohn theorems that lay the foundation for DFT calculations [5]. The associated proofs can be taken from the literature, e.g. [32]. Both theorems draw a connection between the energy functional $E\left[n\right]$ of a quantum many-body system and the spatial electron density $n\left(\vec{r}\right)$ in it.

Theorem 1 *For a given external potential V, the total energy of a system is a unique functional of the ground state electron density $n_0\left(\vec{r}\right)$*

If the ground state is not degenerate, it hence follows that all properties of the system of interest are determined by the ground state density $n_0\left(\vec{r}\right)$. In particular the calculation of individual wave functions is not necessary.

Theorem 2 *The exact ground state density $n_0\left(\vec{r}\right)$ minimizes the energy functional $E\left[n\left(\vec{r}\right)\right]$*

This would allow one to minimize the energy functional depending on the electron density, if there was a known exact functional. In the following it is explained why there is no such practical functional [36] and how nonetheless reasonable approximations can facilitate an analytical treatment.

2.3. Kohn-Sham Equation

Kohn and Sham suggested to write the total energy of the many-body problem as a sum of contributions of non-interacting electrons [37]. The energy functional written in terms of the electron density has the form

$$\begin{aligned} E[n] &= T[n] + U[n] + V[n] \\ &= T_s[n] + U_H[n] + V[n] + E_{XC}[n] \\ &= T_s[n] + \int\int \frac{n(\vec{r})n(\vec{r}')}{|\vec{r}-\vec{r}'|} d\vec{r}d\vec{r}' + \int n(\vec{r})V_{ext}(\vec{r})d\vec{r} + E_{XC}[n], \end{aligned} \tag{2.1}$$

where

$$n(\vec{r}) = \sum_{i=1}^{N} \phi_i^*(\vec{r})\phi_i(\vec{r}) \quad \text{and} \quad T_s[n] = \sum_{i=1}^{N} \int \phi_i^*(\vec{r}) \left(-\nabla^2\right) \phi_i(\vec{r}) d\vec{r}.$$

The sum of kinetic energy $T[n]$, electron-electron interaction $U[n]$ and nuclear potential $V[n]$ is reformulated by introducing the kinetic energy of a non-interacting electron $T_s[n]$ and the Hartree electron-electron interaction term $U_H[n]$ that accounts for the Coulomb interaction. This approximation is made because the effect of the electron-electron interaction on the kinetic energy and the exchange and correlation effects in the Coulomb potential are difficult to determine. In order to compensate for this shortcoming the exchange-correlation functional $E_{XC}[n]$ is introduced. Here, the challenge is to find a functional only depending on the electron density n that can mimic contributions of quantum mechanical nature [38].

Now that the total energy functional has been derived we can apply Theorem 2. In order to ensure that the number of electrons remains constant the Lagrange constraint

$$\sum_i \epsilon_i \left(\int \phi_i^*(\vec{r})\phi_i(\vec{r}) d\vec{r} - 1\right) \tag{2.2}$$

is imposed, where the ϵ_i are Lagrange parameters. Here, the variational principle has the form

$$0 = \frac{\delta E[n]}{\delta n} = \frac{\delta E\left[\phi_i(\vec{r}), \phi_i^*(\vec{r})\right]}{\delta \phi_i^*(\vec{r})}. \tag{2.3}$$

If this is applied to eq. (2.1) with the additional constraint eq. (2.2), it yields the Kohn-Sham equations

$$\left(-\nabla^2 + V_{eff}[n]\right) \phi_i = \epsilon_i \phi_i, \tag{2.4}$$

where an effective potential is defined as

$$V_{eff}[n] = \int \frac{n(\vec{r}')}{|\vec{r} - \vec{r}'|} d\vec{r}' + V_{ext}(\vec{r}) + \frac{\delta E_{XC}[n]}{\delta n}. \tag{2.5}$$

Although eq. (2.4) has the form of a single-particle Schrödinger equation it describes the physics of a quantum many-body system under the approximations made above. Note, that both $\phi_i(\vec{r})$ and ϵ_i do not have a rigorously defined physical meaning although they are often interpreted as single-particle wave functions and single-particle excitation energies, respectively. Quantities in DFT are only well-defined if they are directly related to the electron density $n(\vec{r})$.

2.4. Spin Density Functional Theory

The inclusion of collinear magnetic effects requires the consideration of two spin channels in DFT calculations. Both spin channels then converge to different electron densities

$n^{\uparrow}(\vec{r})$ for spins polarized in positive z-direction and $n^{\downarrow}(\vec{r})$ for spins pointing in negative z-direction. These quantities can be used to define an electron and a magnetization density[39]

$$n(\vec{r}) = n^{\uparrow}(\vec{r}) + n^{\downarrow}(\vec{r}) \tag{2.6}$$

$$m(\vec{r}) = n^{\uparrow}(\vec{r}) - n^{\downarrow}(\vec{r}). \tag{2.7}$$

The generalization of the Kohn-Sham equation eq. (2.4) for collinearly spin polarized systems reads

$$\left(-\nabla^2 + V^{\sigma}_{eff}[n]\right)\phi^{\sigma}_i = \epsilon^{\sigma}_i \phi^{\sigma}_i \tag{2.8}$$

which can be solved independently for both spin channels $\sigma = \{\uparrow, \downarrow\}$.

While a collinear treatment of magnetizations is sufficient for ferromagnetic systems, more sophisticated compounds can show non-collinear magnetic behavior, i.e. atomic spins point in arbitrary directions and not only along a clearly defined z-axis. In non-collinear spin DFT the scalar magnetization density is replaced by a vectorial magnetization density $\vec{m}(\vec{r})$. Both $n(\vec{r})$ and the newly defined $\vec{m}(\vec{r})$ may be expressed by the 2x2 spin density matrix $n^{\alpha\beta}(\vec{r})$, where α and β can have the directions $\uparrow$ or $\downarrow$:

$$n(\vec{r}) = \sum_{\alpha} n^{\alpha\alpha}(\vec{r}) \qquad \vec{m}(\vec{r}) = \sum_{\alpha\beta} \vec{\sigma}^{\alpha\beta} n^{\alpha\beta}(\vec{r}) \tag{2.9}$$

Here, the Pauli matrices $\vec{\sigma}^{\alpha\beta} = \left(\sigma^{\alpha\beta}_x, \sigma^{\alpha\beta}_y, \sigma^{\alpha\beta}_z\right)$ are used. Inversely, the spin density matrix can be written in terms of the electronic density and the vector of the magnetization density as

$$n^{\alpha\beta}(\vec{r}) = \frac{1}{2}\left(n(\vec{r})\delta^{\alpha\beta} + m_x(\vec{r})\sigma^{\alpha\beta}_x + m_y(\vec{r})\sigma^{\alpha\beta}_y + m_z(\vec{r})\sigma^{\alpha\beta}_z\right). \tag{2.10}$$

The spin-dependent energy functional

$$E[n^{\alpha\beta}(\vec{r})] = T_s[n^{\alpha\beta}(\vec{r})] + \int\int \frac{n(\vec{r})n(\vec{r}')}{|\vec{r} - \vec{r}'|} d\vec{r} d\vec{r}' \tag{2.11}$$

$$+ \sum_{\alpha\beta} \int n^{\alpha\beta}(\vec{r}) V^{\alpha\beta}_{ext}(\vec{r}) d\vec{r} + E_{XC}[n^{\alpha\beta}(\vec{r})] \tag{2.12}$$

is defined analogously to eq. (2.1) but with spin density depended kinetic energy, external potential and exchange-correlation energy. Kinetic energy functional and spin-density matrix in the single-particle scheme read

$$T_s[n^{\alpha\beta}(\vec{r})] = \sum_{i,\alpha} \int \phi^{*\alpha}_i(\vec{r}) \left(-\nabla^2\right) \phi^{\alpha}_i(\vec{r}) d\vec{r} \tag{2.13}$$

and

$$n^{\alpha\beta}(\vec{r}) = \sum_i \phi^{*\alpha}_i(\vec{r}) \phi^{\beta}_i(\vec{r}). \tag{2.14}$$

The considerations above lead to the non-collinear Kohn-Sham equations

$$-\nabla^2\phi_i^{\alpha}(\vec{r}) + \sum_{\beta} V_{eff}^{\alpha\beta}(\vec{r})\phi_i^{\alpha\beta}(\vec{r}) = \epsilon_i\phi_i^{\alpha}(\vec{r}), \tag{2.15}$$

where the effective potential is defined as

$$V_{eff}^{\alpha\beta}(\vec{r}) = \delta^{\alpha\beta}\int \frac{n(\vec{r}')}{|\vec{r}-\vec{r}'|}d\vec{r}' + V_{ext}^{\alpha\beta}(\vec{r}) + V_{XC}^{\alpha\beta}(\vec{r}). \tag{2.16}$$

It is noteworthy that the two spin channels α and β are separated in all terms except for the external potential term $V_{ext}^{\alpha\beta}$ and the exchange-correlation term $E_{XC}[n^{\alpha\beta}(\vec{r})]$.

2.5. Exchange-correlation Potential

It should be stressed that in the derivation of the total energy functional eq. (2.1) no approximations are introduced and the expression is exact. The remaining task is to find an expression for the exchange-correlation potential $E_{XC}[n]$ in which non-local effects are combined. This is where DFT needs to resort to approximative functionals since an exact expression in terms of the electronic density is not known. Such functionals can be of arbitrary complexity but it has turned out that for the majority of applications the local density approximation (LDA) or the slightly more elaborate generalized gradient approximation (GGA) suffice. On average these approximations yield considerably better results than the well-known Hartree approximation, where $E_{XC}[n]$ is completely neglected.

In the spin-polarized regime LDA is denoted local spin density approximation (LSD). Here, the exchange-correlation energy reads

$$E_{XC}^{LSD} = \int n(\vec{r})\epsilon_{XC}^{hom}\left(n^{\uparrow}(\vec{r}), n^{\downarrow}(\vec{r})\right) d\vec{r}, \tag{2.17}$$

where the exchange-correlation functional ϵ_{XC}^{hom} is obtained from a quantum Monte-Carlo simulation of a homogeneous electron gas. While LSD requires only the electronic density $n(\vec{r})$ as an input parameter GGA functionals additionally utilize the gradient of the electronic density

$$E_{XC}^{GGA} = \int f(n^{\uparrow}(\vec{r}), n^{\downarrow}(\vec{r}), \nabla n^{\uparrow}(\vec{r}), \nabla n^{\downarrow}(\vec{r}))d\vec{r}. \tag{2.18}$$

There are numerous expressions for the functional f, e.g. PBE [40], PBEsol [41], PW91 [42] or B3LYP [43] are among the most popular. The search for more precise approximations to the exchange-correlation energy itself constitutes a large area of research. For some materials advanced schemes like the GW approximation [44] yield more accurate results than LDA and GGA. However, such a gain in accuracy is associated with increasing computational complexity an lack of physical clarity.

3

KKR-Green Function Method

The Korringa-Kohn-Rostoker (KKR) method was introduced in 1947 by Korringa [45] and in 1954 by Kohn and Rostoker [46]. Its characteristic feature is that it divides the solution of the Schrödinger equation into a *single scattering problem* which is given by a single potential in free space and a *multiple scattering problem* which is based on the precept that the incoming wave at a scattering site is the sum of the outgoing waves from all other scattering centers.

KKR was initially proposed as a wave function scheme but soon reinvented as a Green function method [47] that brings along significant advantages, e.g. a complex energy contour integration that drastically improves the method's efficiency. As will be shown in this chapter, knowledge of the Green function of a specific system allows to extract a range of physical quantities and it is therefore very well justified to center the method around it.

The KKR scheme has been applied very successfully to systems with impurities in a host crystal and to randomly disordered alloys by means of the coherent potential approximation (KKR-CPA) [48]. Both efficiency and accuracy were further refined by the introduction of the so-called screened or tight-binding KKR method [49] that ensures an exponential decay of the multiple scattering components and therefore allows to cut them off at a rather short range without any loss of accuracy.

This chapter reproduces established knowledge and is based on earlier work that can for instance be found in [21, 22, 33, 50, 51]. First, a brief introduction to Green functions is given followed by an explanation of how to extract physical quantities from them by using a complex contour integration based on the recapitulation of Zimmermann (cf. [50]). Hereafter, the separation into single-site and multiple-scattering problems is discussed (cf. [50]). The chapter concludes with the full-potential treatment in KKR, a description of the screened KKR method and the presentation of a workflow scheme on how to solve the KKR equations self-consistently following the remarks of Thieß (cf. [33]).

3.1. Properties of Green Functions

Green functions in differential equations

The concept of Green functions was introduced to the field of linear partial differential equations by the mathematician George Green. A Green function $G(x,x',z)$ is defined as a solution of

$$(z-L)G(x,x',z)=\delta(x-x'), \tag{3.1}$$

where L is a linear differential operator, z is a real or complex scalar parameter and $\delta(x-x')$ is the Dirac delta function. If the respective Green function $G(x,x',z)$ is known, the inhomogeneous differential equation

$$(z-L)f(x)=h(x) \tag{3.2}$$

can be solved by evaluating

$$f(x)=f_0(x)+\int dx'G(x,x',z)h(x'). \tag{3.3}$$

This expression is formed by a solution $f_0(x)$ of the homogeneous differential equation (eq. (3.2) with $h(x)=0$) and a convolution integral of the Green function and the inhomogeneity. In the following Green functions are utilized to solve the quantum many body problem by means of the KKR method.

Green functions in physics

In quantum mechanics an electron exposed to a time-independent potential is described by the Hamiltonian

$$\mathcal{H}=-\nabla^2+V(\vec{r}), \tag{3.4}$$

where the first term describes the kinetic energy and the second term a potential that depends on the position of the electron. For simplicity $\hbar=1$, $m_e=\frac{1}{2}$ and $e=\sqrt{2}$ is assumed from here on. The Hamiltonian $\mathcal{H}$ is a differential operator for which the stationary Schrödinger equation must be fulfilled so that for a Green function $G(E)$

$$(E-\mathcal{H})\,G(E)=1 \tag{3.5}$$

holds. This procedure is analogous to eq. (3.1). The solution can be obtained in a straightforward manner as $G(E)=(E-\mathcal{H})^{-1}$. Naturally, it is also possible to solve this problem by obtaining the eigenstates ψ_i of eq. (3.4). Therefore, both approaches are closely connected which manifests in the so-called spectral representation of the Green function

$$G^{\pm}(E)=\sum_i\frac{|\psi_i\rangle\langle\psi_i|}{E-\epsilon_i\pm i\gamma} \tag{3.6}$$

Note, that an infinitesimal imaginary contribution $\gamma \to 0$ is added to the denominator to avoid singularities when $E = \epsilon_i$. Depending on the sign of γ the Green function is referred to as retarded (G^+) or advanced (G^-). In the following we exclusively use the retarded version. Equation (3.6) can then be generalized for real and spin space as

$$G^{\sigma,\sigma'}(\vec{r},\vec{r}',E) = \sum_i \frac{\psi_i^\sigma(\vec{r})\Big(\psi_i^{\sigma'}(\vec{r}')\Big)^\dagger}{E - \epsilon_i + i\gamma}, \tag{3.7}$$

where $\sigma \in \{\uparrow,\downarrow\}$, i.e. spin up or spin down.

Extraction of physical quantities

A convenient attribute of the Green function formalism is that observables A, which depend only on single particle properties, can be extracted from $G(E)$ by making use of the algebraic connection

$$\langle A \rangle = -\frac{1}{\pi}\mathrm{Im}\int_{-\infty}^{E_F} dE\,\mathrm{Tr}\left[A\,G(E)\right]. \tag{3.8}$$

The trace is integrated over the energy contour up to the Fermi level E_F of the electronic structure.

This allows to easily calculate the electronic density, the key ingredient to DFT, by defining the projection operator

$$P_{\vec{r}} = \sum_\sigma \left|\vec{r},\sigma\right\rangle \left\langle\vec{r},\sigma\right|, \tag{3.9}$$

which projects $G(E)$ onto a position $\vec{r}$. Putting $A = P_{\vec{r}}$ then leads to the spatially resolved electronic density

$$\rho(\vec{r}) = -\frac{1}{\pi}\mathrm{Im}\sum_\sigma \int_{-\infty}^{E_F} dE\, G^{\sigma,\sigma}(\vec{r},\vec{r},E) \tag{3.10}$$

A spin-resolved density of states for distinct energy points is given by

$$n^\sigma(\vec{r},E) = -\frac{1}{\pi}\mathrm{Im}G^{\sigma,\sigma}(\vec{r},\vec{r},E). \tag{3.11}$$

Complex energy contour

The extraction of an observable A from eq. (3.8) requires the evaluation of a semi-infinite integral over the energy E. This integral can be made finite by dividing it into a core electronic part ($-\infty < E < E_b$) and a valence electronic part ($E_b < E < E_F$) (see Figure 3.1). Conveniently, the core contribution that reaches up to the bottom of the valence band E_b can be evaluated in a simpler atomic-like formalism assuming

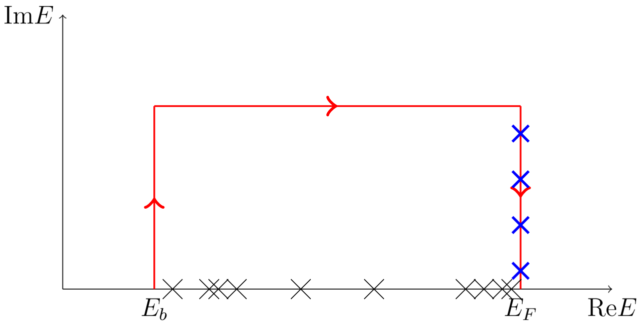

Figure 3.1.: Energy contour in complex plane as used for the integration in eq. (3.8) (red). The contour ranges from the bottom of the valence band E_b to the Fermi level E_F. The black crosses mark poles of the Green function on the real axis that are deliberately avoided by choice of the contour. Matsubara poles arising from the Fermi function are depicted with blue crosses.

that the charge density of the core states is fully localized within the individual cells. The contribution from the valence band is calculated by means of a complex contour integration, where the integration contour is shifted into the complex plane to avoid poles that the Green function defined in eq. (3.6) has on the real axis whenever $E = \epsilon_i$ [52]. Resorting to the complex plane also allows to use fewer points in the numerical integration (typically around 30) and therefore makes a calculation computationally less expensive. Additionally, the Green function is convoluted with the Fermi-Dirac distribution

$$f_T(E - E_F) = \frac{1}{1 + \exp\left((E - E_F)/k_B T\right)}, \tag{3.12}$$

where k_B is the Boltzmann constant and T an artificial electronic temperature which is usually set to a value between 200 and 800 K. This basically leads to a broadening of the density of states at the Fermi level. The Fermi-Dirac distribution leads to so-called Matsubara poles that are located where $E = E_F \pm (2n-1)\pi k_B T i$. Residual contributions from these poles need to be considered in the integration pattern, too. Convolution of the Fermi-Dirac distribution with eq. (3.8) yields

$$\langle A \rangle = -\frac{1}{\pi} \mathrm{Im} \int_{E_b}^{E_F} dE f_T(E - E_F) \mathrm{Tr}\left[A\, G(E)\right]. \tag{3.13}$$

Note, that $f_T(E - E_F)$ exponentially decays above the Fermi level E_F which allows to formally extend the integral to infinity. Observables, e.g. the electronic density, can be derived from this equation analogously to eq. (3.10) and eq. (3.11).

3.2. Single-Site Scattering

In the following it is explained how the propagation of a single electron in a finite potential can be described by a Green function. This is done by introducing the Green function for an electron in free space $g(\vec{r}, \vec{r}', E)$ followed by a derivation of the solution to the single-site scattering problem $G(\vec{r}, \vec{r}', E)$.

Free space

The Hamiltonian for an electron in free space reads $\mathcal{H}_0 = -\nabla^2$. The eigenfunctions to it are plane waves

$$\phi_{\vec{k}} = e^{i\vec{k}\cdot\vec{r}} = \sum_L 4\pi i^l j_l(\kappa r) Y_L(\hat{r}) Y_L(\hat{k}), \tag{3.14}$$

which can be expanded in spherical harmonics $Y_L(\hat{x})$ with Bessel function coefficients $j_l(x)$. $L = (l, m)$ serves as a combined index for both angular (l) and magnetic (m) quantum number. In order to keep notations compact we define $\kappa = |\vec{k}| = \sqrt{E}$, $r = |\vec{r}|$, $\hat{r} = \vec{r}/r$ and $\hat{k} = \vec{k}/\kappa$ The Green function corresponding to the problem given by $\mathcal{H}_0$ is known to be

$$g(\vec{r}, \vec{r}', E) = -\frac{1}{4\pi} \frac{e^{i\kappa|\vec{r}-\vec{r}'|}}{|\vec{r}-\vec{r}'|}. \tag{3.15}$$

It can again be expanded in spherical harmonics as

$$g(\vec{r}, \vec{r}', E) = \sum_L Y_L(\hat{r}) \frac{1}{rr'} g_l(r, r', E) Y_L(\hat{r}'), \tag{3.16}$$

where

$$g_l(r, r', E) = \kappa r r' j_l(\kappa r_<) h_l(\kappa r_>). \tag{3.17}$$

Here, $r_<$ denotes the smaller radius of r and r' and $r_>$ denotes the larger radius of r and r'. $h_l(x) = n_l(x) - i j_l(x)$ is the spherical Hankel function in which $n_l(x)$ is the spherical Neumann function. Note, that $h_l(x)$ does not enter in the expansion of the wave function eq. (3.14), where only the spherical Bessel functions $j_l(x)$ are included. The Hankel functions diverge as $h_l(x) \propto 1/x^{l+1}$ for $x \to 0$ and are needed to describe the divergence of the denominator in eq. (3.15). The spin-dependent Green function for free space is diagonal and reads

$$g^{\sigma\sigma'}(\vec{r}, \vec{r}', E) = \delta_{\sigma,\sigma'} g(\vec{r}, \vec{r}', E). \tag{3.18}$$

Atomic potential with finite range

The next step is to generalize the problem above to a scenario in which a potential V of finite range is added so that the Hamiltonian reads $\mathcal{H} = -\nabla^2 + V$. The potential is defined as

$$V^{\sigma\sigma'}(\vec{r},\vec{r}') = \begin{cases} \sum_{L,L'} \frac{1}{r^2} V^{\sigma\sigma'}_{LL'}(r) Y_L(\hat{r}) Y_{L'}(\hat{r}')\delta(r-r') & \text{, for } |\vec{r}| \leq R \\ 0 \quad \text{, for } |\vec{r}| > R \end{cases} \tag{3.19}$$

and expanded in spherical harmonics Y_L. It is given with an explicit dependency on both spatial parameters $\vec{r}$ and $\vec{r}'$. While this dependency can be replaced with the relative distance $|\vec{r}-\vec{r}'|$ in many cases it is indispensable, if e.g. spin-orbit interaction shall be incorporated. In this case the potential includes spatial derivatives which cannot be evaluated, if only $|\vec{r}-\vec{r}'|$ is known. However, for the following derivations we can assume $V^{\sigma\sigma'}(\vec{r},\vec{r}')$ to be local which is indicated by the δ-distribution in eq. (3.19). For an atomic potential of finite range the Green function reads

$$\mathring{G}^{\sigma\sigma'}(\vec{r},\vec{r}',E) = \sum_{LL'} Y_L(\hat{r}) \frac{1}{rr'} \mathring{G}^{\sigma\sigma'}_{LL'}(\vec{r},\vec{r}',E) Y_{L'}(\hat{r}') \tag{3.20}$$

with expansion coefficients

$$\begin{aligned} &\mathring{G}^{\sigma\sigma'}_{LL'}(\vec{r},\vec{r}',E) = \\ &\kappa \sum_{s,L''} \Big[\Theta(r'-r) R^{s\sigma'}_{LL''}(r,E) \bar{S}^{\sigma s}_{L''L'}(r',E) + \Theta(r-r') S^{\sigma s}_{LL''}(r,E) \bar{R}^{s\sigma'}_{L''L'}(r',E) \Big]. \end{aligned} \tag{3.21}$$

It consists of products of so-called *regular* ($R^{\sigma s}_{L'L}/\bar{R}^{\sigma s}_{L'L}$) and *irregular* ($S^{\sigma s}_{L'L}/\bar{S}^{\sigma s}_{L'L}$) solutions. Furthermore, it must be distinguished between *right* ($R^{\sigma s}_{L'L}/S^{\sigma s}_{L'L}$) and *left* ($\bar{R}^{\sigma s}_{L'L}/\bar{S}^{\sigma s}_{L'L}$) solutions.

All solutions can be obtained by using the Lippmann-Schwinger equation. It connects the wave functions of a perturbed and an unperturbed system

$$\mathcal{H}_0 \left|\psi_0\right\rangle = E \left|\psi_0\right\rangle \tag{3.22}$$

$$(\mathcal{H}_0 + \Delta V) \left|\psi\right\rangle = E \left|\psi\right\rangle \tag{3.23}$$

by the relation

$$\left|\psi\right\rangle = \left|\psi_0\right\rangle + G_0(E)\Delta V \left|\psi\right\rangle = \left|\psi_0\right\rangle + \int dr dr' g_l(r,r',E) V^{\sigma\sigma'}(\vec{r},\vec{r}') \left|\psi\right\rangle, \tag{3.24}$$

where the Green function for free space (eq. (3.17)) and the atomic potential with finite range (eq. (3.19)) are inserted. The expansion of $|\psi\rangle$ in spherical harmonics reads

$$\left|\psi\right\rangle = \psi^{\sigma}_{\vec{k},s}(\vec{r}) = \sum_{L,L'} 4\pi i^l \frac{1}{r} R^{\sigma s}_{L'L}(r,E) Y_L(\hat{k}) Y_{L'}(\hat{r}). \tag{3.25}$$

It must be distinguished between *right* and *left* solutions to a given operator equation. A *right* solution is defined as a solution to $(\mathcal{H}-E)\left|\psi\right\rangle = 0$ while a *left* solution solves $|\bar{\psi}\rangle(\mathcal{H}-E) = 0$.

A lengthy evaluation of eq. (3.24) [53] yields the regular *right* solution

$$R^{\sigma s}_{L'L}(r,E) = J_L(r,E)\delta_{L',L}\delta_{\sigma,s} + \sum_{\sigma'',L''} \int_{\text{cell}} dr'' g_{l'}(r,r'',E) V^{\sigma\sigma''}_{L'L''}(r'') R^{\sigma'' s}_{L''L}(r'',E) \tag{3.26}$$

formulated as a Lippmann-Schwinger equation. The interval in which the integral over r'' is evaluated depends on methodological approaches discussed in section 3.4. Analogously to free space an irregular *right* solution is given as

$$S^{\sigma s}_{L'L}(r,E) = H_L(r,E)\beta^{\sigma s}_{L'L}(E) + \sum_{\sigma'',L''}\int_{\text{cell}} dr'' g_{l'}(r,r'',E)V^{\sigma\sigma''}_{L'L''}(r'')S^{\sigma''s}_{L''L}(r'',E) \quad (3.27)$$

Note, that similarly to the potential-free case the regular solution contains a Bessel function while the irregular solution includes a Hankel function that diverges at the origin.

The *left* solutions can be derived in a similar manner and read

$$\bar{R}^{\sigma s}_{L'L}(r,E) = \delta_{L',L}\delta_{\sigma,s}J_{L'}(r,E) + \sum_{\sigma'',L''}\int_{\text{cell}} dr'' \bar{R}^{s\sigma''}_{LL''}(r'',E)V^{\sigma''\sigma}_{L''L'}(r'')g_{l'}(r'',r,E) \quad (3.28)$$

in the regular and

$$\bar{S}^{\sigma s}_{L'L}(r,E) = \bar{\beta}^{\sigma s}_{L'L}(E)H_{L'}(r,E) + \sum_{\sigma'',L''}\int_{\text{cell}} dr'' \bar{S}^{s\sigma''}_{LL''}(r'',E)V^{\sigma''\sigma}_{L''L'}(r'')g_{l'}(r'',r,E) \quad (3.29)$$

in the irregular form.

In our scheme the irregular solutions shall coincide with the Hankel functions outside the scattering region such that

$$S^{\sigma s}_{L'L}(r,E) = H_L(r,E)\delta_{L',L}\delta_{\sigma,s} \qquad \text{for } r > R. \quad (3.30)$$

The Hankel functions $H_L(r,E)$ in eq. (3.27) and eq. (3.29) are therefore multiplied with

$$\beta^{\sigma s}_{L'L}(E) = \delta_{L',L}\delta_{\sigma,s} - \kappa\int_{\text{cell}} dr' J_L(r',E)\sum_{\sigma'',L''}V^{\sigma\sigma''}_{L'L''}(r')S^{\sigma''s}_{L''L}(r',E) \quad (3.31)$$

and

$$\bar{\beta}^{s\sigma}_{LL'}(E) = \delta_{L,L'}\delta_{s,\sigma} - \kappa\sum_{\sigma'',L''}\int_{\text{cell}} dr' \bar{S}^{s\sigma''}_{LL''}(r',E)V^{\sigma''\sigma}_{L''L'}(r')J_{L'}(r',E), \quad (3.32)$$

respectively. This is to ensure the validity of eq. (3.30) and to impose correct boundary conditions.

Both Lippmann-Schwinger equations for $R^{\sigma s}_{L'L}(r,E)$ in eq. (3.26) and $\bar{R}^{\sigma s}_{L'L}(r,E)$ in eq. (3.28) can in most cases be solved up to sufficient accuracy by expanding them in a Born series. However, if spin-orbit coupling is included in the Hamiltonian, the Born series for the irregular solutions $S^{\sigma s}_{L'L}(r,E)$ (eq. (3.27)) and $\bar{S}^{\sigma s}_{L'L}(r,E)$ (eq. (3.29)) do not converge any longer. That is why a different approach was introduced by Zeller et al. [22] in which the radial dependency of the solutions is expanded in Chebyshev polynomials $T_n(x)$ as

$$f(x) = \sum_{j=0}^{\infty} a_j T_j(x), \tag{3.33}$$

where a_j are the expansion coefficients. Conveniently, the integral over $f(x)$ is again given by an expansion in Chebyshev polynomials as

$$F(x) = \int_{-1}^{x} f(x')dx' = \sum_{j=0}^{\infty} \beta_j T_j(x) \tag{3.34}$$

In practice, the summation is performed only for a finite number of polynomials $j = 0, .., N$. The coefficients a_j and β_j are connected by a matrix transformation of the form

$$\begin{pmatrix} \beta_0 \\ \beta_1 \\ \vdots \\ \beta_N \end{pmatrix} = \mathbf{S} \begin{pmatrix} \alpha_0 \\ \alpha_1 \\ \vdots \\ \alpha_N \end{pmatrix} \tag{3.35}$$

with the transformation matrix $\mathbf{S}$. This property of the Chebyshev expansion allows to write the Lippmann-Schwinger equations eqs. (3.26) to (3.29) as matrix equations that can be solved by matrix inversion. The procedure is described in detail in [22].

3.3. Multiple-Site Scattering

The derivations above exclusively considered single scattering sites. In a crystal structure multiple scattering sites at positions $\vec{R}_n$ $(n = 1, ..., N)$ must be taken into account. Due to the periodicity inherent to a crystal the Cartesian coordinates of the scattering centers can be written as a sum of cell-centered coordinates $\vec{R}_n$ and a local vector $\vec{r}$ that lies within the cell n,

$$\vec{x} = \vec{R}_n + \vec{r}. \tag{3.36}$$

In the following we first derive an expression for the electronic Green function in free space and then for a system of identical scatterers where we assume a site-diagonal potential

$$V^{nn'}(\vec{r} + \vec{R}^n, \vec{r}' + \vec{R}^{n'}) = \delta_{nn'} V^n(\vec{r}, \vec{r}') \tag{3.37}$$

with both arguments $\vec{r}$ and $\vec{r}'$ being confined to the same cell. A Dyson equation is formulated to obtain the associated Green function. Subsequently, the problem is extended to a system with multiple atoms in the unit cell.

Free space

The Green function for free space reads

$$g(\vec{x},\vec{x}',E) = \kappa \sum_{L} J_L(\vec{x}_<,E) H_L(\vec{x}_>,E) \tag{3.38}$$

As in eq. (3.16) the spin components are omitted. The conventions $J_L(\vec{x},E) = j_l(\sqrt{(E)}x)Y_L(\hat{x})$ and $H_L(\vec{x},E) = h_l(\sqrt{(E)}x)Y_L(\hat{x})$ denote products of spherical Bessel and Hankel functions with spherical harmonics. $\vec{x}_<$ ($\vec{x}_>$) is to be replaced by the shorter (longer) vector of $\vec{x}$ and $\vec{x}'$. Equation (3.38) can be transformed into the double expansion [54]

$$g(\vec{r}+\vec{R}^n,\vec{r}'+\vec{R}^{n'},E) = \delta_{nn'} g(\vec{r},\vec{r}',E) + \sum_{L=0}^{\infty} J_L(\vec{r},E) \sum_{L'=0}^{\infty} g_{LL'}^{nn'}(E) J_{L'}(\vec{r}',E). \tag{3.39}$$

This form features the cell-centered coordinates and allows to distinguish between the on-site part for which $n = n'$ (first term) and the multi-scattering part (second term). It is straightforward to confirm that eq. (3.39) is merely a different expression for eq. (3.38) [54]. With the help of the addition theorem

$$\kappa H_L(\vec{r}'+\vec{R}^n-\vec{R}^{n'},E) = \sum_{L'=0}^{\infty} g_{LL'}^{nn'} J_{L'}(\vec{r}') \tag{3.40}$$

the Hankel functions can be expanded in Bessel functions with expansion coefficients

$$g_{LL'}^{nn'}(E) = 4\pi\kappa \sum_{L''} i^{l-l'+l''} C_{LL'L''} H_{L''}(\vec{R}^n-\vec{R}^{n'}). \tag{3.41}$$

The integrals over three spherical harmonics

$$C_{LL'L''} = \int d\Omega\, Y_L(\hat{r}) Y_{L'}(\hat{r}) Y_{L''}(\hat{r}) \tag{3.42}$$

are called Gaunt coefficients. They vanish for $l'' > l' + l$ and thereby restrict the amount of terms which have to be considered in eq. (3.39) to a finite number. If the summations over L and L' are performed in the correct order (see [54] for details), eq. (3.39) is guaranteed to converge.

For magnetic particles the derivation above can be easily generalized with expansion coefficients

$$g_{\Lambda\Lambda'}^{nn'} = g_{LL'}^{nn'} \delta_{\sigma\sigma'}, \tag{3.43}$$

where $\Lambda = (L,\sigma) = (l,m,\sigma)$ is a combined angular momentum and spin index.

Dyson equation

The problem given by the potential in eq. (3.37) is solved by the Green function

$$G^{\sigma\sigma'}(\vec{r}+\vec{R}^n,\vec{r}'+\vec{R}^{n'},E)=\delta_{nn'}\mathring{G}^{\sigma\sigma'}(\vec{r},\vec{r}',E)+\sum_{\Lambda\Lambda'}R^{\sigma}_{\Lambda}(\vec{r},E)G^{nn'}_{\Lambda\Lambda'}(E)\bar{R}^{\sigma'}_{\Lambda'}(\vec{r}',E). \tag{3.44}$$

Its derivation is lengthy and therefore not discussed here [22]. $\mathring{G}^{\sigma\sigma'}$ is known from eq. (3.20) while R^{σ}_{Λ} and $\bar{R}^{\sigma'}_{\Lambda'}$ are given in eq. (3.26) and eq. (3.28), respectively. The so-called structural Green functions $G^{nn'}_{\Lambda\Lambda'}$ require further explanation. They are defined as

$$G^{nn'}_{\Lambda\Lambda'}(E)=g^{nn'}_{\Lambda\Lambda'}(E)+\sum_{n'',\Lambda'',\Lambda'''}g^{nn''}_{\Lambda\Lambda''}(E)t^{n''}_{\Lambda''\Lambda'''}(E)G^{n''n'}_{\Lambda'''\Lambda'}(E) \tag{3.45}$$

with the t-matrices

$$t^{n}_{\Lambda\Lambda'}(E)=\int d\vec{r}\int d\vec{r}'\,\bar{J}_{\Lambda}(\vec{r},E)V^{n}(\vec{r},\vec{r}')R^{n}_{\Lambda'}(\vec{r}',E) \tag{3.46}$$

which describe the transition of the wave function of an incoming electron to the wave function of an electron that is scattered at the potential $V^n(\vec{r},\vec{r}')$.
It is convenient to transform eq. (3.45) into reciprocal space which yields

$$G_{\Lambda\Lambda'}(\vec{k},E)=g_{\Lambda\Lambda'}(\vec{k},E)+\sum_{\Lambda'',\Lambda'''}g_{\Lambda\Lambda''}(\vec{k},E)t_{\Lambda''\Lambda'''}(E)G_{\Lambda'''\Lambda'}(\vec{k},E). \tag{3.47}$$

This approach exploits the periodicity that is inherent to a crystal structure which means that physical quantities can be derived solely from the relative position $\vec{R}_n-\vec{R}_{n'}$. While $t^{n}_{\Lambda''\Lambda'''}(E)$ does not depend on spatial coordinates, the single-site Green functions must also be transformed into Fourier space and are given as

$$g_{\Lambda\Lambda'}(\vec{k},E)=\sum_{n\neq n'}g^{nn'}_{\Lambda\Lambda'}(E)e^{i\vec{k}\cdot(\vec{R}^n-\vec{R}^{n'})}. \tag{3.48}$$

In order to obtain the structural Green function eq. (3.48) is inverted which provides

$$G_{\Lambda\Lambda'}(\vec{k},E)=\left[\left(\underline{\underline{1}}-\underline{\underline{g}}(\vec{k},E)\underline{\underline{t}}(E)\right)^{-1}\underline{\underline{g}}(\vec{k},E)\right]_{\Lambda\Lambda'}. \tag{3.49}$$

This equation constitutes the core of multiple-scattering theory in KKR. Usually, the inversion is performed directly. Under certain circumstances it can however be beneficial to use an iterative scheme as it is used in KKR`nano` (see section 4.1).
The result is transformed back to real space resulting in

$$G^{nn'}_{\Lambda\Lambda'}(E)=\frac{1}{V_{BZ}}\int_{BZ}d\vec{k}G_{\Lambda\Lambda'}(\vec{k},E)e^{-i\vec{k}\cdot(\vec{R}^n-\vec{R}^{n'})} \tag{3.50}$$

so that eq. (3.44) can be easily evaluated to obtain the Green function $G^{\sigma\sigma'}(\vec{r}+\vec{R}^n,\vec{r}'+\vec{R}^{n'},E)$ which solves the multiple-scattering problem.

A more general setting includes multiple atoms $\mu = 1...N_{at}$ in a unit cell with a different potential $V_{\mu}^{\sigma\sigma'}(\vec{r},\vec{r}')$ around each of them. The indices μ and μ' designate atoms within the unit cells n and n', respectively. The Fourier transformation in eq. (3.48) must then be generalized to

$$g_{\Lambda\Lambda'}^{\mu\mu'}(\vec{k},E) = \sum_{n \neq n'} g_{\Lambda\Lambda'}^{n\mu n'\mu'}(E) e^{i\vec{k}\cdot(\vec{R}^n - \vec{R}^{n'})} \tag{3.51}$$

and the form of the subsequent transformation back to real space changes to

$$G_{\Lambda\Lambda'}^{n\mu n'\mu'}(E) = \frac{1}{V_{BZ}} \int_{BZ} d\vec{k} G_{\Lambda\Lambda'}^{\mu\mu'}(\vec{k},E) e^{-i\vec{k}\cdot(\vec{R}^n - \vec{R}^{n'})}. \tag{3.52}$$

3.4. Full-potential Treatment

The spatial integrals $\int_{\text{cell}}$ in this chapter (e.g. eq. (3.26) and eq. (3.27)) are deliberately given without lower and upper boundaries. In the KKR methodology it must be distinguished between calculations that utilize the atomic sphere approximation (ASA) and full-potential (FP) calculations [21].
ASA is based on an approximation where the potential surrounding the scattering sites is considered to be spherical and thus all integrals can be evaluated in a straightforward manner by integrating up to a certain radius. This so-called Wigner-Seitz radius R_{WS} is chosen such that the volume of the unit cell coincides with the volume of the Wigner-Seitz sphere. A consequence of this procedure is that the different spheres overlap since their radii are larger than the touching radius, i.e. the so-called muffin-tin radius R_{MT}.
While ASA gives valid results for a variety of problems it is desirable to work with a scheme that utilizes non-spherical cells. Therefore, in the FP scheme the integrations are performed over the Wigner-Seitz (WS) cells of the individual scattering sites. The radius of the sphere that circumscribes the Wigner-Seitz cell is denoted by R_C. The radii R_{MT} and R_C are depicted in fig. 3.2.

For an FP calculation all spatial integrals $\int_{\text{cell}}$ in the formalism described in this chapter need to be convoluted with the shape function

$$\Theta(\vec{r}) = \sum_L \Theta_L(r) Y_L(\vec{r}) = \begin{cases} 1 & \text{inside WS cell} \\ 0 & \text{outside WS cell} \end{cases} . \tag{3.53}$$

It has the form of a step function expanded in spherical harmonics $Y_L(\vec{r})$ that masks regions outside the cell. The L-expansion converges rather slowly but it can be shown that only the radial shape functions $\Theta_L(\vec{r})$ for which $l \leq 4l_{max}$ contribute to the sum,

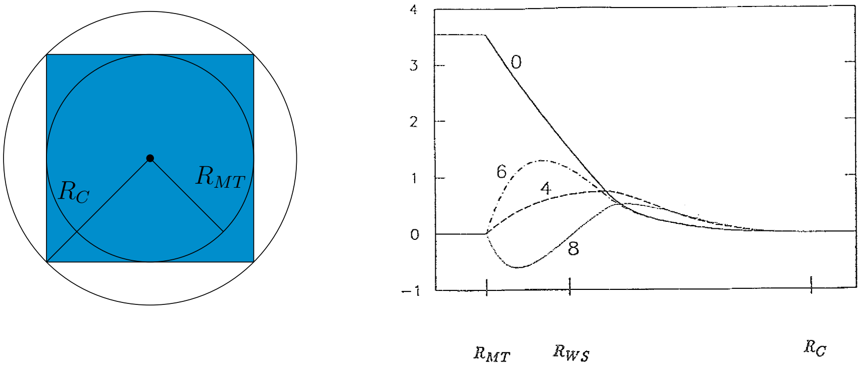

Figure 3.2.: Left: Illustration of a Wigner-Seitz cell (blue) with muffin-tin radius R_{MT} and circumscribing radius R_C. Right: Radial shape functions $\Theta_L(\vec{r})$ of an fcc lattice for $L = 0, 4, 6, 8$ with indicated muffin-tin radius R_{MT}, Wigner-Seitz radius R_{WS} and radius of the circumscribing sphere R_C. Reprinted from [55].

if the expansion of the wave functions is truncated above l_{max} [55]. The radial shape functions are given by

$$\Theta_L(r) = \begin{cases} \delta_{l,0}\sqrt{4\pi} & \text{, for } r \leq R_{MT} \\ 0 & \text{, for } r \geq R_C, \end{cases} \tag{3.54}$$

if r lies within the muffin-tin sphere or outside the circumscribing sphere. In between, the integral

$$\Theta_L(r) = \int d\Omega Y_L(\vec{r})\Theta(\vec{r}) \tag{3.55}$$

has to be evaluated numerically. Figure 3.2 illustrates how values from different L-components contribute to the expansion in eq. (3.53) for an fcc lattice.

3.5. Screened KKR Method

The screened KKR method was suggested by Zeller et al. as a scheme that allows the treatment of large-scale systems [49]. It is also known as tight-binding KKR method. The idea behind it is to replace the vanishing potential of free space, which is used as reference system above, by a constant muffin-tin potential on all sites. The muffin-tin potential leads to an exponential spatial decay of the structural constants (c.f. eq. (3.47)) and is an essential step towards a linear-scaling KKR algorithm (see chapter 4).
This exponential decay of the structural constants occurs for negative energies since

the Schrödinger equation has no eigensolutions for negative energies. Therefore, a reference system is chosen that does not feature eigensolutions in the energy range of an electronic structure calculation. It is characterized by potentials $V^{r,n}(\vec{r},\vec{r}')$ that are located at the scattering centers n. We can then define

$$\Delta t^{n}_{\Lambda\Lambda'}(E) = t^{n}_{\Lambda\Lambda'}(E) - t^{r,n}_{\Lambda\Lambda'}(E) \tag{3.56}$$

which is the difference of the t-matrix of the real system $t^{n}_{\Lambda\Lambda'}$ (see eq. (3.46)) and the t-matrix of the reference system $t^{r,n}_{\Lambda\Lambda'}$ which are defined by $V^{r,n}(\vec{r},\vec{r}')$.
In order to derive a Dyson equation in which free space is substituted, the structural reference Green functions $G^{r,nn'}_{\Lambda\Lambda'}$ must be calculated from

$$G^{r,nn'}_{\Lambda\Lambda'}(E) = g^{nn'}_{\Lambda\Lambda'}(E) + \sum_{n'',\Lambda'',\Lambda'''} g^{nn''}_{\Lambda\Lambda''}(E) t^{r,n''}_{\Lambda''\Lambda'''}(E) G^{r,n''n'}_{\Lambda'''\Lambda'}(E), \tag{3.57}$$

where $g^{nn'}_{\Lambda\Lambda'}$ are the familiar Green functions for free space.

The Dyson equation for the structural Green functions of the real system in reciprocal space is then given by

$$G_{\Lambda\Lambda'}(\vec{k},E) = G^{r}_{\Lambda\Lambda'}(\vec{k},E) + \sum_{\Lambda'',\Lambda'''} G^{r}_{\Lambda\Lambda''}(\vec{k},E)\Delta t_{\Lambda''\Lambda'''}(E) G_{\Lambda'''\Lambda'}(\vec{k},E). \tag{3.58}$$

An inversion leads to the Dyson equation for the screened KKR method

$$G_{\Lambda\Lambda'}(\vec{k},E) = \left[\left(\underline{\underline{1}} - \underline{\underline{G}}^{r}(\vec{k},E) \underline{\underline{\Delta t}}(E) \right)^{-1} \underline{\underline{G}}^{r}(\vec{k},E) \right]_{\Lambda\Lambda'}. \tag{3.59}$$

It is important to stress that, if evaluated exactly, eq. (3.59) and eq. (3.49) yield identical results but that the former features the aforementioned exponential decay in space of $\underline{\underline{G}}^{r}$ which is favorable with regards to the convergence of an iterative solution. The decay can be visualized by considering the 'partial norm'

$$N_{ll'}(|\vec{R}_i - \vec{R}_j|,E) = \frac{|E|^{(l+l')/2}}{(2l+1)!!(2l'+1)!!} \times \left[\sum_{mm'} |G^{r,ij}_{lm,l'm'}(E)|^{2} \right]^{1/2} \tag{3.60}$$

which is plotted in Figure 3.3 both for the screened muffin-tin potential and free space. In case of the screening muffin-tin potential $N_{ll'}(|\vec{R}_i - \vec{R}_j|,E)$ is rapidly decaying with increasing distance between scattering site i and j, while free space as a reference system leads to a very weak decay.

3.6. Self-consistent Solution

After having discussed the necessary steps of the KKR scheme we can formulate a self-consistency cycle (cf. [33]) in which the electronic density is adjusted until convergence is achieved and the variational principle of Hohenberg and Kohn (c.f. eq. (2.3)) is fulfilled. The crucial steps in the self-consistency cycle are the following:

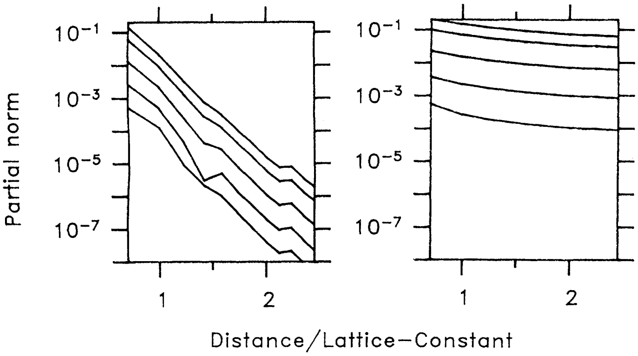

Figure 3.3.: Screened (left panel) and unscreened (right panel) partial norms for $l = l'$ as a function of the distance in units of the lattice constant. The results for $l = 0, 1, 2, 3$ and 4 are shown from top to bottom. Reprinted with permission from [49]. Copyright 1995 by the American Physical Society.

1. Define initial potential V_{in}.
2. Calculate single-site solutions (eqs. (3.26) to (3.29)) for all sites n.
3. Set up screened reference system according to the scheme presented in section 3.5.
4. Solve Dyson equation given in eq. (3.59).
5. Use resulting Green function to extract density n_{out} via the complex energy contour integration in eq. (3.13).
6. Compute new potential V_{out} by means of the Poisson equation which reads $\nabla^2 V_{\mathrm{out}} = -8\pi n_{\mathrm{out}}$.
7. Check convergence by comparing V_{in} and V_{out}. If the potential is not converged, mix V_{out} with V_{in} and use the result as new V_{in} to start again from step 1.

In this chapter the fundamentals of the KKR methodology were outlined. They form the basis of several KKR codes that are developed e.g. in Jülich, Munich, Halle and other places.

In the next chapter, we focus on the unique features of the massively-parallelized KKR`nano`. It is shown that the multiple-scattering part is the computationally most demanding problem and how it can be solved with less computational effort

4

Linear-scaling KKR`nano` and High Performance Computing

The growing interest in phenomena that occur on a length scale of nanometers has triggered research in the direction of linear-scaling DFT methods. The KKR Green function as it is presented in the previous chapter suffers from a bottleneck due to the scaling behavior of its arithmetic complexity which behaves like $O(N^3)$, where N is the number of Voronoi cells that are in the unit cell. This number usually coincides with the number of atoms unless empty cells are included in the system. Obviously, this sets an upper bound for the length scales of the phenomena that can be investigated with ordinary KKR codes. In recent years substantial efforts have been made within the electronic structure community to overcome this computational barrier [56].
Zeller gives a vivid explanation of how DFT can be used for large-scale calculations on state-of-the-art supercomputers with thousands of processors in [32]. It turned out that in order to fully utilize such machines, it is most effective to use grid-based real-space algorithms that can exploit the locality of the real-space Kohn-Sham equations. Thereby, wave functions, electronic density and potentials need to be stored only locally and the inter-processor communication is kept at a minimum. It can be shown that by exploiting the near-sightedness principle of electronic matter [57] the cubic scaling can be reduced to a linear scaling with complexity $O(N)$. Examples of codes that follow this principle are the locally self-consistent multiple scattering (LSMS) code [58], CONQUEST and ONETEP that can handle up to hundreds of thousands of atoms [59].
KKR`nano` [33] is an electronic structure code, specifically designed for petaFLOP computing. Its method falls in the category of codes that scale linearly with the number of atoms, so that we can realize system sizes of up to half a million atoms in a unit cell.

The purpose of this chapter is to introduce the underlying concepts of KKR`nano` and to explain in which sense it was extended during the course of this PhD thesis. At the beginning, we introduce the iterative solver for the multiple-scattering problem and the real-space truncation based on the extensive description by Thieß in [33]. Both are crucial measures in order to achieve linear-scaling. A large part of this chapter is dedicated to High Performance Computing. Here, we present current and upcoming hardware architectures for supercomputers and discuss the various parallelization options that KKR`nano` has to offer. Part of this ongoing work is the efficient usage of GPUs to solve the multiple-scattering problem. A subsection on benchmarks that were run during the JUQUEEN Extreme Scaling Workshop 2017 provides evidence that the multiple-scattering solver in KKR`nano` scales indeed linearly. The benchmarks also show that the solution of the Poisson equation does not scale linearly. For the treatment of a million atoms on the upcoming generation of supercomputers it is therefore required to further optimize the formalism by e.g. using fast multipole methods [60].

Methodological improvements with regards to KKR`nano` that have been made in the context of this thesis are presented in chapter 5.

4.1. Iterative Solution of the Dyson Equation

The solution of the Dyson equation in eq. (3.59) constitutes the biggest computational challenge in large-scale KKR calculations. Its computational complexity can be reduced by choice of a suitable reference system, i.e. a system of repulsive potentials that guarantees the exponential decay of the Green function elements (c.f. section 3.5). Then, the reference Green function is given as a sparse matrix with $(l_{\text{max}}+1)^4 N_{\text{cl}} N$ instead of $(l_{\text{max}}+1)^4 N^2$ non-zero elements, where N_{cl} denotes the number of atoms in the reference cluster and N the number of atoms in the complete system. While a direct inversion with a linear algebra package, e.g. LAPACK, is the appropriate line of action if confronted with a dense matrix, it can be advantageous to consider an iterative approach, if the matrix is sparse. This is a crucial intermediate step towards a linear-scaling algorithm since it lowers the number of necessary algebraic operations from $O(N^3)$ to $O(N_{\text{it}} N_{\text{cl}} N^2)$, where N_{it} is the number of iterations needed to invert the matrix iteratively.

In the following it is explained how the Dyson equation is rewritten in order to solve it with an iterative scheme which is presented subsequently (cf. [19, 33]).
Omitting the indices for a moment, the Dyson equation reads

$$G = G^r + G^r \Delta t G, \tag{4.1}$$

where G is the sought Green function, G_r is the Green function of the screened reference system and $\Delta t = t - t_{\text{ref}}$ is the difference between the t-matrices of the actual system and the reference system.
We can rewrite eq. (4.1) as

$$(1 - G^r \Delta t)G = G^r = -(1 - G^r \Delta t)(\Delta t)^{-1} + (\Delta t)^{-1} \tag{4.2}$$

and multiply by $(1 - G^r \Delta t)^{-1}$ so that

$$G = -(\Delta t)^{-1} + (\Delta t)^{-1} \underbrace{\left[(\Delta t)^{-1} - G^r\right]^{-1}}_{M^{-1}} (\Delta t)^{-1}. \tag{4.3}$$

If it was not for M^{-1}, this equation could be evaluated easily but the calculation of M^{-1} requires a computationally expensive matrix inversion. In a direct matrix inversion M is decomposed into a product of lower and upper triangular matrices which comes with computational costs of $O(N^3)$ floating-point operations for dense matrices. Such a cubic scaling behavior obviously prohibits the investigation of very large supercells and a computationally less demanding way to compute M^{-1} is desirable. It is difficult to parallelize a matrix inversion routine as this inevitably involves operations that can only be performed sequentially.

An iterative inversion provides a way that exploits the sparsity of M and thereby avoids the cubic scaling. If we define $X = M^{-1}$,

$$\Delta t M X = \Delta t \tag{4.4}$$

holds and by inserting M we get

$$X - \Delta t G^r X = \Delta t. \tag{4.5}$$

This equation can be reformulated as an iterative condition

$$X^{(i+1)} = \Delta t + \Delta t G^r X^{(i)}, \tag{4.6}$$

where $X^{(i)}$ is inserted in iteration i to obtain the input $X^{(i+1)}$ for the next iteration step $i+1$. In principle, an iterative mixing scheme that ensures proper convergence can be used to determine the result, e.g. Anderson mixing [61]. However, such mixing schemes require memory-demanding bookkeeping of prior steps in the iteration process which contradicts our intention to keep memory consumption low in KKR`nano`.

Therefore, eq. (4.5) is reformulated as

$$(\Delta t G^r - 1) X = -\Delta t \tag{4.7}$$

to take the form of a system of linear equations

$$Ax = b. \tag{4.8}$$

In our case A, x and b are complex matrices and A is non-singular and non-Hermitian. There exist various iterative algorithms to solve linear equation problems, the most popular being the Krylov projection methods. A thorough derivation and detailed description of them is given in [62] whereas this thesis only covers the fundamentals. In a nutshell, the Krylov subspace methods approximate $x = A^{-1}b$ by $p(A)b$, where $p(A)$ is a polynomial that contains powers of A.

The basis of the algorithm is the creation of a Krylov subspace

$$K_n(r_0, A) = \text{span}\{r_0, Ar_0 \ldots, A^{n-1}r_0\} \tag{4.9}$$

by consecutively multiplying A with the residual vector $r_0 = b - Ax_0$, where x_0 is an initial guess for the solution x. An approximation to the solution of eq. (4.8) in the subspace K_n is then given by

$$A^{-1}b \approx x_m = x_0 + q_{m-1}(A) r_0, \tag{4.10}$$

in which q_{m-1} is a polynomial of degree $m-1$, i.e. it contains powers of A up to A^{m-1}. The way it is constructed depends on the chosen Krylov method. Well-known methods are the Lanczos algorithm, the GMRES algorithm and the QMR algorithm whose transpose-free variant (TFQMR) is utilized in KKR`nano`. For algorithmic details the reader is referred to the literature [33, 63]. The TFQMR algorithm was specially tailored to yield good convergence for the non-singular and non-Hermitian problem that eq. (4.7) constitutes. In the standard QMR algorithm a matrix-vector product with both A and the transpose A^T is required. TFQMR avoids multiplications with the transpose A^T which would require intensive communications between the individual processors as more array entries would have to be shared. An extensive explanation of the TFQMR algorithm itself and the implementation in KKR`nano` is given by Thiess [33]. The default choice for the initial guess x_0 is $0+0i$ but a smarter choice in combination with a preconditioning scheme (see below) can significantly reduce the number of necessary iterations in the algorithm.

Complementary to a well-considered initial guess convergence can be further improved by preconditioning the problem at hand (cf. [33]). The underlying concept is to find a matrix

$$P = P_1 \cdot P_2 \tag{4.11}$$

that approximately corresponds to A and for which the inverse P^{-1} can be easily determined. This leads to a modified linear matrix equation

$$A'y = b', \tag{4.12}$$

where $A' = P_1^{-1}AP_2^{-1}$, $b' = P_1^{-1}(b - Ax_0)$ and $y = P_2(x - x_0)$. x_0 is again the initial guess of the solution to the initial problem $Ax = b$. The residual vector for eq. (4.12) is given by $r'_n = b' - A'y_n$. When r'_n is sufficiently small, i.e. convergence is reached, the solution to the genuine problem is connected to y_n by

$$x_n = x_0 + P_2^{-1}y_n \tag{4.13}$$

with a residual vector that reads

$$r_n = P_1 r'_n. \tag{4.14}$$

The effect of preconditioning schemes has been studied in KKR`nano` yielding mixed results [64]. On the one hand schemes like the block-circulant preconditioning (BCP) can accelerate convergence substantially, on the other hand preconditioning does not guarantee better convergence per se but is very sensitive with regards to the treated material and its crystal structure, e.g. calculations concerning amorphous systems do not benefit from BCP. In light of this observation the decision was made to drop the support of BCP in KKR`nano`.

4.2. Truncation for Linear Scaling

The introduction of the screened reference potential (see section 3.5) in combination with the iterative solution of the Dyson equation led to an $O(N_{\text{it}}N_{\text{cl}}N^2)$ scaling behavior. This $\propto O(N^2)$ scaling can be further improved to become a linear $\propto O(N)$ scaling by using Kohn's nearsightedness principle [57]. In KKR`nano` this translates into the spatial truncation of the Green function [19].
Prototypes of such a neglect of long-range effects are the locally self-consistent multiple scattering (LSMS) [58] and locally self-consistent Green function (LSGF) methods which are based on the assumption that the local electronic density is not decisively affected by the potential of sites that are sufficiently faraway. However, both LSMS and LSGF are limited in the sense that the computational effort increases cubically with the number of atoms in the truncation zone and hence the truncation needs to be made at a rather short range to prevent this behavior from becoming a dominant factor in the overall scaling. This necessity also diminishes the effectiveness of an iterative solving scheme as this is only efficient, if matrices are of a certain sparsity. In LSMS an iterative solver has been tested [65] but it was found that due to the rather small number of atoms within the truncation cluster, typically about a hundred atoms, a direct inversion is preferable.
The procedure introduced by Zeller [66] and implemented in KKR`nano` [19] combines the TB-KKR formalism (c.f. section 3.5) with a truncation of the Green function and an iterative solution of the Dyson equation (c.f. section 4.1).

It is instructive to recall the connection of the single-particle density matrix with the Green function

$$\rho(\vec{r},\vec{r}') = -\frac{1}{\pi}\text{Im}\int_{-\infty}^{\infty} dE f(E,E_F,T)G(\vec{r},\vec{r}',E), \tag{4.15}$$

where an evaluation shows that the spatial decay of $\rho(\vec{r},\vec{r}')$ is mainly determined by the decay of the Green function at the first Matsubara energy $E = E_F + i\pi k_B T$. This relation between density matrix and Green function suggests that a truncation of the Green function above a distance $|\vec{r}-\vec{r}'|$ is equivalent to a neglect of the density matrix elements above the same distance.
The Dyson equation formulated as a system of linear equations (c.f. eq. (4.7)) with an imposed truncation reads

$$\sum_{\mu}\sum_{L'} A^{\nu\mu}_{LL'} X^{\mu}_{L'L''} = b^{\nu}_{L'L''}. \tag{4.16}$$

The truncation is determined by the parameter ν which runs only over the atoms inside the truncation cluster. The index μ is the index for the screened reference Green function. This alters the scaling from $O(N_{\text{it}}N_{\text{cl}}N^2)$ to a linear scaling $O(N_{\text{it}}N_{\text{cl}}N_{\text{tr}}N)$ in N, where N_{tr} is the number of atoms in the truncation cluster. In an ideal scenario the introduction of a truncation can therefore lead to a reduction of complexity by the factor N_{tr}/N which can be quite significant, e.g. in a system with $N = 10000$ atoms and a truncation cluster that contains only $N_{\mathrm{tr}} = 1000$ atoms.

Truncating interactions naturally introduces a methodological inaccuracy. This is however well controlled and test calculations for metallic NiPd have shown that the total energy per atom changes by less than 2 meV with a truncation cluster that comprises $N_{\mathrm{tr}} = 959$ atoms [19].

The size of the truncation cluster can be defined differently for the separate angular momentum scattering channels, e.g. contributions from components with $l = 1$ can be truncated at a larger distance than components with $l = 0$. Such an l-dependent truncation was implemented in KKR`nano` but it did not yield the expected performance enhancement and was therefore dropped as it does not comply with our policy of performance-oriented implementations.

4.3. Parallelization for High Performance Computing

KKR`nano` was designed to utilize the most powerful supercomputers available and an ongoing effort is made to ensure that the code runs efficiently on such machines. This comprises the porting of KKR`nano` to new architectures, performance optimization and sometimes also the rewriting of routines that are crucial to the overall performance.

The Forschungszentrum Jülich provides and excellent supercomputing architecture and its machines JUQUEEN and JURECA are featured in the latest TOP500 list from November 2017 (see [67]).

The TOP500 list is composed of the 500 supercomputers around the world that achieve the best performance in the LINPACK benchmark which gives a measure of a system's floating point computing power. Figure 4.1 gives an account of the performance development of the supercomputers represented in the TOP500 list. It shows how High Performance Computing (HPC) has evolved from the gigaflop regime and is currently approaching the threshold to the exaflop regime.

Exascale computing will bring along a variety of new challenges, e.g. keeping energy consumption at a reasonable level or the necessity to minimize the impact of unavoidable failures of hardware parts over time which occur more often, if a machine relies on more components [20].

Today's HPC machines are constructed of thousands of processing units and exploiting their full potential poses a great challenge to scientists. In order to use them efficiently, the computational problem at hand needs to be split up into smaller pieces and distributed to the single units. The results of these individual calculations must then be brought back together to solve the initial task. Hence, an adequate parallelization scheme as it is presented for KKR`nano` in section 4.3.2 is crucial. In the future the required level of parallelism in HPC will increase even more because Dennard scaling, i.e. transistors get smaller while their power density stays constant, will come to an

end.
To minimize power consumption, low-clocked, but highly parallel compute devices like GPUs (Graphics Processing Unit) have become more important in HPC and will continue to play an even bigger role. Therefore, the TFQMR solver in KKR`nano` was ported to Nvidia GPUs by Thorsten Hater from the Jülich Supercomputing Center [68]. Subsequent tests that were performed in the context of this thesis revealed anomalies that can arise, if code is ported to a different architecture (see section 4.3.3).

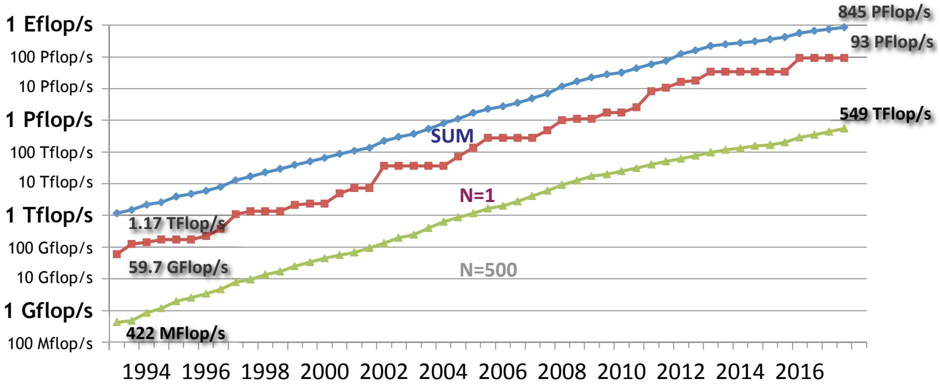

Figure 4.1.: Performance development of the supercomputers represented in the TOP500 list over the past two decades. The three data sets denote the cumulative LINPACK-measured peak performance of the fastest 500 supercomputers in the world (SUM), the peak performance of the single fastest supercomputer in each year (N=1) and that of the supercomputer taking 500th place in the list (N=500). Reprinted with permission from [67].

4.3.1. Hardware Architectures

Since HPC systems have become increasingly heterogeneous, e.g. hybrid architectures entered the market which consist of a *host* compute unit and an *accelerator* module, performance tuning and the design of customized algorithms is of outmost importance in order to use these systems efficiently. In the following the most common hardware architectures currently used in HPC are presented and a brief description of their strengths and weaknesses is given.

Intel Xeon Haswell

The Intel Xeon x86 microprocessor is widely used in servers and embedded systems. They are very similar to the CPUs that can be found in ordinary workstations but are equipped with some more advanced features, e.g. larger cache memory. The product line was introduced in 1998.

Both JURECA in Jülich and the fastest German supercomputer HazelHen in Stuttgart are equipped with Xeon E5-2680 v3 Haswell 2.5 GHz CPUs which feature 12 cores per die and 128 GiB of memory per compute node. The nodes of both machines consist of two such CPUs so that the total number of cores per node is 24. Communication between different nodes is facilitated by high-speed interconnection networks that are provided by Mellanox and Cray, respectively.

A very important feature of state-of-the microprocessors is SIMD (Single instruction, multiple data), i.e. the possibility to 'vectorize' floating-point operations. This means that the operations are performed on multiple values stored in vectors at once in parallel instead of serially on single scalar values. The Haswell microarchitecture provides the Advanced Vector Extensions (AVX) 2.0 with 256-bit instructions for that purpose. Such vectorization is performed automatically by the compiler but supplemental hints on where and how to vectorize can help improve the procedure.

The Intel Haswell architecture aims at general purpose computing with powerful individual CPU cores and therefore massive parallelism is not an issue as crucial as it is with other architectures. However, such convenience brings along the negative aspect of a relatively high power consumption per floating point operation which makes this design ineligible for future exascale computing.

Nvidia GPU Accelerators

Starting from the early 2000s, Graphics Processing Units (GPUs) have been introduced to HPC as so-called *accelerators* that are characterized by their ability to deal with massive parallelism which is not only needed for video games but can also be exploited for supercomputing [69]. Within a decade GPUs evolved from single core devices with fixed function hardware to highly parallel and programmable devices suited for general purpose computation.

The GPUs that can be found in current HPC machines are predominantly manufactured by Nvidia. A rather small amount of 75 nodes of JURECA is equipped with Nvidia K80 GPUs that can be used additionally to the CPUs. Other supercomputers, e.g. TITAN at Oak Ridge National Laboratory and its upcoming successor SUMMIT, are already based solely on the computational power of GPUs and the trend towards such GPU-based accelerator architectures is expected to intensify. A very important feature is the support of double precision floating-point operations described in the IEEE 754 standard [70]. It is indispensable in scientific computing and is available in all of Nvidia's current HPC-GPUs. Another crucial aspect is the bandwith between CPU and GPU memory which is very often a performance-limiting bottleneck. A new memory interconnect called NVlink that provides more bandwith has recently been introduced by Nvidia and IBM [71]. A detailed description of the GPU architecture goes beyond the scope of this thesis and the reader is referred to, e.g. [72], for further technical details. Nvidia's Kepler generation GPU GK110, that was used for our benchmarks in [68], has a clock speed of 745 MHz which is significantly less than the 2.5 GHz of the CPUs used in JURECA. Lower clock speeds help improving the power efficiency since less heat is dissipated. In terms of performance this is compensated by the very high floating-point operation throughput made possible by the high degree of parallelism. A single GK110 can efficiently handle 30720 threads at once. This makes GPUs perfect tools for large linear algebra problems. There exist linear algebra libraries specifically designed for GPUs for this purpose, e.g. cuSPARSE [73].

The generation of GPU-compliant code often requires a change of programming language, e.g. from Fortran90 to CUDA, and a change of compilers. This makes the porting of complex applications from a classical architecture such as x86 microprocessors to GPUs rather complicated. It is therefore advisable to first port the parts of an application that are most crucial to its overall performance as it was done for the TFQMR solver in KKR`nano` (see section 4.3.3).

Intel Xeon Phi

The Xeon Phi series of processors is intended as an x86-compatible answer by Intel to the challenge posed by GPUs in HPC. It is an attempt to adopt the advantage of low energy consumption per floating point operation that a GPU has over standard CPUs, while keeping the required optimization and performance tuning, when porting the applications, as small as possible. This is achieved by keeping the clock rate low and by using a high degree of parallelism. Application developers can stick to their programming language and applications that run on x86 microarchitectures will run on a Xeon Phi, too.

The latest revision of this series of processors was named Knights Landing (KNL). Its low clock rate is compensated by a high number of cores (between 64 and 72), high bandwith memory located very close to the cores and very wide SIMD units. The high bandwith memory (MCDRAM) is shared between all the cores and can either serve as an extended L3 cache or as an extension to the DDR-RAM. KNLs are equipped with the new AVX-512 SIMD extension that features a register size of 512 bits instead of the 256 bits supported by AVX 2.0.

The QPACE3 machine installed in Jülich is based on KNLs with 64 cores each running at a clock speed of 1.30 GHz. In June 2017 it took 17th rank in the Green500 list which ranks supercomputers according to their power efficiency. JURECA was recently equipped with 1640 additional KNL nodes that amount to a peak performance of 5 Petaflop.

IBM BlueGene

Not very long ago, IBM BlueGene supercomputers were among the most powerful and most power efficient machines. The key concept behind the latest BlueGene/Q architecture is a reduction of power consumption by using IBM A2 processors with a clock rate of 1.6 GHz and 17 cores per die. The A2 processor was designed as a system-on-a-chip device, i.e. all components except for the memory are embedded on one chip. A single compute node is comprised of one A2 processor but only 16 out of the 17 cores can be used for computation while the 17th core is reserved for the operating system. The processor supports 4-way hardware threading. Each node disposes of only 16 GiB RAM which is little compared to, e.g. JURECA and HazelHen. Therefore, the optimization of an application's memory usage can be of importance. BlueGene/Q has a very large number of nodes and cores and in order to ensure sufficient communication capabilities between them, it is equipped with a five-dimensional torus interconnect. 1024 nodes form a rack and the supercomputer JUQUEEN in Jülich consists of 28 of such racks. It is to be de-installed in 2018.

With regards to upcoming machines the focus of IBM's HPC efforts seems to have shifted towards the OpenPower architecture, where an IBM POWER processor is combined with an accelerator, e.g. an Nvidia Volta chip.

4.3.2. Parallelization Schemes in `KKRnano`

The parallel supercomputing architectures that are described above are more complex than commodity workstations, as they are used in offices or at home, and exploiting their full potential requires the deliberate use of parallelization schemes. This topic is covered extensively in the literature, e.g. part D in [32], and we explain here only the most important concepts.

Let us assume for a moment that we have a serial application that runs nicely on our single processor. We further assume that 9/10 of it can be parallelized, i.e. these parts of the code can be run in parallel on multiple processors. This leaves us with a serial part of $\alpha = 0.1$ that cannot be run in parallel, e.g. because a calculation done in the code requires input from a prior calculation. According to Amdahl's law [74] the maximum speedup that can be achieved by parallelization is given by

$$S_r = \frac{1}{\alpha + \frac{1-\alpha}{n}}, \tag{4.17}$$

where n is the number of available processors. An example of modest parallelization is $n = 8$ which leads to a speedup of $S_r = 4.7$, a value that is surprisingly small given that the resources are increased eightfold. It is furthermore instructive to consider the limit $n \to \infty$ for which

$$S_r \to \frac{1}{\alpha} \tag{4.18}$$

meaning that in our example there is an upper limit of speedup of $S_r = 10$ that cannot be overcome, even if there was an infinite number of processors at our disposal. This gives a good impression of the limitations of parallelization. Nevertheless, it will be shown in the following that the KKR method can be sufficiently parallelized and that it is parallelization that allows us to treat systems containing ten thousands of atoms.

The two most common programming models for parallel computing are the Message Passing Interface (MPI) [75] and the Open Multi-Processing (OpenMP) [76].

MPI allows to initiate an appropriate number of *tasks* where each of the tasks has its own non-shared memory. Tasks can be seen as sub-processes that run independently of each another unless they are explicitly told to do otherwise at certain points in the code. Often, the number of tasks is chosen such that it coincides with the number of available processor cores. Tasks can communicate with each other, i.e. data can be exchanged, consolidated or barriers can be put in place that suspend the execution of the code until all tasks have reached a specific point defined in the code.
With MPI it is possible to create a hierarchical structure of tasks. In this way we can group tasks according to the purpose they serve. Let us assume that there is a computational problem that we want to solve in parallel for N different input configurations and sum up the results at the very end. Then, we would assign N MPI tasks to this and run the calculation. However, it could be that each of these individual calculations can also be parallelized internally, e.g. assume that we want to compute the sum of the integrals of N different functions numerically and want to use M integration points in each integration. A highly parallelized code could then initiate N tasks (one for each function) and additionally M *sub-tasks* for each integration point so that in total $N \cdot M$ MPI tasks are launched. In the following we will refer to such different types of MPI tasks as *levels*.

The OpenMP programming model is based on a different approach, where the parallel processes are called *threads*. OpenMP allows to define parallel regions in the code at which the *master thread* forks into several threads that then run in parallel until the end of the parallel region is reached, where these threads are killed and the master thread continues to execute the code sequentially. Unlike MPI tasks, OpenMP threads share a common memory address space.
Typically, OpenMP is used when single loops in a code shall be parallelized with little effort. All iterations of the loop can be carried out in parallel, if the operations that are performed for each increment do not depend on each other.

KKR`nano` features both MPI and OpenMP parallelization [19]. The parallelization concept is sketched in Figure 4.2. There are three MPI levels to parallelize over atoms, spins and energy points. OpenMP is used in various parts of the code, mainly to parallelize important loops. The single-site solver for calculations involving non-collinear magnetism and the TFQMR solver that solves the Dyson equation are the parts that potentially benefit the most from OpenMP.

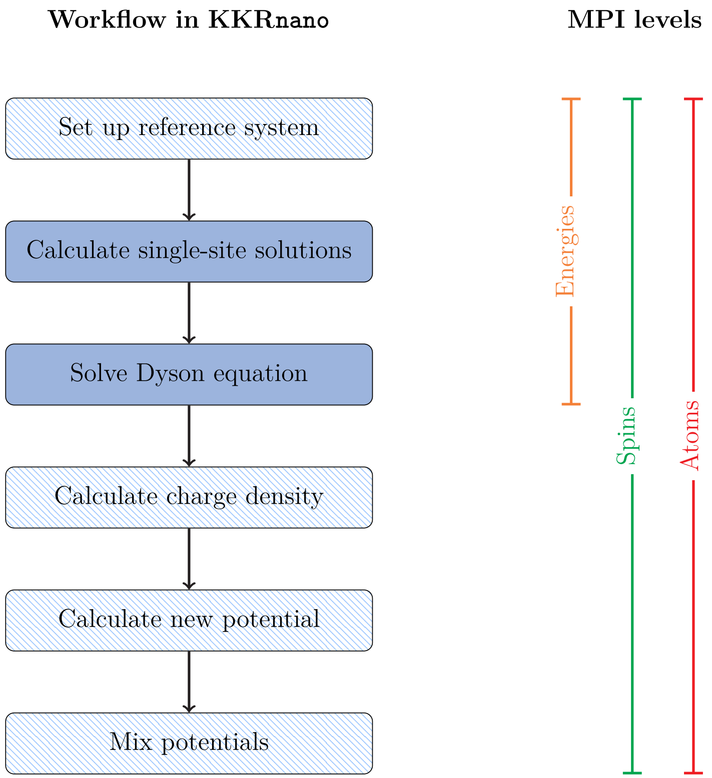

Figure 4.2.: Schematic representation of MPI and OpenMP parallelization in KKR`nano`. The most important steps in the KKR workflow are depicted on the left side and the three MPI regions over atoms, spins and energy points are indicated on the right side.
Parts filled with blue comprise routines where OpenMP is used and where this can be of high importance to the overall performance while in the striped blue parts OpenMP is used but is less significant.

MPI parallelization over atoms

The most crucial MPI level in KKR`nano` is the one for atoms since application scenarios for KKR`nano` involve the treatment of a few thousand atoms and the KKR formalism allows us to solve the multiple-scattering problem locally for each atom, if the Green functions of the reference system and the t-matrices of the other scattering centers are provided (see eq. (4.7)). In practice one MPI task handles 1-16 atoms.
The reference Green functions are calculated by each task for the atoms it is responsible for and are then sent to other tasks that require them. The reference t-matrices for the atoms inside the respective reference cluster are not communicated but calculated by

each task individually as it takes less time to re-compute them than communicating them. In any case the t-matrices of the actual systems need to be communicated. After the necessary information is distributed, the Dyson equation can be solved independently by each task. The calculation of the local charge density can also be conducted locally since only the diagonal nn-elements are needed for this. In order to subsequently obtain the potential from the local charge moments via the Poisson equation, the moments must be shared with all other atom tasks by means of all-to-all communication.

MPI parallelization over spin channels

If the system of interest is a collinear magnet, the two spin channels can be handled by two distinct MPI tasks since the magnetic Kohn-Sham equations are separable (c.f. eq. (2.8)). Due to the relatively small additional MPI communication effort this yields an almost ideal speed-up by a factor of 2. It should be noted that in the non-collinear KKR formalism such a separation of spin channels is no longer possible because there is intermixing (c.f. eq. (5.5)) and all operations involving the t-matrices and Green functions in the global frame of reference need to be performed in full spin space, i.e. $\{\uparrow\uparrow, \uparrow\downarrow, \downarrow\uparrow, \downarrow\downarrow\}$. Thus, the spin parallelization level can only be used in connection with a collinear calculation.

MPI parallelization over energy points

The requirement to calculate the Green function at different energy points offers another possibility to introduce a parallel level since the values of the Green function $G(\vec{r}, \vec{r}, E_i)$ at energy points E_i can be obtained in parallel. After the values are obtained the results must be distributed among the processes within the energy parallelization level to recover the full Green function at all energy points.

Assigning one MPI task to each energy point is not a promising concept because of the significantly different runtimes per energy point. Especially the points closest to the Fermi level (and therefore to the real axis) need many more k-points and TFQMR iterations than the points that lay high up in the complex plane (see fig. 3.1). Therefore the energy points are split into three different groups and each group is taken care of by one MPI task. In the first iteration of the self-consistency cycle the points are equally distributed to all groups. At the end of the first iteration the points are regrouped depending on how much time was used at each point. The aim is to find a grouping for which all groups of energy points are converged at a similar time so that idle tasks are avoided. This is also referred to as *dynamical load-balancing*. A correct load-balancing is of outmost importance to the effectiveness of this MPI level since all tasks need to have finished before the program can move on to the solution of the electrostatic problem, i.e. the Poisson equation. Due to the challenge that load-balancing can pose, parallelization over energy points should only be used, if plenty of processor cores are

available and ought to be utilized.
A lookahead on the performance results presented in section 4.3.4 reveals that with growing system size the electrostatic problem, which in terms of energy parallelization must be considered a serial part of the code, becomes computationally more relevant. Table 4.1 shows that the fraction of the electrostatics (ES) solver runtime compared to the combined runtime of TFQMR solver and ES solver ranges from $\alpha = \frac{84}{432+84} = 0.16$ for 8,192 atoms to $\alpha = \frac{470}{430+470} = 0.52$ for 229,736 atoms. According to eq. (4.18) this limits the maximum speedup that can be achieved by energy parallelization to $S_r \to 6.25$ and $S_r \to 1.92$, respectively.

OpenMP parallelization

KKR`nano` can be compiled either with or without support for OpenMP. If it is enabled, loops primarily in the TFQMR solver but also in the routines that calculate the regular and irregular solutions are executed using parallel threads. This is particularly useful on architectures that support simultaneous multithreading (SMT). However, we try to use BLAS (Basic Linear Algebra Subprograms) library routines for arithmetic operations, e.g. matrix-matrix multiplications, throughout our code. BLAS libraries usually have their own built-in SMT support. Therefore, the available SMT threads must be partitioned between the explicit OpenMP parallel regions in the code and the implicit parallelization of the BLAS library. Here, the optimal partitioning is highly architecture-dependent and a general recommendation cannot be given.

Multiple Atoms per Thread

Assigning multiple atoms to one MPI task is beneficial, if the hardware architecture is not based on a large number of CPU cores, e.g. BlueGene/Q, but heterogeneous as in the accelerated architectures. The host device can be, e.g. an IBM Power 9 CPU, and the accelerator an Nvidia Volta GPU.
The goal that is pursued in GPUs is to process a huge amount of floating-point operations per clock cycle, i.e. the amount of data that is processed at once is larger than in CPUs. It is therefore desirable to have the option of treating multiple atoms per MPI process/CPU and thereby increase the problem size per host CPU on such architectures. On the one hand, this helps to reduce the number of individual data transfer events from CPU to GPU (and vice versa). On the other hand, it allows to use the GPU's capacities more efficiently as its capability to handle more data per clock cycle is better utilized.
KKR`nano` can treat multiple atoms per atomic MPI task by using the following algebraic scheme, which was implemented by Elias Rabel: We rewrite the Dyson equation from eq. (4.16) which reads

$$\sum_{\mu} \sum_{L'} A^{\nu\mu}_{LL'} X^{\mu}_{L'L''} = b^{\nu}_{L'L''}, \tag{4.19}$$

where A has dimension $N_{\mathrm{cl}}(l_{\max}+1)^2 \times N_{\mathrm{tr}}(l_{\max}+1)^2$, b usually has the negative local Δt as diagonal elements and X has dimension $N_{\mathrm{tr}}(l_{\max}+1)^2 \times (l_{\max}+1)^2$. A is a matrix of blocks of size $(l_{\max}+1)^2 \times (l_{\max}+1)^2$ while X and b are vectors of such blocks. For more than a single atom per task x and b can also take a matrix form with dimension $N_{\mathrm{tr}}(l_{\max}+1)^2 \times N_{\mathrm{loc}}(l_{\max}+1)^2$, where N_{loc} is the number of atoms treated by one MPI task of the atom parallelization level. The corresponding linear equation system reads

$$\sum_{\mu}\sum_{L'} A^{\nu\mu}_{LL'} X^{\mu\gamma}_{L'L''} = b^{\nu\gamma}_{L'L''}, \tag{4.20}$$

where an additional index γ is introduced that runs over N_{loc}.

The single-site scattering calculations are realized with loops over the local atoms N_{loc} which are OpenMP-parallelized.

4.3.3. TFQMR Solver on GPUs

Exascale supercomputers will rely on devices which operate at relatively low clock frequency but are capable of performing an extraordinary large number of floating-point operations per cycle. Currently, there are two prototypes installed at the Jülich Supercomputing Center to gather experience on this new kind of architecture. They were named JURON and JULIA. JURON is equipped with IBM Power8 host processors and Nvidia P100 GPUs (Graphics Processing Units) of the Pascal generation while JULIA is based on Intel's Xeon Phi KNL architecture.

In this subsection we focus on the GPU-based architecture for which Thorsten Hater ported the TFQMR solver (see section 4.1) from FORTRAN90 to C++ in order to use Nvidia's CUDA language [77] which enables developers to offload computational work directly to the GPU. The author of this thesis integrated the stand-alone version of Hater's TFQMR solver in KKR`nano`. The TFQMR solver accounts for the computationally most demanding part of KKR`nano` and it is therefore appropriate to focus on it.
Benchmarks [68] show that with the ported solver the GPU architecture can be used most efficiently, if large matrices are involved, i.e. the interactions of $N_{\mathrm{tr}} \geq 1000$ atoms are included in the scattering path operator (see left part of Figure 4.3). The maximum performance that can be reached on an Nvidia K40m processor is around 320 GFlop/s. The theoretical peak performance is 1430 GFlop/s.
The performance can be further improved by running multiple tasks on the CPU that use a single K40m simultaneously. Here, the so-called *Multi-process service* (MPS) feature is used. The parallel efficiency can be defined as

$$\epsilon_{\mathrm{par}} = n\Delta t_s/\Delta t_p(n), \tag{4.21}$$

where n is the number of tasks, Δt_s the serial execution time without MPS and Δt_p the time that is required for n concurrent calls of the solver.

A gain of 17% in parallel efficiency, when four or more tasks are used is observed (see right part of Figure 4.3).

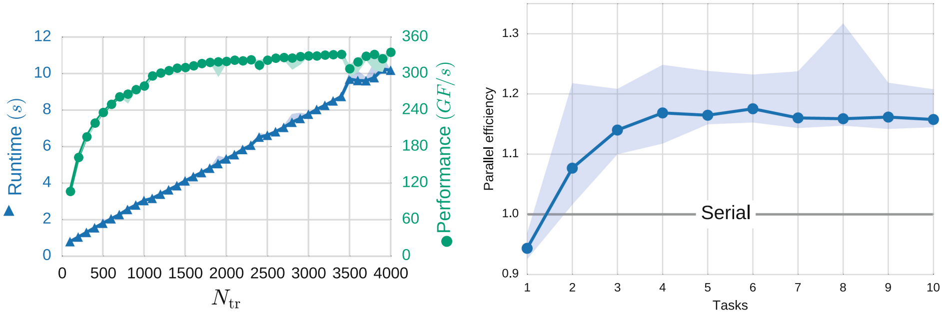

Figure 4.3.: Benchmark performance results obtained for $N_{\mathrm{iter}} = 1000$ iterations using a single (left) and multiple tasks for $N_{\mathrm{tr}} = 1000$ (right) on a single K40m. Reprinted from [68].

The attempt of the author of this thesis to calculate fcc-Cu with four atoms in the unit cell revealed a GPU-specific problem.

The results obtained with the GPU version of the TFQMR solver differ substantially from those obtained with the standard CPU solver. In addition, the symmetry requirement, i.e. all four atoms have to be symmetrically equivalent, is not fulfilled.

A step-by-step comparison of calculations with both solvers shows that at some points in the TFQMR algorithm, array entries in the GPU-based solver are flushed to zero while they remain finite in the CPU version. This happens occasionally when a product of the form $\vec{a} \cdot \vec{b}$ is calculated, where $\vec{a}$ and $\vec{b}$ are complex vectors.

To understand this architecture-related problem an excursion into the basics of floating-point arithmetic is instructive. A comprehensive review on this topic can e.g. be found in [78]. For the sake of simplicity, we consider $\vec{a}$ and $\vec{b}$ to be real in the following.

Let us consider as an example the number 200.15. As floating-point number it can be written in decimal notation as 2.0015×10^2. The $p = 5$ leading digits are called the significand, the decimal base is $\beta = 10$ and the exponent is $e = 2$.

In a processor's floating point unit (FPU) there is only a limited number of bits that are reserved for the representation of a floating-point number with the binary base $\beta = 2$. In KKR`nano` we use double precision for all quantities in the TFQMR solver, i.e. 64 bits in total with 1 bit for the sign, 11 bits for the exponent and 52 bits for the significand according to the IEEE754 standard [70].

However, while Nvidia GPUs strictly follow IEEE754 requirements with 64-bit representation, x86 microprocessors, as they are e.g. manufactured by Intel, use an extended precision of 80 bits with 15 exponent and 64 significand bits during floating point operations [79]. The result is stored with only double precision in both cases. Both the bit-wise layouts of the IEEE754 double precision standard and of the x86 extended precision are visualized in Figure 4.4.

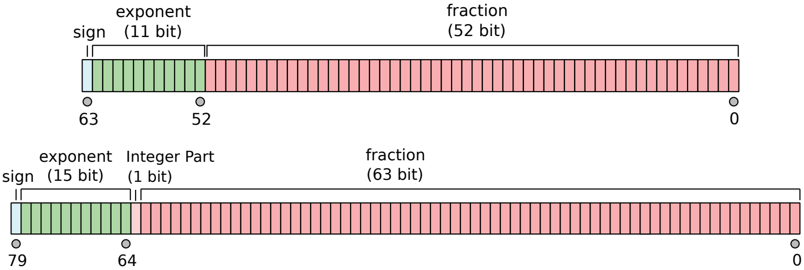

Figure 4.4.: Top: The layout of a double precision floating point number (64 bits) including the sign bit, the exponential bits and the significand/fraction bits. The figure was created by Codekaizen and licensed under CC BY-SA 4.0. Bottom: The analogue for an extended precision floating point number (80 bits) on x86 processors. Here, the significand bits also include a single integer bit since there is no *hidden bit*. The figure was created by BillF4 and licensed under CC BY-SA 3.0.

The different precision can lead to a difference in the computed result and potentially cause a breakdown in the TFQMR algorithm. For the detailed algorithm we refer the reader to p. 36 in [33].

Remember that we attempt to iteratively solve a linear equation problem of the form $Ax = b$, where A, x and b are complex matrices. Here, complex vectors derived from entries in the matrix A are multiplied repeatedly with each other. For fcc-Cu the absolute values of the complex numbers in A range from an order of $O(10^{-20})$ to an order of $O(1)$ (see Figure 4.5).

Such a spread of values poses a challenge for floating-point arithmetic. This can be exemplified by considering the dot product

$$\vec{a} \cdot \vec{b} = \begin{pmatrix} 1.0 \\ 1.0 \times 10^{-9} \\ 1.0 \end{pmatrix} \cdot \begin{pmatrix} -1.0 \\ 1.0 \times 10^{-9} \\ 1.0 \end{pmatrix} = -1.0 + 1.0 \times 10^{-18} + 1.0, \tag{4.22}$$

where the exact sum is clearly 1.0×10^{-18}.

Here, we encounter a problem of floating-point accuracy , when numbers have exponents that are far apart. In order to add 1.0 and 1.0×10^{-18} the latter summand is brought to the same exponent as the first, i.e. $e = 0$. This requires bit shifting by 18 positions, if the basis $\beta = 10$ is used. Computing architectures naturally use $\beta = 2$, which would make it necessary to shift the bits by 60 positions to approximate 1.0×10^{-18} by a finite value. IEEE754 double precision provides a significand of only 53 bits (52 plus one *hidden bit*) so that 1.0×10^{-18} is flushed to 0.0×10^{0} in the summation in eq. (4.22) which results in $\vec{a} \cdot \vec{b} = 0$.

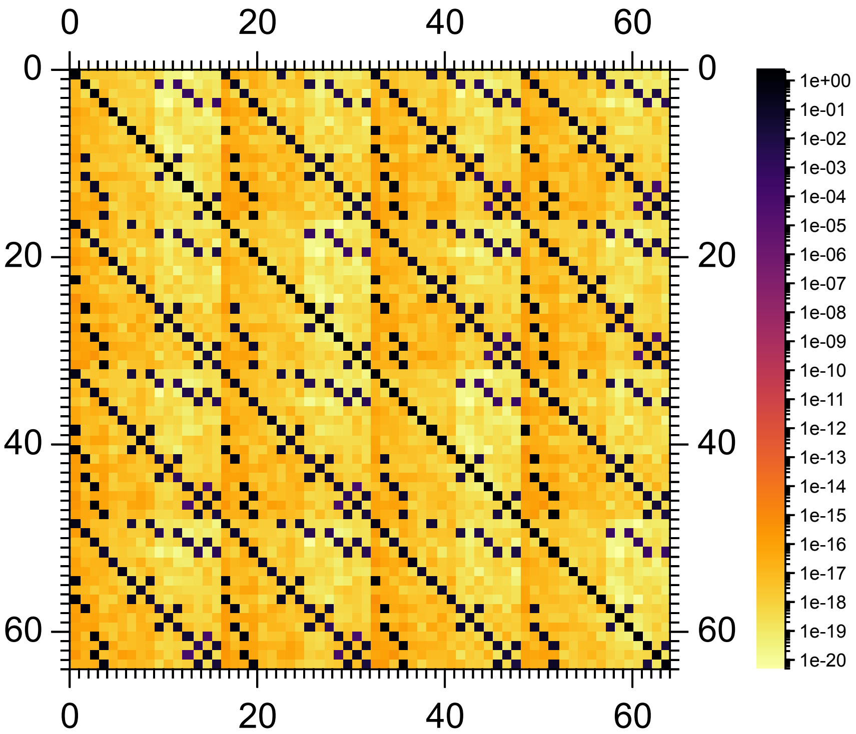

Figure 4.5.: Structure of the complex matrix A in the TFQMR eigenwert problem given by eq. (4.8) for fcc-Cu with four atoms in the unit cell. The matrix is composed of 4x4 blocks, where each block is of the size $(l_{\max}+1)^2 \times (l_{\max}+1)^2$. In our calculation we use $l_{\max} = 3$. The color bar indicates the absolute value of each complex number in the matrix. Figure created by Ingo Heimbach.

Contrarily, FPUs as in the Intel Haswell architecture use an extended precision of 64 significand bits that can represent 1.0×10^{-18} as a finite value in floating-point notation with $\beta = 2$ and $e = 0$ and thus $\vec{a} \cdot \vec{b} \neq 0$ is computed.

This gives rise to the aforementioned difference in the result that the TFQMR algorithm yields on an x86 microarchitecture and on a GPU since the algorithm has a built-in termination criterion, if certain quantities become zero (see again p. 36 in [33]).

A possible solution to this floating-point related problem is to change the KKR formalism in such a way that the huge spread in the range of values is avoided, e.g. by changing the reference system in section 3.5.

A more promising and less comprehensive approach is to improve the accuracy of floating-point operations that are performed on the GPU while not sacrificing too much computational efficiency. One way of doing so could be to perform several independent *sub*-summations of values which are of similar order so that numerical accuracy is maintained. The results of these summations possibly do not differ as much as the individual summands and could therefore be added up in the end without loss of accuracy.

4.3.4. Benchmarks on Blue Gene/Q

Parts of this subsection have been published in Ref. [80]

In the context of the JUQUEEN Extreme Scaling Workshop 2017 [80] performance results for the latest version of KKR`nano` could be obtained on a BlueGene/Q (BG/Q) machine.

The tested version of KKR`nano` exclusively uses MPI collectives and two-sided MPI communication calls. Compute-intense linear algebra operations are performed by calling BLAS/LAPACK routines wherever applicable. File I/O is required only at application start-up and after the convergence of the self-consistency cycle. I/O operations are realized using Fortran direct-access files but an upgrade to MPI I/O is planned.
We perform all benchmarks for the helical magnet MnGe in B20 structure which requires a minimum of 8 atoms per unit cell and can easily reach supercell sizes of a million atoms when large magnetic superstructures need to be accommodated in the simulation volume.
We perform a series of weak scaling tests on different supercell sizes of MnGe. Our aim for these benchmarks is to treat several thousands of atoms self-consistently, i.e. estimate the runtime that about a hundred KKR iterations in a production calculation would require. However, for the purpose of obtaining benchmark results a single KKR iteration is sufficient.

The weak-scaling benchmarks are performed for MnGe in a collinear magnetic setup. KKR`nano` is compiled with the IBM XL compiler (-q64,-O3,-qstrict) and linked to the ESSLSMP linear algebra package. Here, three different hybrid parallelization schemes are used:

- The first runs are conducted with a task distribution of 16 MPI processes per node and 4 OpenMP threads per process (see Table 4.1). This setup is supposed to work best as it complies with the vendor's suggestion.
- Then, OpenMP threading is increased while the number of MPI processes is lowered. The total number of threads running (MPI × OpenMP) is kept constant at 64 matching the number of available hardware threads per node (see Table 4.2 and Table 4.3).

The atomic supercells are scaled from $8,192$ atoms (1024 BG/Q nodes) to $229,376$ atoms (28672 BG/Q nodes) according to the number of racks used. A physically correct description requires coverage of the magnetic properties of MnGe, i.e. both a spin-up and a spin-down calculation need to be done. Thus, we start twice as many MPI tasks as are needed to treat the non-magnetic system, e.g. for 8192 atoms in a $16 \times 8 \times 8$-supercell $16,384$ MPI ranks are used in Table 4.1. Runtimes are measured for the initialization, a single self-consistency iteration and result output. Each MPI process reads four **shared** binary direct-access files before commencing the self-consistency iterations. Two of them are index-files of the size of a few hundred kByte while the other two can grow with system size up to several GByte. The combined size of all files that are read in is roughly $N \times 0.5\,\mathrm{MBytes}$, where N is the number of atoms. In our benchmarks we do not write out a converged potential as we perform only a single self-consistency step. However, a single **shared** index file is set up at the very beginning before the self-consistency loop. This and the read-in of the four files mentioned above accounts for most of the time spent in I/O. In order not to hit the wall time limit for test runs of one hour, writing of the index file is omitted in the calculations on 24 and 28 racks, indicated with a (t) in Table 4.1.

Figure 4.6 shows the total runtime of a single self-consistency iteration for all three parallelization concepts in a double logarithmic plot. Obviously, a bipartite distribution of MPI and OpenMP load promotes shorter runtimes. We know from timing output that the increased slope for 8 racks and higher can be mainly attributed to Fortran direct-access I/O which does not scale well on a GPFS file system. The observation that the increase in runtime when moving from 8 to 28 racks is linked to the number of MPI tasks is a strong hint to this as the amount of file accesses is proportional to the number of MPI processes. The implementation of a more suitable I/O library (e.g., MPI I/O or SIONlib) is likely to solve this issue.

The TFQMR solver is expected to account for most of the computational work in KKR`nano` which is why linear scaling is of particular importance in this part of the code. Timings for it are depicted in Figure 4.7 (solid lines). Necessary MPI communication before the TFQMR part takes less than a second and is therefore not discussed here. Our benchmark results suggest to use a more MPI-oriented parallelization architecture in order to achieve best performance. However, it should be noted that the TFQMR solver kernel has been restructured to benefit from OpenMP threads. Shifting from one atom per MPI process towards e.g. 8 atoms per process reduces the memory requirements for the operator to be inverted as neighboring atoms can share matrix elements. Also the solver performance should increase using more OpenMP threads and less ranks per node, however, this effect cannot be observed here. A more thorough investigation and architecture-specific tuning would be needed.

In the KKR formalism, the electron density and the potential are connected via the Poisson equation. For large systems the Poisson solver contributes considerably to the overall runtime (see dashed lines in Figure 4.7). This is expected since the algorithm used in KKR`nano` scales quadratically with the number of atoms but does not have a major impact when mid-sized systems are investigated. However, there are ideas on how to restructure the Poisson solver towards a more favorable scaling behavior.

In order to get a more realistic impression, we extrapolated the total runtime for more than one self-consistency iteration. The extrapolated results for 10 iterations can be found in Figure 4.8. Here, the black line is not connecting between 16 and 24 racks as the bottleneck of final I/O has been omitted in the two calculations with $393,216$ and $458,752$ MPI ranks on 24 and 28 racks, respectively. As mentioned above, production runs may have of the order of hundred iterations. Multiplying the runtimes with a factor 100 would for some test cases exceed a wall-time of one day.

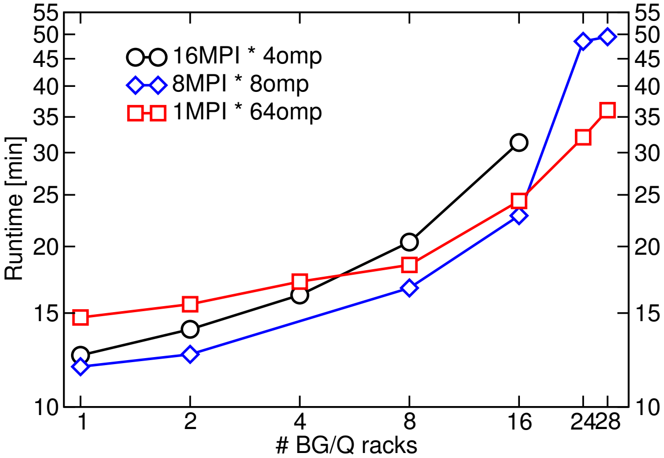

Figure 4.6.: Weak scaling of the total runtime for a single SCF iteration on MnGe using 1 to 16 BG/Q racks and three different parallelization schemes.

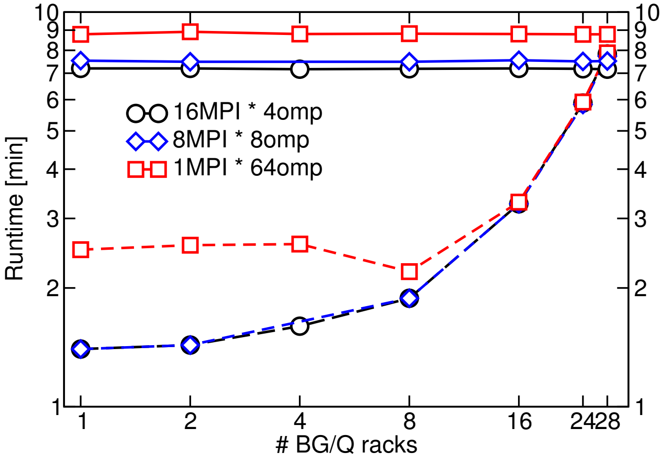

Figure 4.7.: MnGe: Time per iteration spent in the TFQMR solver (solid lines) and in the electrostatics solver (dashed lines).

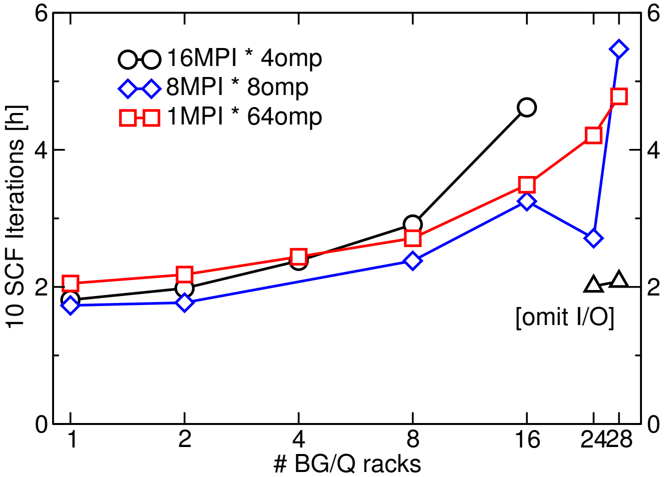

Figure 4.8.: Extrapolated weak scaling of the total runtime for 10 SCF iterations on MnGe. The triangles indicate the two runs with no final I/O operations.

Table 4.1.: Total runtime (Total), TFQMR solver runtime (TFQMR) and electrostatics solver runtime (ES) in weak scaling measurement series employing moderate OpenMP parallelization with 16 MPI ranks per node and 4 threads per process. Runtimes are given in seconds. (t) indicates the tuned version where final I/O is omitted.

Supercell	BG/Q nodes	MPI ranks	Threads	Total	TFQMR	ES
$16 \times 8 \times 8$	1,024	16,384	65,536	750	432	84
$16 \times 16 \times 8$	2,048	32,768	131,072	839	432	86
$16 \times 16 \times 16$	4,096	65,536	262,144	973	430	96
$32 \times 16 \times 16$	8,192	131,072	524,288	1223	431	113
$32 \times 32 \times 16$	16,384	262,144	1,048,576	1880	432	196
$32 \times 32 \times 24$	24,576	393,216	1,572,864	(t) 1077	431	353
$32 \times 32 \times 28$	28,672	458,752	1,835,008	(t) 1210	430	470

Table 4.2.: Total runtime (Total), TFQMR solver runtime (TFQMR) and electrostatics solver runtime (ES) in weak scaling measurement series employing balanced OpenMP parallelization with 8 MPI ranks per node and 8 threads per process. Runtimes are given in seconds.

Supercell	BG/Q nodes	MPI ranks	Threads	Total	TFQMR	ES
$16 \times 8 \times 8$	1,024	8,192	65,536	714	452	84
$16 \times 16 \times 8$	2,048	16,384	131,072	753	449	86
$16 \times 16 \times 16$	4,096	32,768	262,144	—	—	—
$32 \times 16 \times 16$	8,192	65,536	524,288	1003	449	113
$32 \times 32 \times 16$	16,384	131,072	1,048,576	1371	453	196
$32 \times 32 \times 24$	24,576	196,608	1,572,864	2910	450	350
$32 \times 32 \times 28$	28,672	229,376	1,835,008	2969	451	464

Table 4.3.: Total runtime (Total), TFQMR solver runtime (TFQMR) and electrostatics solver runtime (ES) in weak scaling measurement series employing massive OpenMP parallelization with 1 MPI rank per node and 64 threads per process. Runtimes are given in seconds.

Supercell	BG/Q nodes	MPI ranks	Threads	Total	TFQMR	ES
16 × 8 × 8	1,024	1,024	65,536	883	527	150
16 × 16 × 8	2,048	2,048	131,072	935	535	154
16 × 16 × 16	4,096	4,096	262,144	1031	528	155
32 × 16 × 16	8,192	8,192	524,288	1108	529	132
32 × 32 × 16	16,384	16,384	1,048,576	1461	528	198
32 × 32 × 24	24,576	24,576	1,572,864	1923	527	355
32 × 32 × 28	28,672	28,672	1,835,008	2162	527	473

5

Methodological Improvements to KKR`nano`

During the formation process of this thesis, several methodological improvements were added to KKR`nano` that were crucial to the investigation of the physical phenomena that should and shall be investigated in the future. In this chapter, these improvements are explained and their usefulness with regards to specific scientific questions is shown. We begin with a section on non-collinear magnetism and discuss how it was implemented by the author within the framework of KKR`nano`. Closely connected to this work is the consideration of relativistic effects. Section 5.2 gives a short overview on where these effects originate from and how our new version of KKR`nano` combines the scalar relativistic approximation with the treatment of spin-orbit coupling effects. In order to test this new implementation, the strong magnetic anisotropy in $\mathrm{IrMn_3}$ is investigated and results from a fully-relativistic code are used as a benchmark.

The chapter is concluded by some smaller methodological improvements that were newly introduced or re-established during the course of this PhD thesis. The Generalized Gradient Approximation (GGA) as well as the semi-core contour integration were added as new features. Also Lloyd's formula, which allows to determine the exact charge density, was re-established during the restructuring of KKR`nano`. In the last years it was neglected and had become dis-functional so that a rather time-consuming re-implementation needed to be done.

5.1. Non-collinear Magnetism in KKR

The need to distinguish between calculations where the atomic spins point collinearly in parallel or anti-parallel direction, i.e. order ferromagnetically or antiferromagnetically, and spins that point non-collinearly in arbitrary directions was already mentioned in section 2.4. Lounis gives an illustrative description of how non-collinear alignments of magnetic spins can be treated within KKR (cf. chapter 4 in [34]) and we adopt his scheme in the following. While both spin channels are decoupled in the collinear case, they mix for non-collinear calculations and the Kohn-Sham equations are therefore not

separable.
For convenience we rewrite them here as

$$-\nabla^2\phi_i^\alpha(\vec{r}) + \sum_\beta V_{\text{eff}}^{\alpha\beta}(\vec{r})\phi_i^{\alpha\beta}(\vec{r}) = \epsilon_i\phi_i^\alpha(\vec{r}), \tag{5.1}$$

where the effective potential is given as

$$V_{\text{eff}}^{\alpha\beta}(\vec{r}) = \delta^{\alpha\beta}\int \frac{n(\vec{r}')}{|\vec{r}-\vec{r}'|}d\vec{r}' + V_{\text{ext}}^{\alpha\beta}(\vec{r}) + V_{\text{XC}}^{\alpha\beta}(\vec{r}) \tag{5.2}$$

and the indices α and β stand for the spin directions ↑ or ↓ (cf. [34]). The exchange-correlation effects in the potential $V_{XC}^{\alpha\beta}$ are treated in the local spin frame which is introduced below.
This leaves us with the external potential $V_{\text{ext}}^{\alpha\beta}$ as the contribution that requires a treatment that is different from the collinear KKR formalism presented in chapter 3. It can be expressed as

$$V_{ext}^{\alpha\beta} = \begin{pmatrix} V_{\uparrow\uparrow} & V_{\uparrow\downarrow} \\ V_{\downarrow\uparrow} & V_{\downarrow\downarrow} \end{pmatrix} = \underline{\underline{1}} \cdot V(\vec{r}) + \underline{\underline{\sigma}} \cdot \vec{B}(\vec{r}) \tag{5.3}$$

with a diagonal contribution $V(\vec{r}) = {}^1\!/\!_2\mathrm{Tr}_s\underline{\underline{V}}(\vec{r})$ that consists of the trace in spin space over the potential and is familiar from the collinear definition and an additional contribution that is non-diagonal and couples different spin channels by a product a magnetic field $\vec{B}(\vec{r})$ and the Pauli matrices $\underline{\underline{\sigma}} = (\underline{\underline{\sigma}}_x, \underline{\underline{\sigma}}_y, \underline{\underline{\sigma}}_z)$. The individual Pauli matrices are defined as

$$\underline{\underline{\sigma}}_x = \begin{pmatrix} 0 & 1 \\ 1 & 0 \end{pmatrix} \quad \underline{\underline{\sigma}}_y = \begin{pmatrix} 0 & i \\ -i & 0 \end{pmatrix} \quad \underline{\underline{\sigma}}_z = \begin{pmatrix} -1 & 0 \\ 0 & 1 \end{pmatrix} \tag{5.4}$$

This definition differs from the common definition but is equally justified and used as such in the KKR codes developed in Jülich. Obviously, there is no off-diagonal contribution in $V_{ext}^{\alpha\beta}$, if $\vec{B}(\vec{r})$ points along the z-direction. This matches the prerequisites of a collinear calculation and hence the decoupling of the Kohn-Sham equations is restored in this case.
The fact that the effective potential can no longer be expressed in two decoupled equations naturally manifests in the structural Green functions, too. They are then given with off-diagonal elements in spin space and read

$$G_{LL'}^{nn',\alpha\beta} = \begin{pmatrix} G_{LL'}^{nn',\uparrow\uparrow} & G_{LL'}^{nn',\uparrow\downarrow} \\ G_{LL'}^{nn',\downarrow\uparrow} & G_{LL'}^{nn',\downarrow\downarrow} \end{pmatrix}. \tag{5.5}$$

The Dyson equation that allows to determine the structural Green functions in a non-collinear calculation is found to be

$$G_{LL'}^{nn',\alpha\beta}(E) = \delta_{\alpha\beta}G_{LL'}^{r,nn',\alpha\alpha}(E) + \sum_{n'',L'',L'''} G_{LL''}^{r,nn'',\alpha\alpha}(E)t_{L''L'''}^{n'',\alpha\beta}(E)G_{L'''L'}^{n''n',\alpha\beta}(E) \tag{5.6}$$

It should be noted that the reference Green function $G^{r,nn',\alpha\alpha}_{LL'}$ is still diagonal in spin-space and that the non-diagonality of $G^{nn',\alpha\beta}_{LL'}$ is the result of the non-diagonal t-matrices $t^{n'',\alpha\beta}_{L''L'''}$. They reflect the spin channel mixing in $V^{\alpha\beta}_{ext}$ which is given, if $\vec{B}(\vec{r})$ does not point along the z-axis. The expression for the spatial electronic density

$$n(\vec{r}) = -\frac{1}{\pi}\mathrm{Im}\mathrm{Tr}_s \int_{-\infty}^{E_F} dE\, G^{nn',\alpha\beta}_{LL'}(\vec{r},\vec{r},E) \tag{5.7}$$

slightly differs from the convention in eq. (3.10) as the trace is not only taken over the sites (nn') but also over the spin components $(\alpha\beta)$. The magnetization in each direction γ reads

$$m_\gamma(\vec{r}) = -\frac{1}{\pi}\mathrm{Im}\mathrm{Tr}_s \int_{-\infty}^{E_F} dE\, \underline{\underline{\sigma}}_\gamma G^{nn',\alpha\beta}_{LL'}(\vec{r},\vec{r},E) \tag{5.8}$$

following the prescription for the extraction of physical quantities in eq. (3.8).
The density matrix of a non-collinear system

$$\underline{\underline{\rho}}(\vec{r}) = \begin{pmatrix} \rho_{\uparrow\uparrow}(\vec{r}) & \rho_{\uparrow\downarrow}(\vec{r}) \\ \rho_{\downarrow\uparrow}(\vec{r}) & \rho_{\downarrow\downarrow}(\vec{r}) \end{pmatrix} = \frac{1}{2}\left[n(\vec{r}) + \underline{\underline{\sigma}}\cdot\vec{m}(\vec{r})\right] \tag{5.9}$$

is non-diagonal like the Green function and can be written as a composition of electronic density and magnetization.

In order to simplify the evaluation of the single-site problem one distinguishes between the global spin frame and the local spin frame. In the global spin frame the direction of every magnetic moment is given relative to a globally defined z-axis. If we assume that the magnetic moment is uniform within each Wigner-Seitz cell, a local frame of reference can be defined in which the local magnetic moment always points in z-direction (see Figure 5.1).
In case of non-collinear magnetization such a local spin frame is different for each cell. The reference system can be switched from local to global by a unitary rotation matrix

$$\underline{\underline{U}}(\theta,\phi) = \begin{pmatrix} \cos\frac{\theta}{2}e^{-\frac{i}{2}\phi} & -\sin\frac{\theta}{2}e^{-\frac{i}{2}\phi} \\ \sin\frac{\theta}{2}e^{\frac{i}{2}\phi} & \cos\frac{\theta}{2}e^{\frac{i}{2}\phi} \end{pmatrix}, \tag{5.10}$$

where θ and ϕ are the polar and the azimuthal angle. An operator A_{loc} which is known in the local frame can thus be easily transformed into its counterpart A_{glob} in the global fre via the algebraic connection

$$A_{\mathrm{glob}} = \underline{\underline{U}} A_{\mathrm{loc}} \underline{\underline{U}}^\dagger. \tag{5.11}$$

The advantage of being able to transform quantities from a local to a global frame and vice versa is that the single-site problem can then be solved in the local spin frame where there are neither off-diagonal contributions in the potential nor in the t-matrix:

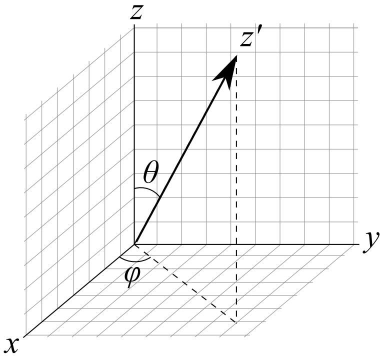

Figure 5.1.: Rotation of a magnetic moment (arrow) from the global frame given by the axis z to the local frame denoted by the different axis z'. The polar angles needed for the rotation are θ and ϕ

$$V_{\text{loc}} = \begin{pmatrix} V^{\uparrow} & 0 \\ 0 & V^{\downarrow} \end{pmatrix} \qquad t_{\text{loc}} = \begin{pmatrix} t^{\uparrow} & 0 \\ 0 & t^{\downarrow} \end{pmatrix} .$$

With a potential in diagonal form the solving techniques for collinear setups discussed in section 3.2 can be applied which yield the regular and irregular solutions $R^{\sigma s}_{L'L}/\bar{R}^{\sigma s}_{L'L}$ and $S^{\sigma s}_{L'L}/\bar{S}^{\sigma s}_{L'L}$. The standard procedure here is to solve the Lippmann-Schwinger equations with a few (usually less than five) Born iterations. As the convergence of this procedure is not guaranteed, if e.g. spin-orbit coupling effects are included, Zeller and Bauer proposed a scheme that solves the Lippmann-Schwinger equation directly (Chapter 5 in [22]). It is automatically used in KKR`nano` whenever spins are allowed to be non-collinear.

The multiple-scattering problem, i.e. the Dyson equation in eq. (5.6), is not solvable in the local picture as it generally contains contributions from different sites with individual local spin frames. Therefore, the Dyson equation is formulated with four spin components and the resulting structural Green functions consist of blocks that are of the size $2 \cdot (l_{\max}+1)^2 \times 2 \cdot (l_{\max}+1)^2$ instead of $(l_{\max}+1)^2 \times (l_{\max}+1)^2$ for a non-magnetic calculation.

5.2. Relativistic Full-potential Treatment

The KKR formalism for non-collinear magnetism which is discussed in the prior section is closely connected to relativistic effects, e.g. spin-orbit coupling (SOC), which can drive certain systems into a non-collinear state. Relativistic effects are not included in the standard DFT scheme but are usually treated as extensions to it. In the following we introduce the Dirac equation as the fully relativistic generalization of the Schrödinger equation and briefly discuss its most important properties. Subsequently, the scalar relativistic approximation is described and a scheme is presented which allows to treat SOC.

5.2.1. Dirac Equation

In 1928 Paul Dirac presented his famous equation that gives a fully relativistic description of the properties and the behavior of fermions [2]. While it is sufficient to only consider the non-relativistic Schrödinger equation for a variety of applications, there are effects, e.g. spin-orbit coupling, that can only be described in a relativistic framework. In the following a derivation of a solution to the fully relativistic problem is given and the term that gives rise to SOC is identified. This subsection is based on the scheme proposed in [81].

We begin with the single-site Dirac Hamiltonian which reads

$$H_{\mathrm{D}} = \frac{c}{i}\underline{\underline{\vec{\alpha}}}\vec{\nabla} + \frac{1}{2}\left(\underline{\underline{\beta}} - \underline{\underline{1}}\right) + \underline{\underline{V}}(\vec{r}), \tag{5.12}$$

where

$$\underline{\underline{\alpha_i}} = \begin{pmatrix} 0 & \underline{\underline{\sigma}}_i \\ \underline{\underline{\sigma}}_i & 0 \end{pmatrix} \qquad \underline{\underline{\beta}} = \begin{pmatrix} \underline{\underline{1}}^{2\times 2} & 0 \\ 0 & -\underline{\underline{1}}^{2\times 2} \end{pmatrix} \tag{5.13}$$

are the standard Dirac matrices. The potential can be split up into a spin-independent part and a spin-dependent part so that

$$V(\vec{r}) = V(r) + \underline{\underline{\beta}}\,\underline{\underline{\vec{\sigma}}}\vec{B}_{\mathrm{eff}}(\vec{r}) \tag{5.14}$$

Note, that in this derivation it is assumed that the potential terms are spherically symmetric and that $\vec{B}_{\mathrm{eff}}$ points along the z-axis, i.e. $\vec{B}_{\mathrm{eff}} = B_{\mathrm{eff}}(\vec{r})\hat{\vec{z}}$. An ansatz to a solution for the eigenvalue problem that the Hamiltonian in eq. (5.12) constitutes is given by

$$\Psi(\vec{r}, E) = \sum_{\Lambda} \begin{pmatrix} g_{\Lambda}(r, E)\chi_{\Lambda}(\hat{\vec{r}}) \\ if_{\Lambda}(r, E)\chi_{-\Lambda}(\hat{\vec{r}}) \end{pmatrix}, \tag{5.15}$$

where $\Lambda = (\kappa, \mu)$ and $-\Lambda = (-\kappa, \mu)$ are combined indices for the spin-orbit and magnetic quantum numbers κ and μ. g_{Λ} and f_{Λ} are the so-called the *major* and *minor* wave functions and $\chi_{\Lambda}(\hat{\vec{r}})$ denotes the spin-angular functions which are composed of complex spherical harmonics and Pauli spin functions.
This ansatz yields a set of radial differential equations

$$P'_{\Lambda} = -\frac{\kappa}{r}P_{\Lambda} + \left[\frac{E-V}{c^2} + 1\right]Q_{\Lambda} + \frac{B_{\mathrm{eff}}}{c^2}\sum_{\Lambda'}\left\langle\chi_{-\Lambda}\right|\sigma_3\left|\chi_{-\Lambda'}\right\rangle Q_{\Lambda'} \tag{5.16}$$

$$Q'_{\Lambda} = \frac{\kappa}{r}Q_{\Lambda} - \left[E-V\right]P_{\Lambda} + B_{\mathrm{eff}}\sum_{\Lambda'}\left\langle\chi_{\Lambda}\right|\sigma_3\left|\chi_{\Lambda'}\right\rangle P_{\Lambda'}, \tag{5.17}$$

if it is applied to eq. (5.12). $P' = \frac{d}{dr}P$ and $Q' = \frac{d}{dr}Q$ denote the spatial derivatives of $P(r, E) = g(r, E)r$ and $Q(r, E) = cf(r, E)r$. P is often referred to as the *large* component and Q as the *small* component. Note, that the radial dependencies of some quantities were dropped for the sake of readability. We restrict our investigation to the case where $\Delta l = |l' - l| = 0$ and $\Delta\mu = \mu' - \mu = 0$ and define the abbreviations

$$S_\Lambda = \frac{E - V}{c^2} + 1 + \frac{B_{\mathrm{eff}}}{c^2} \langle\chi_{-\Lambda}|\, \sigma_3 \,|\chi_{-\Lambda}\rangle\,, \tag{5.18}$$

$$T = E - V \tag{5.19}$$

and

$$B_{\Lambda\Lambda'} = B_{\mathrm{eff}} \langle\chi_\Lambda|\, \sigma_3 \,|\chi_{\Lambda'}\rangle\,. \tag{5.20}$$

Then, eq. (5.16) and eq. (5.17) can be simplified to

$$P'_\Lambda = -\frac{\kappa}{r}P_\Lambda + S_\Lambda Q_\Lambda \tag{5.21}$$

$$Q'_\Lambda = \frac{\kappa}{r}Q_\Lambda - TP_\Lambda + \sum_{\Lambda'} B_{\Lambda\Lambda'}P_{\Lambda'} \tag{5.22}$$

By inserting eq. (5.21) into eq. (5.22) we arrive at a second-order radial differential equation

$$P''_\Lambda = \frac{l(l+1)}{r^2}P_\Lambda - S_\Lambda T P_\Lambda + S_\Lambda \sum_{\Lambda'} B_{\Lambda\Lambda'}P_{\Lambda'} + \frac{S'_\Lambda}{S_\Lambda}\left[\frac{d}{dr} - \frac{1}{r} + \underbrace{\frac{\kappa+1}{r}}_{\mathrm{SOC}}\right]P_\Lambda, \tag{5.23}$$

where $P'' = \frac{d^2}{dr^2}$. A comparison with the Schrödinger equation shows that the last term on the right hand side does not have a non-relativistic counterpart. Furthermore, we can identify its κ-dependent part as the contribution that describes spin-orbit coupling as it is the only term that depends on the corresponding quantum number.

5.2.2. Scalar-relativistic Approximation

In order to obtain solutions for the Dirac Hamiltonian given in eq. (5.12) about twice as many states as needed for a non-relativistic calculation have to be taken into account [82]. This is why approximative schemes have been invented that only consider first-order contributions up to $\mathcal{O}(1/c^2)$ from the Dirac equation and neglect spin-orbit coupling. Hereby, important relativistic effects, e.g. change of the mass with velocity, can be retained.

In KKR`nano` the scalar relativistic approximation (SRA) of Drittler and Weinert [55] is adopted which has the advantage that spin-orbit coupling can subsequently be added in a perturbative scheme and thus its impact can be studied in our calculations. SRA re-establishes the angular momentum as a good quantum number so that the spin-orbit quantum number κ can be replaced by the angular momentum l as it is used in the non-relativistic derivations. For the sake of readability we do not mark the explicit energy dependence of the variables in the following.

To arrive at the desired approximation we consider eq. (5.23) without magnetic field ($B_{\Lambda\Lambda'} = 0$) and projected potentials ($S_\Lambda \to S_{LL'} = \frac{E\delta_{LL'} - V_{LL'}}{c^2} + 1$ and $T \to T_{LL'} = E\delta_{LL'} - V_{LL'}$). In combination with the neglect of SOC this yields (cf. eq. (13.11) in [83])

$$P''_{L''L'} = \frac{l''(l''+1)}{r^2} P_{L''L'} - S_{LL''}T_{LL''}P_{L''L'} + \frac{S'}{S}\left[\frac{d}{dr} - \frac{1}{r}\right] P_{L''L'} \tag{5.24}$$

Note, that in contrast to the Dirac equation, the combined angular momentum indices L are used which is legitimate since l and m are good quantum numbers, if SOC is neglected. Furthermore, we consider here the general case of full potential and hence two angular momentum indices are required. The second-order differential equation in eq. (5.24) can be rewritten as two first-order differential equations (see [83]) which then read

$$P'_{LL'} = \frac{1}{r} P_{LL'} + \sum_{L''} S_{LL''}(r) Q_{L''L'} \tag{5.25}$$

$$Q'_{L''L'} = -\frac{1}{r} Q_{L''L'} + \sum_{L''} U_{LL''}(r) P_{L''L'} \tag{5.26}$$

with coefficients

$$S_{LL'} = \left[\frac{E}{c^2} + 1\right] \delta_{LL'} - \frac{1}{c^2} V_{LL'} \tag{5.27}$$

$$U_{LL'} = \sum_{L''} S^{-1}_{LL''}(r) \delta_{L''L'} \frac{l''(l''+1)}{r^2} - \left[E\delta_{LL'} - V_{LL'}\right] \tag{5.28}$$

From this one can obtain the potential-free solutions by setting $V_{LL'} = 0$ which simplifies eq. (5.25) and eq. (5.26) to

$$\frac{d}{dr} P^0_l = \frac{1}{r} P^0_l + \left[\frac{E}{c^2} + 1\right] Q^0_l \tag{5.29}$$

$$\frac{d}{dr} Q^0_l = -\frac{1}{r} Q^0_l + \left[\frac{1}{\frac{E}{c^2} + 1} \frac{l(l+1)}{r^2} - E\right] Q^0_l. \tag{5.30}$$

Solutions to these equations can be easily derived [22] and are given as

$$\underline{R}^0_l = r \begin{pmatrix} j_l(\kappa r) \\ \frac{1}{2M_0} \partial_r j_l(\kappa r) \end{pmatrix}, \quad \bar{\underline{R}}^0_l = r \left(j_l(\kappa r), \quad -\tfrac{1}{2M_0} \partial_r j_l(\kappa r) \right)$$

$$\underline{S}^0_l = r \begin{pmatrix} h_l(\kappa r) \\ \frac{1}{2M_0} \partial_r h_l(\kappa r) \end{pmatrix}, \quad \bar{\underline{S}}^0_l = r \left(h_l(\kappa r), \quad -\tfrac{1}{2M_0} \partial_r h_l(\kappa r) \right), \tag{5.31}$$

where the relativistic mass of an electron in free space

$$M_0 = \frac{1}{2} + \frac{E}{2c^2} \tag{5.32}$$

and the coefficient $\kappa = \sqrt{E + \frac{E^2}{c^2}}$ are introduced.
The structure of the solutions is similar to those of the non-relativistic solutions given in eqs. (3.26) to (3.29). However, in SRA we have a large component (P_l^0) and a small component (Q_l^0) and the first (second) entry in each of the four solutions in eq. (5.31) solves our problem for the large (small) component, e.g. $j_l(\kappa r)$ is the regular right solution for the large component and $\frac{1}{2M_0}\partial_r j_l(\kappa r)$ the analogue for the small component.
As in eq. (3.21) we can calculate expansion coefficients for the Green function from the regular and irregular solutions. The coefficients are then written as 2x2-matrices

$$\underline{\underline{G}}_l^0(r,r') = \kappa\Theta(r'-r)\underline{R}_l^0(r)\bar{\underline{S}}_l^0(r') + \kappa\Theta(r-r')\underline{S}_l^0(r)\bar{\underline{R}}_l^0(r'). \tag{5.33}$$

with matrix products of $\underline{R}_l^0$, $\bar{\underline{S}}_l^0$, $\underline{S}_l^0$ and $\bar{\underline{R}}_l^0$. A general expression that is not restricted to the potential-free case can be given in close analogy.
It is straightforward to formulate Lippmann-Schwinger equations that connect the solutions in empty space to the solutions of a system with a given general potential. To this aim, we define the relativistic masses of an electron that is subject to a spherical potential

$$M(r) = \frac{1}{2} + \frac{E - V_{\text{sph}}}{2c^2}. \tag{5.34}$$

The term that needs to be inserted into the Lippmann-Schwinger equations which describes the difference between free space and $V_{LL'}$ then reads

$$\Delta\underline{\underline{V}}_{LL'}(r) = \begin{pmatrix} \left[\frac{1}{2M(r)} - \frac{1}{2M_0}\right]\frac{l(l+1)}{r^2} + V_{LL'}(r) & 0 \\ 0 & 2M(r) - 2M_0 \end{pmatrix}. \tag{5.35}$$

It is a diagonal 2x2-matrix, where the upper left part acts on the large relativistic component and the lower right part on the small relativistic component. Hence, we can write the Lippmann-Schwinger equations to obtain the solutions to the full potential problem as

$$\begin{aligned} \underline{R}_{LL'}(r,E) = {}& \underline{R}_L^0(r,E)\delta_{LL'} \\ & + 2M_0\kappa\underline{R}_L^0(r,E)\int_r^{R_{\max}} dr'\bar{\underline{S}}_L^0(r,E)\sum_{L''}\Delta\underline{\underline{V}}_{LL''}(r')\underline{R}_{L''L'}(r',E) \\ & + 2M_0\kappa\underline{S}_L^0(r,E)\int_0^r dr'\bar{\underline{R}}_L^0(r,E)\sum_{L''}\Delta\underline{\underline{V}}_{LL''}(r')\underline{S}_{L''L'}(r,E) \end{aligned} \tag{5.36}$$

for the regular solutions and

$$\begin{aligned}\underline{S}_{LL'}(r,E) &= \underline{S}^0_L(r,E)\beta_{LL'} \\ &\quad + 2M_0\kappa\underline{R}^0_L(r,E)\int_r^{R_{\max}} dr'\,\bar{\underline{S}}^0_L(r,E)\sum_{L''}\Delta\underline{\underline{V}}_{LL''}(r')\underline{S}_{L''L'}(r',E) \\ &\quad + 2M_0\kappa\underline{S}^0_L(r,E)\int_0^r dr'\,\bar{\underline{R}}^0_L(r,E)\sum_{L''}\Delta\underline{\underline{V}}_{LL''}(r')\underline{S}_{L''L'}(r,E)\end{aligned} \tag{5.37}$$

for the irregular solutions. In order to impose correct boundary conditions

$$\beta_{LL'} = 1 + 2M_0\kappa\int_0^{R_{\max}} dr'\,\bar{\underline{R}}^0_L(r',E)\sum_{L''}\Delta\underline{\underline{V}}_{LL''}(r')\underline{S}_{L''L'}(r',E) \tag{5.38}$$

is defined following the same philosophy as in section 3.2.

In practice, the eqs. (5.36) and (5.37) are not written as Fredholm integral equations but rewritten as Volterra integral equations and the problem is solved in a two-step procedure in which first the spherical part of the potential is included in the Lippmann-Schwinger equations while the non-spherical part is treated thereafter as an inhomogeneity (see [22]).
It should be noted that Zeller recently proposed to solve the full Dirac equation without making any approximations [84]. This feature is to be implemented in KKR`nano` but it requires a substantial effort which was beyond the scope of this thesis.

5.2.3. Spin-orbit Coupling

In the relativistic single particle theory spin and orbital degrees of freedom couple (see eq. (5.23)) which gives rise to interesting physical phenomena in magnetic and non-magnetic materials [85]. The first example of spin-orbit coupling (SOC) that is typically encountered in atomic physics is the fine structure splitting in hydrogen, where the p-levels $p_{\frac{1}{2}}$ and $p_{\frac{3}{2}}$ have different energy which they do not have in the Schrödinger picture without SOC.
Recently, SOC has begun to play an important role in the field of spin-orbitronics where single atomic spins or non-trivial topologically protected magnetic textures, e.g. skyrmions [17], are used to store information. While charge-based storage devices can store information merely based on the magnitude of charge they accumulate, spin-based storage devices rely on the atomic spin, which is a vector quantity, and therefore offers different ways of manipulating and processing information. SOC is of particular interest to this topic as it e.g. couples the spin direction to an applied electric field. An important example is the Spin Hall effect whose physical origin is SOC [86].

Derivation in the KKR Formalism

In the following it is shown how SOC is derived and dealt with in the KKR formalism (cf. [53]).
By inserting the Dirac spinor

$$|\Psi\rangle = \begin{pmatrix} \psi \\ \chi \end{pmatrix} \tag{5.39}$$

into the Schrödinger equation with an electromagnetic field we obtain the two equations

$$(E - mc^2 + eV(\vec{r}))\psi = \vec{\sigma} \cdot (c\vec{p} + e\vec{A}(\vec{r}))\chi \tag{5.40}$$

$$(E + mc^2 + eV(\vec{r}))\chi = \vec{\sigma} \cdot (c\vec{p} + e\vec{A}(\vec{r}))\psi \tag{5.41}$$

for the familiar large and small components. If we now combine both equations by inserting eq. (5.41) into eq. (5.40) we can obtain a lengthy expression which contains a term

$$\vec{\sigma} \cdot (\nabla V(r) \times \vec{p}) \tag{5.42}$$

$$= \frac{1}{r}\frac{dV(r)}{dr}\vec{\sigma} \cdot (\vec{r} \times \vec{p}) \tag{5.43}$$

$$= \frac{1}{r}\frac{dV(r)}{dr}\vec{\sigma} \cdot \vec{L} \tag{5.44}$$

that couples the spin matrices $\vec{\sigma}$ to the orbital moment $\vec{L}$ (see [85]). The spin-orbit potential that needs to be added to the Kohn-Sham equations which are given by eq. (2.1) is defined as

$$V_{\mathrm{SOC}} = \frac{1}{M(r)^2 c^2}\frac{1}{r}\frac{dV(r)}{dr}\vec{L} \cdot \vec{S}, \tag{5.45}$$

where we once again encounter the relativistic mass

$$M(r) = \frac{1}{2} + \frac{E - V(r)}{2c^2}. \tag{5.46}$$

as part of the prefactor. The evaluation of eq. (5.45) requires the knowledge of the Kohn-Sham potential

$$V(r) = V_{Z-e} + V_{e-e} \tag{5.47}$$

and its spatial derivative. $V(r)$ can be split up into a part that stems from the interaction of the electrons and the core (V_{Z-e}) and a part that originates from the mutual interaction of the electrons (V_{e-e}).
The electron-core contribution is given analytically as the classical Coulomb potential

$$V_{Z-e} = -\frac{2Z}{r}, \tag{5.48}$$

while the electron-electron contribution is an essential part of a DFT calculation and is therefore inherently available. The spatial derivative of the potential

$$\frac{dV(r)}{dr} = \frac{2Z}{r^2} + \frac{dV_{e-e}(r)}{dr} \tag{5.49}$$

is thus a sum of an analytical expression and a derivative that is calculated numerically from $V_{e-e}(r)$ whose values are known for specific radial grid points r_i.

The strength of SOC is determined mostly by the nuclear field which behaves like $\propto \frac{1}{r}\frac{dV}{dr} \propto -\frac{Z}{r^3}$. This dependency is the reason why SOC is more important in heavy elements with high nuclear charge than in light elements.

The remaining term in eq. (5.45) that needs to be evaluated is $\vec{L} \cdot \vec{S}$. In the KKR scheme spatial quantities are expanded in spherical harmonics. Therefore, an expression for the matrix elements of the coupling term in real spherical harmonics needs to be derived. It reads

$$\begin{pmatrix} \left(\vec{L} \cdot \vec{S}\right)^{\uparrow\uparrow}_{LL'} & \left(\vec{L} \cdot \vec{S}\right)^{\uparrow\downarrow}_{LL'} \\ \left(\vec{L} \cdot \vec{S}\right)^{\downarrow\uparrow}_{LL'} & \left(\vec{L} \cdot \vec{S}\right)^{\downarrow\downarrow}_{LL'} \end{pmatrix} = \frac{1}{2} \langle Y_L(\hat{\vec{r}})| \begin{pmatrix} L_z & L_- \\ L_+ & -L_z \end{pmatrix} |Y_{L'}(\hat{\vec{r}})\rangle \,, \tag{5.50}$$

where we used the common angular momentum operators L_z, L_+ and L_- to write $\vec{L} \cdot \vec{S}$ in a basis of real spherical harmonics $Y_L(\hat{\vec{r}})$. The off-diagonal elements indicate that SOC causes a mixing of spin channels. Details on how the expansion is performed can be found in [53].

What remains to be done is the correct addition of the perturbation V_{SOC} to the potential without SOC. In KKR`nano` this is done in the following way: First, the single-site problem is solved for the spherical part of the potential V_{sph} because SRA yields diverging terms in a full-potential approach. Then, the SOC potential ΔV_{SOC} and the non-spherical parts of the ordinary potential ΔV_{ns} are combined as

$$\begin{pmatrix} \Delta V(\vec{r})^{\uparrow\uparrow} & \Delta V(\vec{r})^{\uparrow\downarrow} \\ \Delta V(\vec{r})^{\downarrow\uparrow} & \Delta V(\vec{r})^{\downarrow\downarrow} \end{pmatrix} = \begin{pmatrix} \Delta V_{\mathrm{SOC}}(\vec{r})^{\uparrow\uparrow} & \Delta V_{\mathrm{SOC}}(\vec{r})^{\uparrow\downarrow} \\ \Delta V_{\mathrm{SOC}}(\vec{r})^{\downarrow\uparrow} & \Delta V_{\mathrm{SOC}}(\vec{r})^{\downarrow\downarrow} \end{pmatrix} + \begin{pmatrix} \Delta V_{\mathrm{ns}}(\vec{r})^{\uparrow\uparrow} & 0 \\ \Delta V_{\mathrm{ns}}(\vec{r})^{\downarrow\uparrow} & 0 \end{pmatrix} . \tag{5.51}$$

This perturbation potential can then be used to formulate Lippmann-Schwinger equations in the same manner as it is done in eqs. (5.36) and (5.37). If the wave functions are known, the change in the t-matrices caused by SOC can be determined straightforwardly (see again [53]). The implementation of this scheme in KKR`nano` is based on a prior implementation in another KKR code that was devised by Bauer and Zeller [22].

A look at eq. (5.45) also explains the fine structure splitting that can be observed in the hydrogen atom. The p-states ($l = 1$) can have the total angular momentum quantum number $j = |l - s|$ or $j = |l + s|$ so that there is a $p_{\frac{1}{2}}$- and a $p_{\frac{3}{2}}$-state. This difference manifests in the product

$$\vec{L} \cdot \vec{S} = \frac{1}{2} \left(j(j+1) - l(l+1) - s(s+1) \right) \tag{5.52}$$

, which enters in the SOC term and hence gives rise to two distinct energy levels that depend on the respective value of j.

5.2.4. Results for IrMn3

In order to test the implementation of non-collinear magnetism in combination with the scalar relativistic approximation and spin-orbit coupling, IrMn3 was chosen as an appropriate system.

IrMn3 in the cubic fcc phase is one of the most widely used industrial antiferromagnets and shows a frustrated triangular magnetic ground state known as the T1 state [87] that is shown in the left part of Figure 5.2. In this state (indicated by the dotted red arrows), the three Mn spins lay in one plane with a 120°-angle between them.

A KKR`nano` calculation of the system is initialized using a lattice constant of $a = 3.785$ Å with the three Mn spins pointing in the directions depicted by the black arrows. The spins are allowed to relax during the self-consistency cycle so that the magnetic energy is minimized. The converged result correctly predicts the T1 ground state. A comparison of the total energy of the collinear state and the non-collinear T1 state laying in the (111) plane yields that the latter is 0.9 eV lower in energy. This underlines the inherent non-collinear magnetic nature of the system.

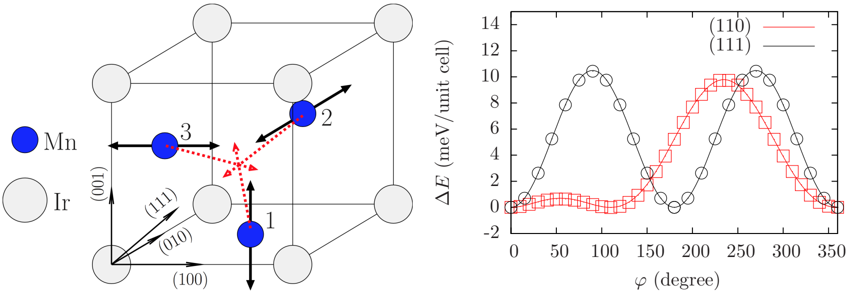

Figure 5.2.: Left: Triangular T1 state depicted in the IrMn3 unit cell. The magnetic moments (red) lay in the (111) plane and are separated by angle of 120 degrees. The solid arrows indicate the local easy axis for each Mn atom. Right: Magnetocrystalline anisotropy energy for rotations of the T1 state around the (110) and the (111) axis. The solid black line displays a fit to the function $K_{\text{eff}} \sin^2(\phi)$. Reprinted with permission from [87]. Copyright 2009 by the American Physical Society.

A subsequent investigation that is reasonable to test the correct implementation of our extensions to magnetism in KKR`nano` is a study of the magnetocrystalline anisotropiy energy (MCE) in IrMn3. This is done by usage of the *magnetic force theorem*, where we start from the converged T1 state and then perform a *one-shot* calculation, i.e. a single iteration instead of a fully self-consistent cycle. In each *one-shot* calculation all three Mn spins are rotated by the same specific rotation angle ϕ around the (111) axis. The differences in the single particle energies ΔE for different rotation angles then give a measure of the MCE landscape. This analysis is performed in steps of 10° for a

range $\phi = [0°, 180°]$ and the results are visualized in Figure 5.3. A strong magnetic anisotropy can be observed that is of the order of 10 meV per unit cell. Furthermore, KKR`nano` yields the correct symmetry properties, i.e. a rotation by 180° leads to a configuration that is symmetrically equivalent to the initial one.
We can compare our results to calculations following the same procedure that were performed by Szunyogh *et al.* [87]. Their results are adapted in Figure 5.2. For an antiferromagnetic system a simple orientation-dependence of the MCE can be derived that reads

$$E(\phi) = E(0) + K_{\text{eff}} \sin^2 \phi, \tag{5.53}$$

where K_{eff} is an effective uniaxial magnetic anisotropy constant. Fitting our data points to this function yields the curve shown in Figure 5.3 with $K_{\text{eff}} = 9.22$ meV. This nicely compares to the value of $K_{\text{eff}} = 10.42$ which was obtained by Szunyogh et al.. It should be noted though that they followed the same procedure in their calculation but used a fully relativistic KKR code while our data is obtained in the scalar relativistic approximation including spin-orbit coupling. However, this nicely shows that our approach can almost reproduce the results of a fully relativistic calculation.

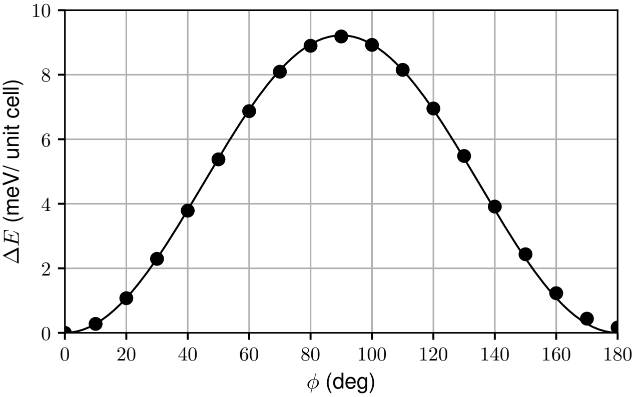

Figure 5.3.: Sum of band energies over rotation angle ϕ in (111) plane. The obtained values are fitted with a function $E(\phi) = E(0) + K_{\text{eff}} \sin^2 \phi$, where $K_{eff} =$ 9.22 meV.

5.3. Generalized Gradient Approximation (GGA)

The challenge of determining an exchange-correlation potential that describes the non-local nature of exchange and correlation effects only by the local electronic density and its gradient is briefly discussed in section 2.5. The local density approximation

(LDA) as well as the generalized gradient approximation (GGA) yield surprisingly accurate results for structural parameters as well as energy barriers and band gaps considering that it is a rather crude way of characterizing the quantum mechanical origin of exchange and correlation effects.

As part of this thesis an existing implementation of GGA was ported to KKR`nano` and extended by the PBEsol functional.

The idea of GGA was introduced by Langreth and Perdew in 1980 [88]. In the GGA picture, the LDA approximation is the first term of an asymptotic Taylor expansion in gradients of the density [89]. Considering only the first- and second-order term in this expansion leads to the second-order gradient-expansion approximation (GEA) which does not provide systematic improvements over LDA.

GGA goes beyond local approximations and defines the exchange-correlation energy as

$$E_{xc}^{GGA} = \int f(n^{\uparrow}(\vec{r}), n^{\downarrow}(\vec{r}), \nabla n^{\uparrow}(\vec{r}), \nabla n^{\downarrow}(\vec{r})) d\vec{r} \tag{5.54}$$

in its most general form. Different GGA functionals f have been proposed and the achievable accuracy strongly depends on the kind of material and the physical properties that are of interest, e.g. atomic bonding energies.

Exchange and correlation effects are a result of the interaction between an electron and the exchange-correlation hole that exists around the electron due to the Pauli principle. The hole is characterized by a deficit of one electron,

$$\int_0^{\infty} dR\, 4\pi R^2 n_{xc}(\vec{r}, R) = -1, \tag{5.55}$$

with an electron located at $\vec{r}$. R denotes the distance to the electron. The exchange-correlation hole density $n_{xc}(\vec{r}, R)$ can be subdivided into the exchange hole density $n_x(\vec{r}, R)$ and the correlation hole density $n_c(\vec{r}, R)$. The former satisfies

$$n_x(\vec{r}, R) \leq 0 \tag{5.56}$$

and integrates to -1, whereas $n_c(\vec{r}, R)$ integrates to zero. These two conditions are met by the LDA functional which is important to the explanation of its success. The refinement that GGA offers is then that it improves the description of the hole close to the electron by adding the Taylor expansion terms of the density. This in turn worsens the description of the hole further away from the electron. These spurious contributions and oscillations for large R need to be cut off. The numerous proposed GGA functionals all adopt this goal but differ in the way it is met and in the additional constraints that are imposed.

In the following the most popular functional named PBE and its variation for more accurate equilibrium properties in densely-packed solids PBEsol are derived.

PBE

The GGA functional PBE was introduced in 1996 by Perdew, Burke and Ernzerhof [40]. Contrarily to other functionals, e.g. PW91 [42], it satisfies only the conditions which are energetically significant. It can therefore be derived rather easily and is the *de facto* standard in present-day DFT calculations.
All parameters of PBE are fundamental constants except for the exchange-correlation energy of the uniform electron gas. Correlation and exchange energies are determined separately and the expression for the correlation energy reads

$$E_c^{GGA} = \int d^3r\, n \left[\epsilon_c^{\text{unif}}(r_s, \zeta) + H(r_s, \zeta, t)\right], \tag{5.57}$$

where r_s is the local Wigner-Seitz radius ($n = 3/4\pi r_s^3 = k_F^3/3\pi^2$), $\zeta = (n_\uparrow - n_\downarrow)/n$ is the relative spin polarization and $t = |\nabla n|/2\phi k_s n$ is a dimensionless density gradient in which $\phi(\zeta) = \left[(1+\zeta)^{2/3} + (1-\zeta)^{2/3}\right]/2$. The Thomas-Fermi screening wave number is used as $k_s = \sqrt{4k_F/\pi}$. $\epsilon_c^{\text{unif}}(r_s, \zeta)$ is the correlation energy of the uniform electron gas.
The gradient contribution H is constructed from three conditions:

1. For slow variations of the dimensionless density gradient ($t \to 0$) H shall equal the second-order gradient expansion [90]

   $$H \to 2\beta\phi^3 t^2, \tag{5.58}$$

   where $\beta \approx 0.066725$.

2. For rapid variations $t \to \infty$ the correlation energy in eq. (5.57) shall vanish and therefore

   $$H \to -\epsilon_c^{\text{unif}}(r_s, \zeta) \tag{5.59}$$

   must hold.

3. The logarithmic singularity that $\epsilon_c^{\text{unif}}(r_s, \zeta) \propto \ln(r_s)$ has in the high-density limit $r_s \to 0$ [91] must cancel out and E_c^{GGA} has to scale to a constant [92]. This is achieved by demanding that

   $$H \to 2\gamma\phi^3 \ln t^2 \tag{5.60}$$

   in the high density limit, where $\gamma = 0.031091$.

All three conditions are met by the ansatz

$$H = 2\gamma\phi^3 \ln\left[1 + \frac{\beta}{\gamma} t^2 \left(\frac{1 + At^2}{1 + At^2 + A^2t^4}\right)\right], \tag{5.61}$$

where

$$A = \frac{\beta}{\gamma}\left[\exp\left(-\epsilon_C^{\text{unif}}/(2\gamma\phi^3)\right) - 1\right]^{-1} \tag{5.62}$$

In the limit $t \to 0$ the t^4-term can be neglected and the first contribution to the Taylor expansion of $\ln\left[1+\frac{\beta}{\gamma}t^2\right]$ reads $\frac{\beta}{\gamma}t^2$ which leads to the behavior demanded by eq. (5.58). For $t \to \infty$ we can write

$$H = 2\gamma\phi^3 \ln\left[1+\frac{\beta}{\gamma}t^2\left(\frac{1+At^2}{1+At^2+A^2t^4}\right)\right] \tag{5.63}$$

$$\approx 2\gamma\phi^3 \ln\left[1+\frac{\beta}{\gamma}\left(\frac{t^2+At^4}{At^2+A^2t^4}\right)\right] \tag{5.64}$$

$$= 2\gamma\phi^3 \ln\left[1+\frac{\beta}{\gamma}\frac{1}{A}\right] \tag{5.65}$$

$$= -\epsilon_c^{\text{unif}} \tag{5.66}$$

and arrive at eq. (5.59).

The contribution of the exchange energy reads

$$E_x = \int d^3r\, n\epsilon_x^{\text{unif}} F_x(s) \tag{5.67}$$

In order to recover the excellent approximation of the exchange energy by LDA for small density variations [93], i.e. $s = |\nabla n|/2k_F n \to 0$, the constraint

$$F_x(s) \to 1 + \mu s^2 \tag{5.68}$$

shall hold, where $\mu = \beta(\pi^2/3) = 0.21951$. The Lieb-Oxford inequality [94] defines a lower boundary

$$E_x\left[n_\uparrow, n_\downarrow\right] \leq E_{xc}\left[n_\uparrow, n_\downarrow\right] \leq -1.679e^2 \int d^3r\, n^{4/3}. \tag{5.69}$$

for the indirect part of the Coulomb energy, i.e. exchange and correlation. The combination of eq. (5.68) and eq. (5.69) is satisfied by the simple ansatz

$$F_x(s) = 1 + \kappa - \kappa/(1 + \mu s^2/\kappa), \tag{5.70}$$

where $\kappa = 0.804$.

Exchange and correlation contributions can be combined and written as a single functional that needs to be convoluted with the exchange energy of a uniform electron gas and the electronic density to yield the exchange-correlation energy for PBE

$$E_{xc}^{GGA}[n_\uparrow, n_\downarrow] = \int d^3r\, n\epsilon_X^{unif}(n) F_{xc}(r_s, \zeta, s). \tag{5.71}$$

In the limit $F_{xc}(r_s,\zeta,s) \to F_{xc}(r_s,\zeta,0)$ the LDA approximation is recovered. In the high-density limit ($r_s \to 0$) exchange dominates and $F_{xc}(r_s,\zeta,s) \to F_x(\zeta,s)$, whereas in the low-density limit ($r_s \to \infty$) correlation non-locality dominates.

PBEsol

In 2008 Perdew et al. [41] presented the functional PBEsol which was designed to correct PBE in such a way that equilibrium properties of densely packed solids are improved. Its implementation is straightforward since it differs from PBE merely by the two coefficients μ and β.
It is important to note that no GGA functional can yield both accurate atomization and total energies and lattice parameters or surface energies. Hence, a trade-off is inevitable and a decision for either must be made depending on which properties are paramount.
The fundamental idea behind PBEsol is to restore the correctness of the density gradient expansion of the exchange in the first order approximation for the uniform electron gas.

We rewrite eq. (5.68) for convenience

$$F_x(s) = 1 + \mu s^2 + ..., \tag{5.72}$$

where the choice of $\mu = 0.1235$ (cf. $\mu = 0.21951$ in PBE) yields the correct exact linear response for the uniform electron gas. This alone leads to much better lattice constants.
The change of μ requires an alteration of the parameter β which enters as a parameter in the expression for the correlation energy in eq. (5.57) via the definition in eq. (5.61). For a GGA correlation functional one can write

$$E_c^{GGA} = \int d^3r\, n \left[\epsilon_c^{\text{unif}}(r_s, \zeta) + \beta t^2(r) + ...\right] \tag{5.73}$$

up to the first order contribution. For weakly-varying valence-electron densities as they are found in densely packed solids, LDA gives a proper response to an applied weak potential. In order to completely retain this feature the condition

$$\mu = \pi^2 \beta / 3 \tag{5.74}$$

must be fulfilled. However, β is chosen as $\beta = 0.046$ which deviates from the value 0.0375 which the condition suggests. This is done in favor of better surface energies as comparisons with meta-GGA functionals, i.e. functionals that also make use of the orbital kinetic energies, have shown.

Comparison

KKR`nano` currently features the GGA functionals PBE, PBEsol and PW91 [89]. We conducted an evaluation of the equilibrium lattice constants that each of the functionals predicts and compared them with experimental values for Cu and Ge in Table 5.1. Cu is a text book example for a DFT calculation. LDA tends to overbind the atoms in a solid which results in underestimating the equilibrium lattice parameters while PBE shows a tendency to slightly overestimate them. PBEsol corrects this *overshooting* and yields a value that matches experiment.

The case of Ge is an exception from the empirical knowledge that GGA usually does a better job at predicting the lattice constant. Here, all GGA functionals overestimate the lattice parameter while the result obtained with LDA matches the experimental value.

	LDA	PW91	PBE	PBEsol	exp.
a_{Cu} (a_0)	6.7	6.9	6.9	6.8	6.82
a_{Ge} (a_0)	10.7	> 10.9	> 10.9	10.9	10.7

Table 5.1.: Equilibrium lattice constants for Cu (a_{Cu}) and Ge (a_{Ge}) produced with LDA, PW91, PBE and PBEsol exchange-correlation functionals in KKR`nano` and the experimental lattice parameters.

5.4. Lloyd's Formula

The angular momentum components of the Green function in the KKR method can only be considered up to a certain cut-off (c.f. section 3.5) in L and L'. This inevitably causes an inaccuracy in the calculation of the electronic charge density which in turn leads to an incorrect Fermi energy.

This does not constitute a problem in metals as it will only result in a small shift of the Fermi level. However, in band-gap materials, i.e. insulators and semiconductors, correct charge normalization is of outmost importance. Even small errors cause the Fermi level to move into the valence or conduction band and the material is falsely treated as a metal. Lloyd's formula [95] is a method to calculate the integrated density of states exactly. It implicitly sums over all angular momenta and thereby avoids the problem mentioned above. The variant of Lloyd's formula presented in the following is the one which is implemented in KKR`nano` and was derived by Zeller [96].

In KKR the electronic density is obtained via

$$\rho(\vec{r}+\vec{R}^n) = -\frac{2}{\pi}\mathrm{Im}\int_{-\infty}^{\infty} dE\, f(E,E_F,T)\, G(\vec{r}+\vec{R}^n,\vec{r}+\vec{R}^n,E), \tag{5.75}$$

where $f(E,E_F,T)$ is the Fermi-Dirac distribution, $G(\vec{r}+\vec{R}^n,\vec{r}+\vec{R}^n,E)$ is the multiple-scattering Green function and $\vec{r}+\vec{R}^n$ denote cell-centered coordinates. The integral needs to be evaluated numerically so we rewrite it as

$$\rho(\vec{r}+\vec{R}^n) = -\frac{2}{\pi}\sum_i \mathrm{Im}\left[w_i G(\vec{r}+\vec{R}^n,\vec{r}+\vec{R}^n,E_i)\right] \tag{5.76}$$

with suitably chosen complex valued integration points E_i and weights w_i. The Fermi energy E_F is determined by the energetically highest-lying integration point and can be obtained straightforwardly by imposing the condition that the total charge Q, which is identical to the number of valence electrons in the system, equals the integral over the spatial electronic density in all cells:

$$Q = \sum_n \int_n d\vec{r}\, \rho(\vec{r} + \vec{R}^n). \tag{5.77}$$

The error that is made when determining E_F like this stems from the fact that the Green function

$$\tilde{G}(\vec{r} + \vec{R}^n, \vec{r} + \vec{R}^n, E) = \sum_L^{l_{\max}} R_L^n(\vec{r}, E) S_L^n(\vec{r}, E) + \sum_{LL'}^{l_{\max}} R_L^n(\vec{r}, E) G_{LL'}^{nn'}(E) R_{L'}^n(\vec{r}, E) \tag{5.78}$$

is truncated in angular momentum space above $l = l_{\max}$. Here, we used eq. (3.44) in a modified form for equal space arguments. The truncation results in a spurious charge density

$$\tilde{\rho}(\vec{r} + \vec{R}^n) = -\frac{2}{\pi} \sum_i \operatorname{Im}\left[\tilde{w}_i \tilde{G}(\vec{r} + \vec{R}^n, \vec{r} + \vec{R}^n, E_i)\right] \tag{5.79}$$

with integration points $\tilde{E}_i$ and weights $\tilde{w}_i$ that differ from the correct values E_i and w_i in eq. (5.76) Therefore, also the total charge

$$\tilde{Q} = \sum_n \int_n d\vec{r} \tilde{\rho}(\vec{r} + \vec{R}^n) \tag{5.80}$$

is associated with an error and $\tilde{E}_F$ is not correct in band-gap materials.
Lloyd's formula [97] can correct this shortcoming by providing an exact expression

$$N(E) = N^r(E) + \frac{2}{\pi} \sum_n \ln\det\left|\Delta\alpha_{LL'}^n(E)\right| - \frac{2}{\pi} \ln\det\left|\delta_{LL'}^{nn'} - G_{LL'}^{r,nn'}(E) \Delta t_{LL'}^{n'}(E)\right| \tag{5.81}$$

for the total charge in the system $N(E)$. $N^r(E)$ is the total charge and $G_{LL'}^{r,nn'}(E)$ the Green function of an arbitrary reference system, e.g. free space. $\Delta t_{LL'}^{n'}(E)$ denotes the difference of the t-matrices of the actual and this reference system. The α matrix describes the different behavior of the single-scattering solutions R_L^n and J_L^n at the origin:

$$R_L^n(\vec{r}, E) = \sum_{L'} J_{L'}^n(\vec{r}, E) \alpha_{L'L}^n(E) \qquad r \to 0. \tag{5.82}$$

With the exact expression from eq. (5.81) the total charge and with it the correct Fermi level can be correctly calculated as

$$Q = \operatorname{Im} \int_{\infty}^{\infty} dE f(E, E_F, T) n(E) = \sum_i \operatorname{Im}\left[w_i n(E_i)\right], \tag{5.83}$$

where $n(E)$ denotes the energy derivative of $N(E)$. In a periodic crystal with an infinite number of atoms eq. (5.81) is applied in reciprocal space and reads

$$\begin{aligned} N(E) = &N^r(E) + \frac{2}{\pi}\sum_{\nu} \ln\det\left|\Delta\alpha^{\nu}_{LL'}(E)\right| \\ &- \frac{2}{\pi V_{BZ}}\int_{BZ} d\vec{k}\, \ln\det\left|\delta^{\nu\nu'}_{LL'} - G^{r,\nu\nu'}_{LL'}(\vec{k},E)\Delta t^{\nu'}_{LL'}(E)\right|. \end{aligned} \tag{5.84}$$

Here, ν and ν' are restricted to the basis sites in the unit cell and the integral in the last term is over the Brillouin zone.
Lloyd's formula only yields the total charge in a system but does not deliver the spatially resolved charge density. The correct Fermi level which is obtained in eq. (5.83) does not make up for the incorrect Green function that enters in eq. (5.79). This deficiency can be compensated by the introduction of normalization factors λ_i that are applied along the integration contour so that we arrive at an adjusted density of states

$$\rho_\lambda(\vec{r}+\vec{R}^n) = -\frac{2}{\pi}\sum_i \lambda_i \mathrm{Im}\left[w_i\tilde{G}(\vec{r}+\vec{R}^n,\vec{r}+\vec{R}^n,E_i)\right]. \tag{5.85}$$

The factors are determined by the condition

$$\frac{2}{\pi}\sum_i \lambda_i \mathrm{Im}\left[w_i\tilde{G}(\vec{r}+\vec{R}^n,\vec{r}+\vec{R}^n,E_i)\right] = \mathrm{Im}\left[w_i n(E_i)\right], \tag{5.86}$$

where the exact energy derivative $n(E)$ obtained with Lloyd's formula and the spurious Green function $\tilde{G}(\vec{r}+\vec{R}^n,\vec{r}+\vec{R}^n,E_i)$ enter. A correct choice of the λ_i makes both sides of the equation equivalent. The adjusted density of states ρ_λ is thus correctly normalized and provides the correct total charge

$$\sum_n \int_n d\vec{r}\rho_\lambda(\vec{r}+\vec{R}^n) = Q. \tag{5.87}$$

In practice an additional step needs to be made due to the infinite increase of the real part of $\tilde{G}$ with $l_{\max} \to \infty$. This causes the λ_i to vanish in that limit which is unphysical since the inclusion of higher angular momentum components should improve the accuracy of $\tilde{G}$ in eq. (5.85) so that a smaller amount of correction is needed and $\lambda_i \to 1$. Well-behaving λ_i can be obtained by subtracting the contribution of a suitably chosen reference system from both sides of eq. (5.86). We choose the potential-free space (see section 3.3) as reference with the Green function

$$G^0(\vec{r}+\vec{R}^n,\vec{r}+\vec{R}^n,E) = \sum_L^{\infty} J_L(\vec{r},E)H_L(\vec{r},E) \tag{5.88}$$

The analogue to eq. (5.86) is then

$$\frac{2}{\pi}\sum_i \mathrm{Im}\left[w_i\tilde{G}^0(\vec{r}+\vec{R}^n,\vec{r}+\vec{R}^n,E_i)\right] = \mathrm{Im}\left[w_i n^0(E_i)\right] - \mathrm{Im}\left[w_i\Delta n^0(E_i)\right], \tag{5.89}$$

where $n^0(E)$ denotes the energy derivative of the integrated density of states $N^0(E)$ for free space which is a quantity that can be exactly calculated. The sum over l is divided into a part up to $l_{\max}$ and a part

$$\mathrm{Im}\left[w_i \Delta n^0(E_i)\right] = \frac{2}{\pi} \sum_n \int_n d\vec{r}\,\mathrm{Im}\left[w_i \sum_{l>l_{\max}}^{\infty} J_L(\vec{r}, E_i) H_L(\vec{r}, E_i)\right] \tag{5.90}$$

that covers $l > l_{\max}$. Its contribution to the total charge is very small (less than 0.0006 electrons per atom). It is therefore justified to use the following two-step scheme to calculate the factors λ_i. We add eq. (5.89) to eq. (5.86) and neglect the contribution from eq. (5.90) so that

$$\begin{aligned} &\frac{2}{\pi} \sum_i \lambda_i^\star \mathrm{Im}\left[w_i \tilde{G}(\vec{r} + \vec{R}^n, \vec{r} + \vec{R}^n, E_i)\right] \\ &\qquad = \mathrm{Im}\left[w_i n(E_i)\right] + \mathrm{Im}\left[w_i n^0(E_i)\right] - \frac{2}{\pi} \sum_i \mathrm{Im}\left[w_i \tilde{G}^0(\vec{r} + \vec{R}^n, \vec{r} + \vec{R}^n, E_i)\right] \end{aligned} \tag{5.91}$$

with preliminary factors $\lambda_i^\star$. These preliminary factors are then scaled by the ratio $Q/Q^\star$ which yields

$$\lambda_i = \lambda_i^\star \frac{Q}{Q^\star}. \tag{5.92}$$

Q is the exact charge calculated with Lloyd's formula while $Q^\star$ is the charge calculated according to eq. (5.85) with λ_i being replaced by $\lambda_i^\star$. Thus, the factors λ_i are the essential quantities in correcting the charge normalization error, that is made in KKR due to angular momentum truncation, by means of Lloyd's formula.

An example of the importance of Lloyd's formula in KKR`nano` for non-metals is shown in Figure 5.4. The density of states of the perovskite $SrTiO_3$ has a band-gap since this material is a semiconductor. It plays an important role in the research on resistive switching materials and is considered to be a candidate for a new non-volatile solid-state memory [98]. With Lloyd's formula the Fermi level is placed in the band-gap where it is supposed to be. Without Lloyd's formula $SrTiO_3$ appears to be a metal with a high density of Ti states at the Fermi energy.

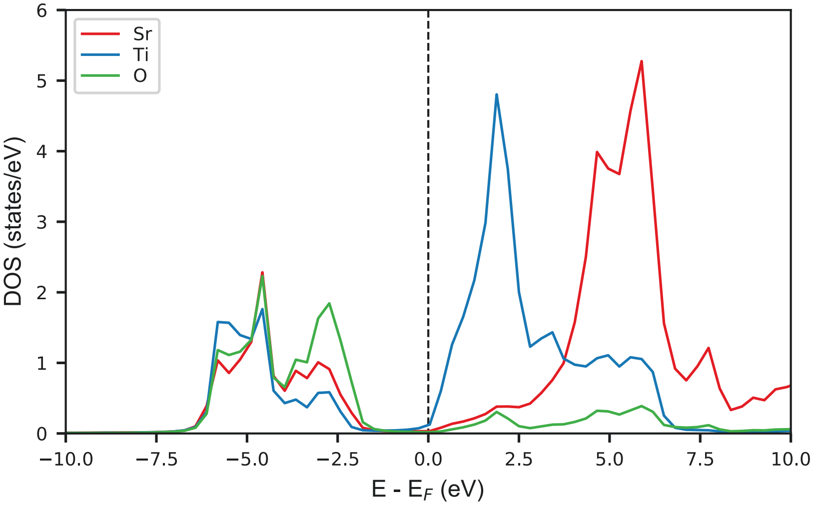

(a)

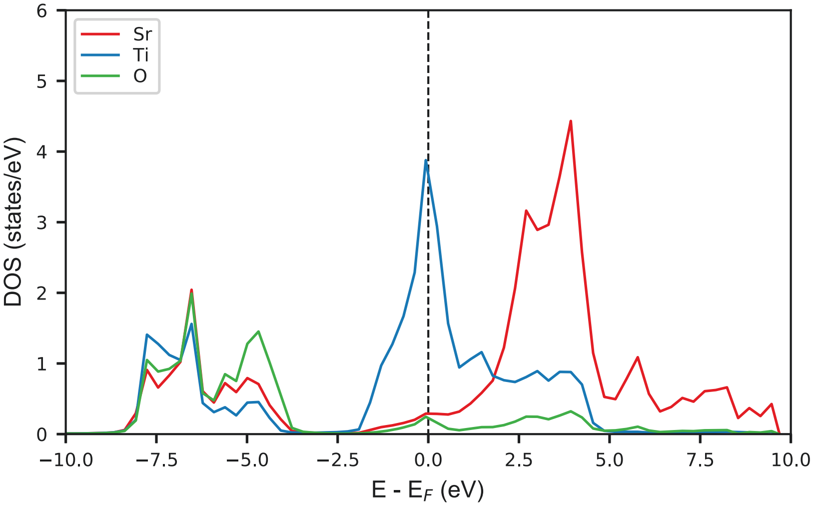

(b)

Figure 5.4.: Density of states for the resistive switching material $SrTiO_3$ with (a) and without (b) the use of Lloyd's formula. The Fermi level is indicated by a dashed line. With Lloyd's formula it is positioned correctly on the edge of the band gap of the semiconducting $SrTiO_3$. If Lloyd's formula is not used, it lies deep inside the conduction band so that the system is treated like a metal.

5.5. Semi-core Contour

At the beginning of this subsection about the introduction of a *semi-core* energy contour it should be remembered from section 3.1 that the energetically low-lying core states are treated differently from the higher-lying valence states. The crucial complex energy contour in eq. (3.8) covers only the valence states. Some states in certain materials cannot be unambiguously identified as core or valence states. Higher-lying core states have wave functions that significantly reach out of the muffin-tin region and therefore require a treatment similar to valence states [83]. In order to account for this one can define another contour integration in addition to the valence contour. This semi-core contour is only over the states that cannot be assigned either to the group of core states or the group of valence states. The newly added feature in KKR`nano` is inspired by an existing implementation in the juKKR code.

Bulk Ge has high-lying 3d-states that are positioned closely to the valence band (see Figure 5.5). They qualify as semi-core states and can be treated with the scheme that is described in the following.

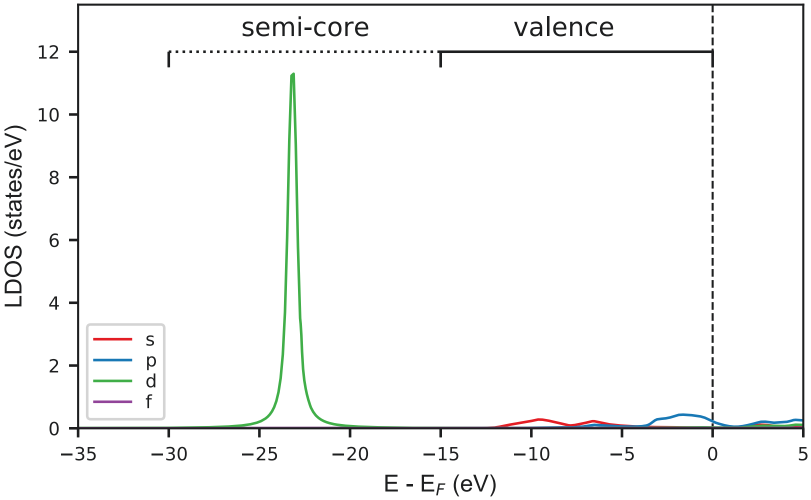

Figure 5.5.: Semi-core contour (dotted line) and valence contour (solid line) depicted in an energy-resolved density of states for Ge with high-lying 3d core states. The Fermi level is indicated by a dashed line. The strong localization of the 3d state is evident.

The simplest way of dealing with semi-core states would be to extend the valence contour to include them. However, this requires more energy points in the complex

contour integration or a sacrifice of accuracy. The semi-core contour offers a more elegant way to calculate the contribution of the strongly localized semi-core states. We take advantage of the fact that the number of electrons that are to be found within the contour is an integer and known exactly. In case of Ge 10 electrons are in the 3d-state. With that knowledge we can afford to trade accuracy for performance, i.e. use a sparser k-mesh and less energy points than in the valence contour.
The imprecise charge $\tilde{Q}$ that is obtained by this sloppy procedure is rounded to the nearest integer value $\lfloor\tilde{Q}\rceil$, e.g. $\tilde{Q} \approx 9.8$ and $\lfloor\tilde{Q}\rceil = 10$ in Ge. Then, a factor

$$f_{SC} = \frac{\lfloor\tilde{Q}\rceil}{\tilde{Q}} \tag{5.93}$$

can be determined which is multiplied with the integration weights in the semi-core contour in the next iteration to ensure that the charge it contains has the correct integer value. The procedure is similar to the one in Llyod's formula (c.f. section 5.4) and we define $\tilde{w}_{\mathrm{SC},i}$ as the uncorrected weights and $w_{\mathrm{SC},i} = f_{SC}\tilde{w}_{\mathrm{SC},i}$ as corrected weights. Then, we rewrite the charge density in the semi-core contour as

$$\rho_{\mathrm{SC}}(\vec{r} + \vec{r}^n) = -\frac{2}{\pi} \sum_i \mathrm{Im}\left[w_{\mathrm{SC},i} G(\vec{r} + \vec{R}^n, \vec{r} + \vec{R}^n, E_{\mathrm{SC},i})\right] \tag{5.94}$$

with integration points $E_{\mathrm{SC},i}$. It leads to the correct integer semi-core contour charge

$$Q_{\mathrm{SC}} = \sum_n \int_n d\vec{r} \tilde{\rho_{\mathrm{SC}}}(\vec{r} + \vec{R}^n). \tag{5.95}$$

6

Atomistic Spin Dynamics

Density Functional Theory (DFT) is formulated as a static theory that does not include dynamic effects. This is quite obvious when looking at the Kohn-Sham equations in eq. (2.4) since they depend neither explicitly nor implicitly on time. In this chapter we show that there is a time-dependent analogon, usually referred to as TD-DFT, that can capture dynamical effects, e.g. the precession of an atom's magnetic moment. The concept of atomistic spin dynamics (ASD) is introduced as a cheaper alternative to the much more costly prospect of solving the TD-DFT equations in real time. Furthermore, due to the complexity of TD-DFT only very short time scales of the order of femtoseconds can be accessed [99, 100]. ASD is based on the Landau-Lifshiftz-Gilbert equation that describes the motion of an atomic moment under an effective magnetic field. The usage of the Landau-Lifshitz-Gilbert equation in the ASD framework was initially proposed by Antropov et al. [101].

More comprehensive elucidations on the matter can be found in textbooks [102] and PhD theses [22, 103] in the field. For the derivation of the Landau-Lifshitz-Gilbert equation and the magnetic Hamiltonian we adopt the approach of Eriksson et al. (cf. [102]).

6.1. Landau-Lifshitz-Gilbert Equation

It is the aim of this section to derive the Landau-Lifshitz-Gilbert (LLG) equation which models the effects of a magnetic field on magnetic materials. It is based on an equation originally proposed by Landau and Lifshitz which was later modified by Gilbert [104]. The equation reads

$$\frac{d\vec{m}_i}{dt} = -\gamma_L \vec{m}_i \times \vec{B}_{\text{eff},i} - \gamma_L \frac{\alpha}{|\vec{m}_i|} \vec{m}_i \times \left[\vec{m}_i \times \vec{B}_{\text{eff},i} \right] \tag{6.1}$$

and describes the dynamical behaviour of a magnetic moment $\vec{m}_i$ under an effective magnetic field $\vec{B}_{eff,i}$. The first term on the right-hand side accounts for the moment's precession that is directed perpendicular to the direction of the moment and the direction of the effective field, i.e. it causes the moment to precess on a circular path around $\vec{B}_{\text{eff},i}$. The second term is called the *damping term* as it yields a vector that damps the precession of $\vec{m}_i$ and eventually causes it to realign with the effective magnetic field. The prefactor

$$\gamma_L = \frac{\gamma}{1+\alpha^2} \tag{6.2}$$

is determined by the gyromagnetic ratio γ and the Gilbert damping coefficient α.

In order to derive the LLG equation we write the spin-dependent Kohn-Sham Hamiltonian

$$\begin{aligned} H_{KS}^{\alpha\beta} &= -\nabla^2\delta^{\alpha\beta} + V_{\text{eff}}^{\alpha\beta}(\vec{r},t) \\ &= -\nabla^2\delta^{\alpha\beta} + V_0(\vec{r},t)\delta^{\alpha\beta} + \hat{\sigma}\cdot\vec{B}_{\text{eff}}(\vec{r},t) \end{aligned} \tag{6.3}$$

by using the formulation in eq. (2.15). However, in this notation the effective potential $V_{\text{eff}}^{\alpha\beta}(\vec{r},t)$ can be time-dependent and is divided into a diagonal potential $V_0(\vec{r},t)$ and a magnetic potential $\hat{\sigma}\cdot\vec{B}_{\text{eff}}(\vec{r},t)$.

The time evolution of a quantum mechanical system is governed by the time-dependent Schrödinger equation

$$i\frac{\partial\psi(\vec{r},t)}{\partial t} = H_{KS}\psi(\vec{r},t) \tag{6.4}$$

$$-i\frac{\partial\psi^\dagger(\vec{r},t)}{\partial t} = \left[H_{KS}\psi(\vec{r},t)\right]^\dagger \tag{6.5}$$

which is needed in the following both in its standard form and conjugated form. We can calculate the time evolution of a spin density $\vec{s} = \psi_i^\dagger(\vec{r},t)\hat{s}\psi_i(\vec{r},t)$ by

$$\begin{aligned} \frac{\partial\vec{s}(\vec{r},t)}{\partial t} &= \frac{\partial}{\partial t}\left[\psi_i^\dagger(\vec{r},t)\hat{s}\psi_i(\vec{r},t)\right] = \psi_i^\dagger(\vec{r},t)\hat{s}\frac{\partial\psi_i(\vec{r},t)}{\partial t} + \frac{\partial\psi_i^\dagger(\vec{r},t)}{\partial t}\hat{s}\psi_i(\vec{r},t) \\ &= \frac{1}{2i}\left\{\psi_i^\dagger(\vec{r},t)\hat{\sigma}H_{KS}\psi_i(\vec{r},t) - \left[H_{KS}\psi_i(\vec{r},t)\right]^\dagger\hat{\sigma}\psi_i(\vec{r},t)\right\} \\ &= \frac{1}{4i}\nabla\cdot\left\{\left[\hat{\sigma}\nabla\psi_i^\dagger(\vec{r},t)\right]\psi_i(\vec{r},t) - \psi_i^\dagger(\vec{r},t)\hat{\sigma}\nabla\psi_i(\vec{r},t)\right\} - \gamma\vec{s}\times\vec{B}_{eff}(\vec{r},t) \\ &= -\nabla\cdot\vec{J}_s - \gamma\vec{s}\times\vec{B}_{\text{eff}}(\vec{r},t), \end{aligned} \tag{6.6}$$

where $\hat{s} = \frac{1}{2}\hat{\sigma}$ is the quantum mechanical spin operator. A thorough derivation of the equation above is given in appendix A.1. The result can be written as the sum of the divergence of the so-called spin current density

$$\vec{J}_s = \frac{1}{4i}\left\{\left[\hat{\sigma}\nabla\psi_i^\dagger(\vec{r},t)\right]\psi_i(\vec{r},t) - \psi_i^\dagger(\vec{r},t)\hat{\sigma}\nabla\psi_i(\vec{r},t)\right\}. \tag{6.7}$$

From here on we consider this term to be negligible since it is usually only relevant, if certain transport phenomena, e.g. spin transfer torque effects, are investigated. The crucial term is the last one which is very similar to the first term in eq. (6.1). Dropping the prefactor for a moment they can be brought into complete agreement by assuming that the atomic magnetic moments are localized and not itinerant. Then, the magnetic moment can be spatially integrated around the atomic positions and our reference changes from continuum to discrete atomic positions $\vec{s}(\vec{r},t) \rightarrow \vec{m}_i(t)$. This is also known as the atomic moment approximation.

We can make another approximation similar to the Born-Oppenheimer approximation (c.f. section 2.1) by assuming that $\vec{B}_{\mathrm{eff},i}$ changes slowly with time on a scale of 10^{-12} s or longer compared to the magnetic dynamics of the electrons which are much faster and change within 10^{-16} s. This is an adiabatic approximation and allows to solve eq. (6.6) straightforwardly by considering $\vec{B}_{eff,i}$ as being independent of the characteristic electronic time scales.

While the precession term in eq. (6.1) is easy to derive from first principles, the damping term was initially introduced as a phenomenological parameter. An *ab initio* derivation of the latter requires the consideration of spin-orbit coupling or the full Dirac equation. Therefore, we restrict its explanation to qualitative arguments. Obviously, a real magnetic system is always connected to an environment and energy dissipation is inevitable. This obstructs the conservation of individual atomic spins and the spin will eventually align with the effective magnetic field. The damping term can also be written and included in the LLG equation as

$$\frac{d\vec{m}_i}{dt} = -\gamma \vec{m}_i \times \vec{B}_{\mathrm{eff},i} - \frac{\alpha}{|\vec{m}_i|} \vec{m}_i \times \frac{d\vec{m}_i}{dt}. \tag{6.8}$$

This is the so-called Gilbert damping which is used more often in the spin dynamics community. However, for the case of isotropic damping it can be shown that the damping terms in eq. (6.1) and eq. (6.8) are equal. The damping parameter α can be extracted from an ab initio calculation but is in many calculations just set to a constant value that is deduced from experiment.

6.2. The Magnetic Hamiltonian

The considerations above led to eq. (6.1) and gave an explanation of its constituents. However, it was not clarified how $\vec{B}_{\mathrm{eff},i}$ is obtained in practice. This shall be done in the following based on the remarks in [102].

$\vec{B}_{\mathrm{eff},i}$ can be written as the derivative of an effective spin Hamiltonian H such that

$$\vec{B}_{\mathrm{eff},i} = \frac{\partial H}{\partial \vec{m}_i}. \tag{6.9}$$

H shall contain all relevant magnetic interactions that need to be considered in an atomistic spin model for a given system so that it reads

$$H = H_{\mathrm{Heis}} + H_{\mathrm{MCE}} + H_{\mathrm{DM}} + H_{\mathrm{dd}} + H_{\mathrm{ext}}. \tag{6.10}$$

This is called the extended Heisenberg Hamiltonian and it comprises the interatomic Heisenberg interaction, the magnetocrystalline anisotropy, the Dzyaloshinskii-Moriya (DM) interaction [105, 106], the magnetostatic dipole-dipole interaction and the Zeeman energy. The contribution from the standard Heisenberg model is given by the well-known Hamiltonian

$$H_{\text{Heis}} = -\frac{1}{2}\sum_{i\neq j} J_{ij}\vec{m}_i \cdot \vec{m}_j \tag{6.11}$$

which is a sum over neighbouring isotropic exchange interactions J_{ij} multiplied with the product of the two magnetic moments $\vec{m}_i$ and $\vec{m}_j$ on site i and j, respectively. Positive (negative) sign of J_{ij} favours ferromagnetic (antiferromagnetic) coupling between the two spins. The Heisenberg contribution is in most cases the largest summand in eq. (6.10) and is crucial in determining the critical temperature of the system, i.e. the temperature above which a magnet system becomes paramagnetic. While the Heisenberg contribution alone already yields quite accurate results for many materials, further terms are necessary to capture the magnetic behaviour more precisely.

The DM interaction

$$H_{\text{DM}} = -\frac{1}{2}\sum_{i,j} \vec{D}_{ij} \cdot (\vec{m}_i \times \vec{m}_j) \tag{6.12}$$

has only recently been recognized as very important because it plays a decisive role in thin metallic films with broken inversion symmetry, e.g. the underlying creation mechanism for topological solitons known as skyrmions in various layered systems is the DM interaction [17]. Note, that DM interaction exclusively exists in systems with non-negligible spin-orbit coupling and that it favours a magnetic configuration, where the moments point in perpendicular directions.

Another contribution arises from the magnetocrystalline anisotropy which has its origin in the coupling between magnetic moments and the crystal lattice. Spin-orbit coupling imposes a preferred orientation of the magnetization in certain crystallographic directions, i.e. the magnetocrystalline anisotropy energy (MCE) has a minimum, if spins are aligned along those directions. This favourable direction is called the *easy* axis while the energetically most unfavourable direction is referred to as the *hard* axis. The MCE can be uniaxial or cubic depending on the magnetic material. The uniaxial form reads

$$H_{\text{uni}} = -\sum_{i} \left\{ K_i^1 \left(\hat{e}_i \cdot \hat{e}_i^k\right)^2 + K_i^2 \left(\hat{e}_i \cdot \hat{e}_i^k\right)^4 + ...\right\}, \tag{6.13}$$

where K_i^n are the uniaxial anisotropy constants and $\hat{e}_i^k$ is the axis of the uniaxial anisotropy, i.e. the preferred direction of magnetization, while $\hat{e}_i = \vec{m}_i/|\vec{m}_i|$ is the unit vector of the magnetic moment. Usually, it is sufficient to restrict the expansion in eq. (6.13) to the first order and only consider K_i^1. In case of a cubic symmetry the MCE is given by

$$H_{\text{cub}} = -\sum_{i} \left\{ K_i^1 \left(e_{x,i}^2 e_{y,i}^2 + e_{x,i}^2 e_{z,i}^2 + e_{y,i}^2 e_{z,i}^2\right) + K_i^2 \left(e_{x,i}^2 e_{y,i}^2 e_{z,i}^2\right) + ...\right\}. \tag{6.14}$$

The dipole-dipole interaction H_{dd} is routinely neglected, if the isotropic exchange interaction is dominant. If we neglect K_i^2, it is obvious that for $K_i^1 < 0$ the *easy* axes are the x-, y- and z-axes while for $K_i^1 > 0$ the *easy* axes are given by the diagonal directions, e.g. $\hat{e}_i = \frac{1}{\sqrt{3}}(1,1,1)$.

6.3. Extraction of Magnetic Interaction Parameters from KKR

The coefficients which enter in eqs. (6.11) to (6.14) are not known a priori. They can either be estimated by analyzing experimental results or can be obtained from first-principles calculations. The latter is particularly convenient within the KKR formalism since the Green function is known which contains all the information that is necessary to extract coupling parameters with the aid of eq. (3.8).

We focus on the extraction of the isotropic Heisenberg exchange coupling constants J_{ij} and the Dzyaloshinskii-Moriya interaction coupling constants $\vec{D}_{ij}$ and neglect other terms for a moment. Liechtenstein et al. presented a simple formalism that allows to calculate the J_{ij} [107] which was later generalized by Udvardi et al. [108, 109] so that also the $\vec{D}_{ij}$ can be obtained.

The generalized Heisenberg Hamiltonian (cf. eq. (6.10)) with neglected dipolar interaction reads in tensorial form

$$H = \hat{e}_i \underline{\underline{J}} \hat{e}_j = \hat{e}_i \begin{pmatrix} J_{ij}^{xx} & J_{ij}^{xy} & J_{ij}^{xz} \\ J_{ij}^{yx} & J_{ij}^{yy} & J_{ij}^{yz} \\ J_{ij}^{zx} & J_{ij}^{zy} & J_{ij}^{zz} \end{pmatrix} \hat{e}_j, \tag{6.15}$$

where $\hat{e}_j$ and $\hat{e}_j$ is the orientation of the magnetic moment on site i and j, respectively. It can be decomposed into

$$\underline{\underline{J}} = J_{ij} \underline{\underline{1}} + \underline{\underline{J}}^S + \underline{\underline{J}}^A \tag{6.16}$$

with the diagonal isotropic Heisenberg contributions

$$J_{ij} = \frac{1}{3} \mathrm{Tr} \underline{\underline{J}}, \tag{6.17}$$

a traceless symmetric part

$$\underline{\underline{J}}^S = \frac{1}{2} \left(\underline{\underline{J}} + \underline{\underline{J}}^T \right) - J_{ij} \underline{\underline{1}} \tag{6.18}$$

and an antisymmetric part

$$\underline{\underline{J}}^A = \frac{1}{2} \left(\underline{\underline{J}} - \underline{\underline{J}}^T \right). \tag{6.19}$$

We can thus write the Hamiltonian combining all three contributions as

$$H = J_{ij} \hat{e}_i \cdot \hat{e}_j + \hat{e}_i \underline{\underline{J}}^S \hat{e}_j + \vec{D}_{ij} \left(\hat{e}_i \times \hat{e}_j \right), \tag{6.20}$$

where the DM interaction is defined as a vectorial quantity that is connected to the tensor elements of $\underline{\underline{J}}$ by

$$D_{ij}^{x} = \frac{1}{2}\left(J_{ij}^{yz} - J_{ij}^{zy}\right), \quad D_{ij}^{y} = \frac{1}{2}\left(J_{ij}^{xz} - J_{ij}^{zx}\right), \quad D_{ij}^{z} = \frac{1}{2}\left(J_{ij}^{xy} - J_{ij}^{yx}\right). \tag{6.21}$$

The tensor $\underline{\underline{J}}$ can be obtained through the method of infinitesimal rotations [108]. Here, the magnetic moment is infinitesimally rotated around the axis α which leads to a perturbation of the local potential ΔV_i^{α}. This perturbation can again be utilized to calculate the concomitant energy shift that corresponds to the exchange coupling tensor and one can write

$$\underline{\underline{J}} = J_{ij}^{\alpha\alpha'} = -\frac{1}{\pi}\mathrm{Im}\int_{E_b}^{\infty} \mathrm{d}E\,\mathrm{Tr}\left[\Delta V_i^{\alpha}\, G_{ij}\, \Delta V_j^{\alpha'}\, G_{ji}\right] \tag{6.22}$$

following the specification given by eq. (3.8).
For instance, if the tensor elements J_{ij}^{xz} is to be calculated, an infinitesimal rotation of the magnetic moment i is made around the x-axis that results in a perturbation ΔV_i^{x} and another rotation around the z-axis for the magnetic moment at site j yields ΔV_j^{z}. The Green function G_{ij} is known from the solution of eq. (3.44). Then, the tensor element J_{ij}^{xz} can be calculated straightforwardly by integrating over the energy contour. Our approach to obtain the model parameters is advantageous since the full electronic Green function is a byproduct of our method and we can therefore access it without any additional costs. In comparison to other methods it should also be noted that with our approach we can extract the parameters in a one-shot calculation for each magnetization axis, while usage of e.g. the generalized Bloch theorem requires more computational effort.

7

Magnetic Textures in B20 Compounds

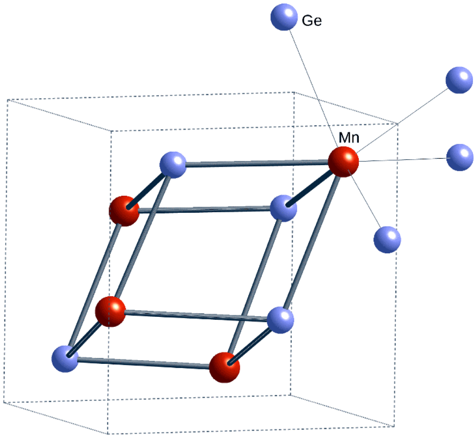

Figure 7.1.: Illustration of the elementary unit cell of B20-MnGe with the Mn-atoms colored in red and the Ge-atoms colored in blue. Other B20 materials adopt the same basic structure with slightly varying structural parameters. Reprinted with permission from [110]. Copyright 2014 by the American Physical Society.

The focus of this chapter is on the investigation of complex magnetic textures in B20 materials. Most of the current research activity dealing with magnetism in B20 compounds is closely connected to the field of skyrmionics. Skyrmions are two-dimensional magnetization solitons, i.e. two-dimensional magnetic structures localized in space, protected by a topologically non-trivial magnetization texture, which have particle-like properties. These days, they constitute one of the most active subjects in the field of magnetism, because such topological solitons can serve as information-carrying particles that are small-sized and stable up to room temperature [111, 112]. That is why special attention has been paid lately to cubic B20-type compounds with broken lattice inversion symmetry, where skyrmion phases have been observed experimentally [113]. In fact, the B20 material MnSi was the first material in which the formation of skyrmions was experimentally observed [15].

In this chapter, results from both magnetic models and KKR`nano` calculations are presented. The investigations are directed at the B20 compounds MnGe and FeGe as well as $\mathrm{Mn}_{1-x}\mathrm{Fe}_x$Ge-alloys.
B20 materials order in a cubic structure that is described by the $P2_13$ space group. This space group is noncentrosymmetric, which means that there is no lattice inversion symmetry. The atoms are located at the Wyckoff positions (u,u,u), $(1/2-u, 1-u, 1/2+u)$, $(1-u, 1/2+u, 1/2-u)$ and $(1/2+u, 1/2-u, 1-u)$, where u is a constant value that is determined for each atom type, e.g. $u_{Mn} = 0.14$ and $u_{Ge} = 0.84$ for B20-MnGe [110]. Hence, there are 8 atoms in total in a simple B20 unit cell. The B20 germanides that are of interest in our analysis consist of a transition metal like Mn or Fe and the metalloid Ge. An exemplary visualization of the B20-MnGe unit cell is given in Figure 7.1.

7.1. Basic Properties of MnGe

B20-MnGe was identified as a good candidate material to be investigated with the new version of KKR`nano` (see chapter 4), which was developed as part of this thesis and now contains the feature of non-collinear magnetism and spin-orbit coupling.
In a recent study [28], it was found by transmission electron microscopy that 3D magnetic objects exist in B20-MnGe. The authors of [28] came to the conclusion that their data indicates a cubic lattice of skyrmionic hedgehogs and anti-hedgehogs (see Figure 7.2a) with a rather short pitch of about 3-6 nm which can be observed up to a temperature of 170 K. The singularity at the center of the texture exists only in the micromagnetic description since the atomic magnetic moment of the atom, which is located at the center, remains finite [114].

Findings by Kanazawa et al. suggest that this lattice is set up by a superposition of three orthogonal helical structures also referred to as 3Q state [24]. Here, the local magnetization is determined by the provision

$$\vec{M}(\vec{r}) = \begin{pmatrix} \sin qy + \cos qz \\ \sin qz + \cos qx \\ \sin qx + \cos qy \end{pmatrix}, \tag{7.1}$$

where $q = \frac{2\pi}{\lambda}$ is the wavenumber given in terms of the helical wavelength λ and x, y and z are the spatial coordinates within the unit cell. Note, that $\vec{M}(\vec{r})$ is not normalized. In contrast to other systems exhibiting a similar magnetic phase, the rather short helical wavelength in B20-MnGe allows one to perform density functional theory (DFT) calculations with KKR`nano`.
B20-MnGe is currently the subject of extensive investigation [25, 28, 116–118]. This is mainly inspired by the discovery of skyrmions as small information-carrying particles

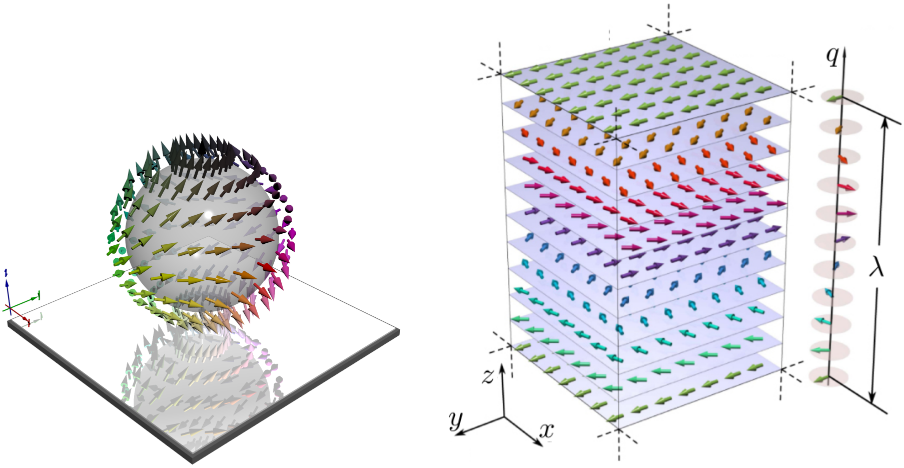

(a) (b)

Figure 7.2.: Magnetic textures that are found experimentally in B20-MnGe: (a) Magnetic anti-hedgehog texture that is wrapped around a singularity at the center. (b) Helical spin spiral that propagates in (001) direction. Reprinted from [115] with modifications and licensed under CC BY 3.0.

that could potentially be used in spintronic devices [17]. However, no large-scale DFT calculation seems to have been performed, yet.

At present there is a lack of a convincing explanation of what is observed in experiment. Research in the framework of micromagnetic models identified both magnetic frustration (RKKY interaction) [30] as well as spin-orbit coupling induced Dzyaloshinskii-Moriya (DM) interaction as potentially crucial to a better understanding [29].

While the 3Q state certainly constitutes the most interesting non-trivial magnetic texture in B20-MnGe, there are also reports that the magnetic ground state in this system is actually a helical spiral (see Figure 7.2b) [119] which was observed up to a temperature of 170 K [120]. These two observations are clearly contradictory and it has not yet been explained how both can coexist within the same material. The helical spin spiral in B20-MnGe forms along the (001) direction and therefore the magnetization is described by the relation

$$\vec{M}(\vec{r}) = \begin{pmatrix} \cos qz \\ -\sin qz \\ 0 \end{pmatrix} . \tag{7.2}$$

In the following, we refer to this as the 1Q state. In Figure 7.3 the result of a density of states calculation for the ferromagnetic 8-atomic unit cell with KKR`nano` is shown. It is clearly visible that the magnetic properties of MnGe are governed by the 3d-states of the Mn. The spin splitting gives rise to a magnetic moment of roughly 2 μ_B/f.u.. The other channels as well as the Ge states do not contribute significantly to the density of states at and around the Fermi level.

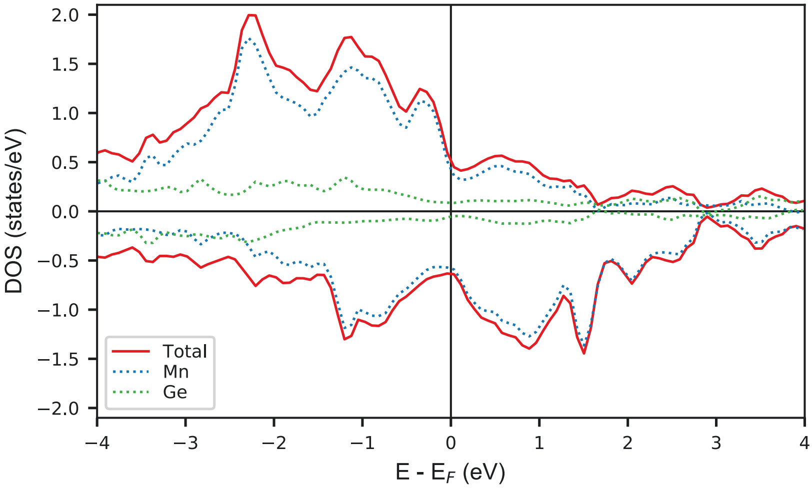

Figure 7.3.: Energy-resolved density of states for B20-MnGe. The contributions of the Mn bands and the Ge bands are plotted separately with dotted lines while the combined density of both the Mn and the Ge states is indicated by a solid line. The majority (minority) spin channel is denoted by positive (negative) y-values. The spin splitting, which gives rise to the magnetic moment of the Mn atoms, is clearly recognizable.

7.1.1. High-spin/Low-spin Transition

In 2012 Rößler [121] predicted a pressure-induced magnetic transition from a high-spin state (HS) to a low-spin (LS) state in B20-MnGe. He used the FPLO code [122], a full-potential local orbital method, with the PBE functional and performed additional calculations with LDA to compare with. In [121] the lattice constant is varied between 4.2 and 5.0 Å to simulate the exertion of pressure on the sample. His calculations yield an HS state that has a magnetic moment of a bit more than $2\mu_B/f.u$ and a LS state with a magnetic moment of only $1\mu_B/f.u$. If LDA is used to account for exchange-correlation effects, the global minimum of the total energy is found for the LS state, while for PBE the lowest total energy coincides with a high magnetic moment and hence with the HS state.

Rößler's prediction was experimentally observed in 2014 by Deutsch et al. [31]. They confirmed that at a pressure of about 6 GPa the magnetic moment rapidly drops by more or less the amount that Rößler's calculations had predicted. They also report that the helical ordering in the material collapses above an applied pressure of 10 GPa.

We investigate this phenomenon with KKR`nano`, i.e. calculate the change of the total energy as well as that of the magnetic moment over a lattice parameter that is varied from 4.6 to 4.8 Å. The calculations are performed in the scalar-relativistic approximation with ferromagnetically aligned spins and do not include the effects of spin-orbit coupling. As exchange-correlation functionals we choose LDA according to the scheme of Vosko, Wilk and Nusair [123] and PBEsol. A grid of $14 \times 14 \times 14$ k-points in combination with a broadening temperature of 800 K is used. The resulting curves are visualized in Figure 7.4. The total energies for LDA and PBEsol have the shape of a parabola around the energetic minimum. The equilibrium lattice constant is determined by the minimum of the total energy, which is found to be at 4.65 Å in LDA and 4.76 Å in PBEsol. In comparison to experiment, where 4.8 Å has been reported [110], PBEsol clearly yields the more accurate lattice constant for B20-MnGe. The same calculation also sheds light on the behaviour of the magnetic moment under a variation of the lattice constant. As can be seen in the lower part of Figure 7.4, the magnetic moment of each Mn atom becomes larger with increasing lattice constant. The main difference between LDA and PBEsol is the location of the crossover region in which the moments increase abruptly and the system goes into the HS state. For PBEsol it is found around 4.65 Å while it is slightly below 4.7 Å for LDA. Furthermore, it is remarkable that the magnetic moments per Mn atom differ a lot for the equilibrium lattice constant of LDA and PBEsol. Here, LDA predicts a magnetic moment/f.u. that is a bit larger than 1 μ_B, where instead PBEsol prefers a value of almost exactly 2 $\mu_B/f.u.$. Experimentally, a magnetic moment between 1.6 $\mu_B/f.u.$ and 2.3 $\mu_B/f.u.$ was measured [119].

A closer look reveals that there are actually two parabola-like energy curves for each functional. One describes the total energy of the system in the HS state (solid line) while the other does the same for the LS state (dashed line). At the transition point the two curves intersect and the two states are degenerate. The nature of a DFT calculation is to minimize the total energy and therefore the path of the parabola with the lower energy is followed, if the lattice constant is increased or decreased.

In conclusion it can be stated that the results obtained with KKR`nano` coincide with those of Rößler. A HS/LS-state transition is predicted with both LDA and PBEsol, where PBEsol correctly finds the ground state to be the HS state while LDA does not. In combination with the fact that PBEsol also gives a more realistic estimate of the equilibrium lattice constant, it can be stated that PBEsol is to be preferred over LDA for B20-MnGe.

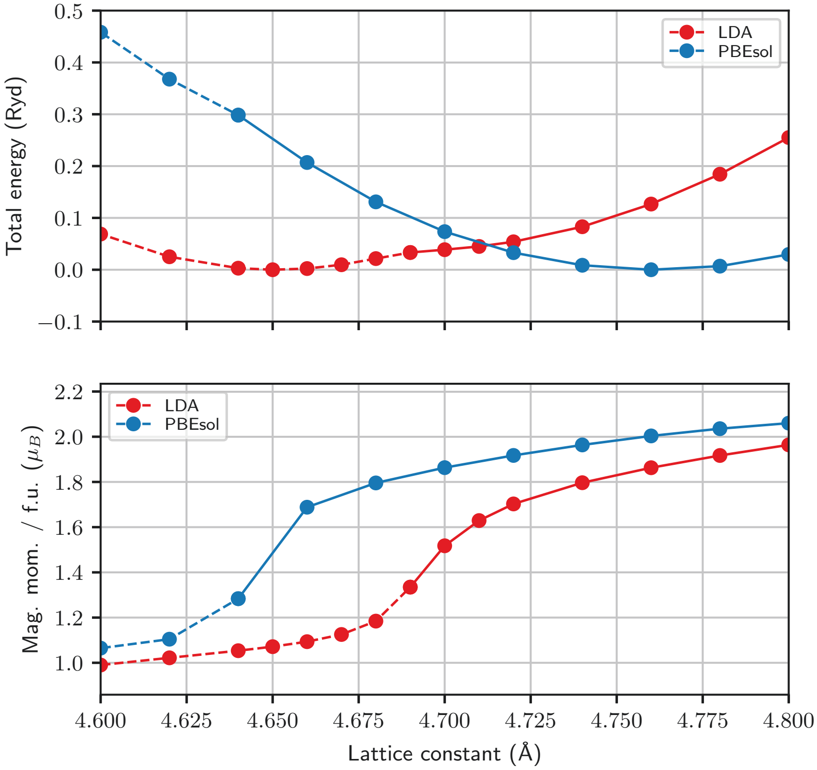

Figure 7.4.: Top: Total energy vs. lattice parameter with LDA and PBEsol functional. For LDA the equilibrium lattice constant is found at 4.65 Å, while PBEsol predicts it to be at 4.76 Å. The respective minimum energy is taken as reference for the energy scale. Bottom: Magnetic moment vs. lattice parameter. If pressure is applied, both LDA and PBEsol predict a transition from a high-spin state (solid line on the right-hand side of the figure) in which the magnetic moment is around 2 $\mu_B/f.u.$ to a low-spin state (dashed line on the left-hand side of the figure), where the moment is about 1 $\mu_B/f.u.$. While LDA estimates the crossover region to be around 4.7 Å, PBEsol expects it to be at approximately 4.65 Å.

7.1.2. Magnetocrystalline Anisotropy

Many materials, e.g. $IrMn_3$, which is discussed in section 5.2.4, show a strong Magnetocrystalline Anisotropy (MA), i.e. there are directions of the magnetic moments with respect to the crystal axes that are energetically preferred. These directions are referred to as the *easy* axes while the least preferable directions are named the *hard* axes. The most common reason given for such rotational symmetry breaking is spin-orbit coupling.

Surprisingly, and in contradiction to previous assumptions, Chacon et al. [124] stated in a recent publication that cubic MA can be a stabilization mechanism in the formation of skyrmions and helices. The influence of (uniaxial) MA on the magnetic structure of B20-MnGe thin films was studied by Kanazawa et al. [125]. The cubic MA was already theoretically considered by Grigoriev et al. [126], who found that it can also have an impact on the stability of helical states in cubic B20-MnGe. These findings ask for a thorough analysis of the MA in B20-MnGe, which is conducted in the following.

In the single-ion picture of MA, there are two main well-known mechanisms. The anisotropy in 4f ions is caused by electrostatic effects that deform the charge cloud, which is rigidly coupled to the spin due to the strong spin-orbit interaction within the 4f electronic shell. In contrast, for 3d magnets, spin-orbit coupling is a small correction to the electronic Hamiltonian and perturbation theory can be used to obtain its impact on the electronic structure, and so compute the magnetocrystalline anisotropy energy (MCE), among other quantities. However, in heavy transition metals both mechanisms can be of importance, establishing an intermediate picture [127].

Computationally, the MCE can be extracted in two ways: The first way is to force the magnetization to point in a certain direction and achieve self-consistency. This scheme has been applied successfully to 3d magnets in the past [128]. The challenging aspect of this type of calculation is to achieve sufficient precision in the computed total energies. For a KKR calculation, we prescribe the orientation of the exchange-correlation magnetic field to the desired direction and iterate until the potential and with it the total energy are self-consistently determined. In this case, the resulting total energy E_{total} is the quantity that needs to be analyzed. The calculations are performed for every magnetization direction that shall be investigated, e.g. for a set of directions that lay in a certain symmetry plane. The other way is to utilize the magnetic force theorem, as it is done in [129]. This theorem justifies replacing the difference of self-consistent total energies with the difference of non-self-consistent band energies E_{band}, which are easier to obtain with the required numerical precision. According to Wang et al. [130], the validity of such an approach in cubic materials is questionable – an aspect that must be kept in mind when analyzing the results. For a KKR calculation, a single calculation is converged with the magnetization pointing along a specific direction (for instance, the z-axis). Then, a single KKR iteration is performed with the exchange-correlation magnetic field pointing in each direction that is of interest, starting from the potential obtained in the self-consistent calculation.

We first investigate the MA in bulk B20-MnGe by means of the total energy obtained from a series of self-consistent KKR`nano` calculations. The direction of all Mn moments is continuously rotated within the z-x plane from the positive z-direction to the negative z-direction. Additionally, another set of calculations is performed in the x-y plane, where the moments are rotated from the positive x-direction to the negative x-direction. Both rotations are equivalent in a cubic system and comparing both of them in a single plot is a good consistency check. The resulting total energies over the sweeping angle

α are depicted in Figure 7.5, where a rotation by 180° is performed in both planes. The value for $\alpha = 0°$ is taken as the base value. The ideal curve that models the cubic

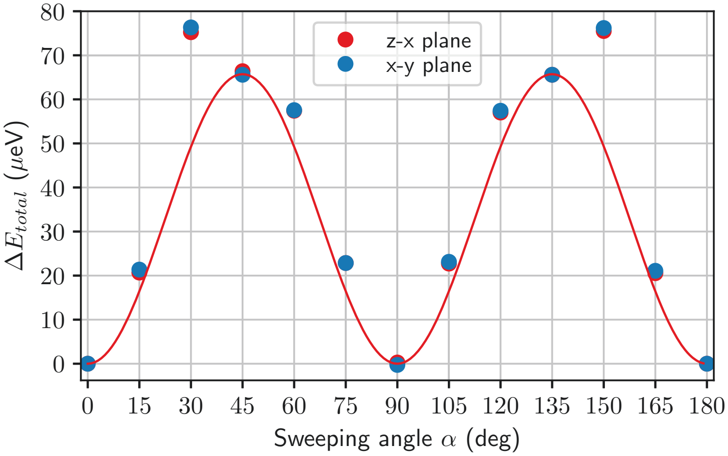

Figure 7.5.: Magnetocrystalline anisotropy energy of B20-MnGe obtained by means of the total energy. The total energy is calculated for different sweeping angles α, i.e. the direction of all Mn moments is rotated within a plane, and the value for $\alpha = 0°$ serves as base line. This rotation is performed in the z-x plane and the x-y plane. The red curve is the form expected from eq. (7.3).

MCE has the form [127]

$$\Delta E_{\text{total}} = E_{\text{total}}(\hat{n}) - E_{\text{total}}(\hat{z}) = K\left(n_x^2 n_y^2 + n_y^2 n_z^2 + n_x^2 n_z^2\right) . \qquad (7.3)$$

Here, $\hat{n} = (n_x, n_y, n_z)$ is the unit vector describing the orientation of the magnetic moment, and K is the MCE constant, which can be positive or negative. This means that the possible easy axes are either the cubic axes or the diagonals of the cube. The red curve in the figure is fitted following these assumptions. The obtained data is symmetric around $\alpha = 90°$ and we can therefore restrict the angular range in further investigations to values below $\alpha = 90°$. Total energy mimima are found for $\alpha = 0°$ and $\alpha = 90°$, respectively, i.e with moments pointing in positive or negative z-direction. The energy is supposed to peak when the moments are aligned along the crystallographic x-direction with $\alpha = 45°$. Interestingly, this is not the case, neither for a rotation in the z-x plane nor in the x-y plane. Instead, with the available data the peak is found for $\alpha = 30°$. The origin of this non-trivial behavior of the MA is currently being investigated. Figure 7.6 proves that this is not something that is related to convergence with k-points. Even a calculation with a very dense mesh of 64 × 64 × 64 k-points yields the peculiarity mentioned above.

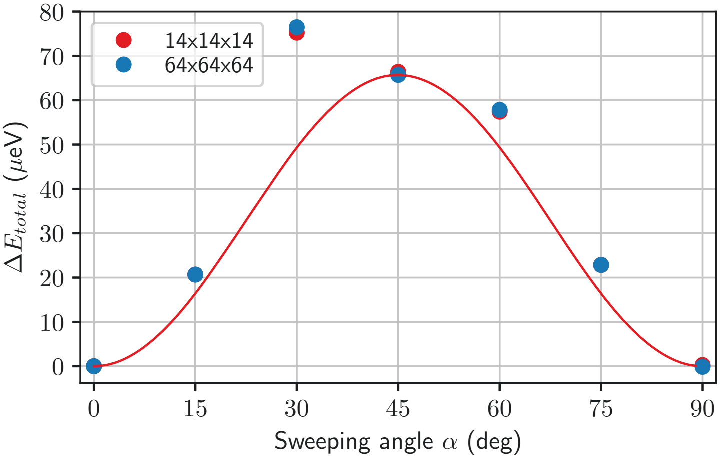

Figure 7.6.: Magnetocrystalline anisotropy energy of B20-MnGe calculated with different k-point meshes. The total energy is calculated for a sweep in the z-x plane with both a k-point mesh of $14 \times 14 \times 14$ and $64 \times 64 \times 64$ to investigate the convergence with respect to k-points. The red curve is the form expected from eq. (7.3). The differences in the total energy between both meshes are insignificant.

The second possibility to quantify the MCE in a system is to utilize the magnetic force theorem and compare the sum of band energies for a series of one-shot calculations in which the magnetic moments are made to point in different directions. Such calculations might help to identify the origin of the peculiar angular dependence of the MA found with the total energy calculations. For B20-MnGe this procedure yields the results depicted in Figure 7.7. In addition to the one-shot calculation, we also provide data from a related set of calculations, where the Fermi level is adjusted to guarantee charge neutrality. This is done by performing multiple iterations instead of just a single one while prohibiting the potential from changing. Both data sets obviously do not fulfill the symmetry conditions of a cubic anisotropy, i.e. a symmetric curve around $\alpha = 45°$. One possible explanation is that SOC lowers the symmetry from cubic to tetragonal in the self-consistent calculation with the magnetic moment pointing in the z-direction. This is then built into the spatial shape of the self-consistent potential. For the one-shot calculations, the rotation of the magnetic direction does not take into account that the deformation of the shape of the potential should be tied to the magnetic direction, which might lead to the lower symmetry found in these results. Furthermore, the energy scale is of the order of less than a μeV which raises concerns on the meaningfulness of these energy differences. Therefore, from a numerical point of view we conclude that the converged total energy is the more meaningful quantity with regards to the investigation of the MCE in B20-MnGe.

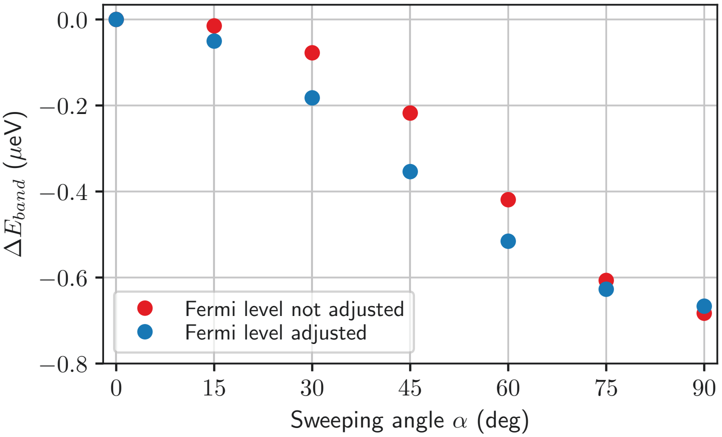

Figure 7.7.: Magnetocrystalline anisotropy energy in B20-MnGe by means of the sum of band energies. The sum of band energies is calculated for a sweep in the z-x plane. The Fermi level is either left as it is after a single iteration (red points) or adjusted to guarantee charge neutrality in the system (blue points), always while leaving the potential unchanged. The resulting patterns do not comply with what is observed for the total energies in Figure 7.6.

A possible explanation for the different outcome of both methods is that the mechanism that gives rise to MA in B20-MnGe is rather of the 4f-type than of the 3d-type, although Mn is a 3d element and Ge is not particularly heavy. This would mean that the anisotropy effect is not directly linked to spin-orbit coupling, which is the energy contribution captured in the one-shot calculations, but is the result of a change of the electrostatic crystal field, where the charge cloud surrounding the nucleus is deformed depending on the orientation of the magnetic moments, which happens indirectly through the spin-orbit coupling. Such a phenomenon is not captured by a one-shot calculation and therefore the investigation of converged total energies is required.

In general, it must be stressed that the energy differences are in the μeV range and therefore fairly small, even for magnetic effects which usually occur on the meV scale. Therefore, it can be concluded that there is a small magnetic anisotropy but that it does not play a decisive role in bulk B20-MnGe. It is therefore well justified to neglect the effect of the magnetocrystalline anisotropy in the following.

Further investigation, after the first edition of this thesis was handed in, showed that the magnetic anisotropy results depend strongly on the density of the radial mesh points that are used in the scalar-relativistic non-collinear single-site solver (see section 5.2). This issue is still under investigation but it underlines that when energy differences in the μeV range are compared, possible numerical issues should be taken into consideration.

7.2. Magnetic Model for MnGe

In this section, an attempt to investigate B20-MnGe with help of the atomistic spin model and the micromagnetic model is made. It is explained how the atomistic quantities can be transformed into micromagnetic quantities and the Curie temperature is calculated from the extracted parameters. The deviation to the experimentally determined Curie temperature can be considered as a *quality measure* of our parameters. Finally, atomistic spin dynamics (ASD) simulations are performed based on the atomistic parameters that we obtained.

7.2.1. Micromagnetic Parameters

The atomistic model parameters, which appear in the Heisenberg model in chapter 6, can be connected to the micromagnetic model, that has the form of a continuum theory. The latter is widely used in the skyrmion community and we adopt it to complement our toolbox for the investigation of the magnetic properties of the B20 materials.
We exemplify the connection between the two models with a helical spin spiral that points along the z-axis (c.f. 1Q state in eq. (7.2)) and is described by the wave vector $\vec{q} = \Big(0, 0, q\Big)$, i.e. the magnetic moments rotate within the x-y-plane and the wave vector points along the z-axis. The magnetization of each atom i is then given by

$$\vec{m}_i = \cos{(qz_i)}\hat{e}_x - \sin{(qz_i)}\hat{e}_y, \tag{7.4}$$

where z_i denotes the z-coordinate of the respective atom. In the following we show how such a magnetic structure interpolates smoothly between the discrete lattice and the continuum limit. We define the Heisenberg energy with isotropic exchange interaction and DMI interaction as

$$E_{\text{atom}} = -\sum_{ij} J_{ij}\vec{m}_i\vec{m}_j + \sum_{ij} \vec{D}_{ij} \cdot (\vec{m}_i \times \vec{m}_j) \tag{7.5}$$

using the same convention as in the juKKR code, which we will use in the following to extract the model parameters from DFT. Insertion of eq. (7.4) and usage of addition theorems leads to

$$\begin{aligned}E_{\text{atom,1Q}} =& -\sum_{ij} J_{ij} \cos\left(q(z_i - z_j)\right) \\ &+ \sum_{ij} \vec{D}_{ij} \cdot \hat{e}_z \left(\sin\left(qz_i\right)\cos\left(qz_j\right) - \cos\left(qz_i\right)\sin\left(qz_j\right)\right) \\ =& -\sum_{ij} J_{ij} \cos\left(q(z_i - z_j)\right) + \sum_{ij} D^z_{ij} \sin\left(q(z_i - z_j)\right) \\ =& N\left(-J(q) + D^z(q)\right), \end{aligned} \tag{7.6}$$

where we used the translational invariance of J_{ij} and N is the number of atoms. For the helical spiral defined in eq. (7.4), only the z-component D^z_{ij} of $\vec{D}_{ij}$ needs to be considered.

The micromagnetic energy [113] reads

$$E_{\text{micro}} = \int dV\, \frac{A}{2}\left((\nabla m_x)^2 + (\nabla m_y)^2 + (\nabla m_z)^2\right) + D\vec{m} \cdot (\nabla \times \vec{m}), \tag{7.7}$$

where A is the so-called *spin stiffness* and D the *DM spiralization*. Insertion of the magnetization of the helical spiral given by eq. (7.4) yields

$$\begin{aligned}E_{\text{micro},1Q} =& \int dV\, \frac{A}{2} q^2 \left(\sin^2\left(qz\right) + \cos^2\left(qz\right)\right) \\ &+ D\left(\cos\left(qz\right)\hat{e}_x - \sin\left(qz\right)\hat{e}_y\right) \cdot \left(\frac{\partial}{\partial z}\sin\left(qz\right)\hat{e}_x + \frac{\partial}{\partial z}\cos\left(qz\right)\hat{e}_y\right) \qquad (7.8) \\ =& \int dV\, \frac{A}{2} q^2 + Dq\left(\cos^2\left(qz\right) + \sin^2\left(qz\right)\right) \\ =& \int dV\, \frac{A}{2} q^2 + Dq \\ =& NV_\Omega\left(\frac{A}{2}q^2 + Dq\right), \end{aligned} \tag{7.9}$$

where V_Ω is the volume of the considered unit cell. The wave number q will take the value which minimizes $E_{\text{micro},1Q}$ and we can thus impose the condition

$$\frac{\partial E_{\text{micro},1Q}}{\partial q} \overset{!}{=} 0 \tag{7.10}$$

$$\Leftrightarrow \frac{\partial}{\partial q}\left(V_\Omega\left(\frac{A}{2}q^2 + Dq\right)\right) = 0 \tag{7.11}$$

$$\Leftrightarrow Aq + D = 0 \tag{7.12}$$

$$\Leftrightarrow q = -\frac{D}{A}, \tag{7.13}$$

which gives us a provision on how the wave number q depends on the magnitude of DM spiralization and spin stiffness.

The atomistic and the micromagnetic model are connected in the limit $q \to 0$, i.e.

for a helical spiral that extends over multiple unit cells. Equation (7.6) can then be simplified to

$$\begin{aligned} E_{\mathrm{atom,1Q}} &= -\sum_{ij} J_{ij} \cos\left(q(z_i - z_j)\right) + \sum_{ij} D^z_{ij} \sin\left(q(z_i - z_j)\right) \\ &= -\sum_{ij} J_{ij} \left(1 - \frac{1}{2}\left(q(z_i - z_j)\right)^2\right) + \sum_{ij} D^z_{ij} q(z_i - z_j) + \mathcal{O}(q^3) \\ &= \underbrace{-\sum_{ij} J_{ij}}_{E_0} + \underbrace{\frac{1}{2}\sum_{ij} J_{ij}\left(z_i - z_j\right)^2}_{A} q^2 + \underbrace{\sum_{ij} D^z_{ij}\left(z_i - z_j\right)}_{D} q + \mathcal{O}(q^3). \end{aligned} \tag{7.14}$$

Thus in this limit, it is possible to derive the micromagnetic parameters A and D from the atomistic parameters J_{ij} and $\vec{D}_{ij}$ which can be obtained from a KKR calculation by following the procedure described in section 6.3. The term E_0 determines the ferromagnetic reference energy. The exchange stiffness A describes the increase in energy if a spin spiral is assumed instead of the ferromagnet. The micromagnetic DMI D can lower the energy if the product of D and q is negative and can thus make the spin spiral configuration the energetically preferred state.

In general, A and D are 3×3 tensors that we denote with $\mathcal{A}$ and $\mathcal{D}$. For B20 compounds this simplifies to diagonal matrices due to symmetry arguments and we obtain

$$\begin{aligned} \mathcal{A} &= \sum_{ij} J_{ij} \begin{pmatrix} \vec{R}_{ij} \cdot \vec{R}_{ij} & 0 & 0 \\ 0 & \vec{R}_{ij} \cdot \vec{R}_{ij} & 0 \\ 0 & 0 & \vec{R}_{ij} \cdot \vec{R}_{ij} \end{pmatrix} \\ &= \sum_{ij} J_{ij} \left|\vec{R}_{ij}\right|^2 \underline{\underline{I_3}} = A \underline{\underline{I_3}} \end{aligned} \tag{7.15}$$

and

$$\begin{aligned} \mathcal{D} &= \sum_{ij} \begin{pmatrix} \vec{R}_{ij} \cdot \vec{D}_{ij} & 0 & 0 \\ 0 & \vec{R}_{ij} \cdot \vec{D}_{ij} & 0 \\ 0 & 0 & \vec{R}_{ij} \cdot \vec{D}_{ij} \end{pmatrix} \\ &= \sum_{ij} \left(\vec{R}_{ij} \cdot \vec{D}_{ij}\right) \underline{\underline{I_3}} = D \underline{\underline{I_3}}. \end{aligned} \tag{7.16}$$

It should be noted that from eq. (7.16) it follows that D vanishes for $\vec{D}_n \perp \vec{R}^n$ and is largest for $\vec{D}_n \parallel \vec{R}^n$.

Extraction of Parameters

We use the juKKR code to extract the isotropic exchange interactions (J_{ij}) and the Dzyaloshinskii-Moriya interactions ($\vec{D}_{ij}$) between the four Mn atoms in B20-MnGe. To this aim the formalism explained in section 6.3 is utilized.

The calculations are performed for $a = 4.76$ Å, the theoretical equilibrium lattice constant using PBEsol, with a broadening temperature of $T = 800$ K and the interaction parameters are extracted using a $60 \times 60 \times 60$ k-point mesh. In order to investigate the impact of a shift of positions, the interaction parameters are determined for the experimentally obtained positions of the Mn atoms with $u = 0.135$ and a slightly smaller (larger) value of $u = 0.125$ ($u = 0.145$). When the Mn atoms are moved, the distance between Mn and Ge atoms in the crystal structure changes. This potentially gives rise to increased hybridization between both atom types which might be the reason for the changes of the DM interaction. The Ge atoms are non-magnetic and therefore the calculations yield only a small induced magnetic moment of $0.1\mu_B/f.u.$ so that their explicit contribution can be neglected in our magnetic model analysis.

An inhouse code that only considers the isotropic exchange interactions J_{ij} to determine the Curie temperature of the system [131] is used. Sergii Grytsiuk performed these simulations with the interactions that the author of this thesis calculated with the juKKR code. The resulting Curie temperature T_C (see Figure 7.8) depends on the number of shells that are included in the simulation. In contrast to the micromagnetic quantities A and D (see below), the Curie temperature T_C is more or less converged, when interactions up to $2a$ are taken into account. The consideration of J_{ij} parameters where the distance between site i and j lies above this value does not significantly change T_C. However, this converged value of $T_\mathrm{C} \approx 300$ K lies considerably above the

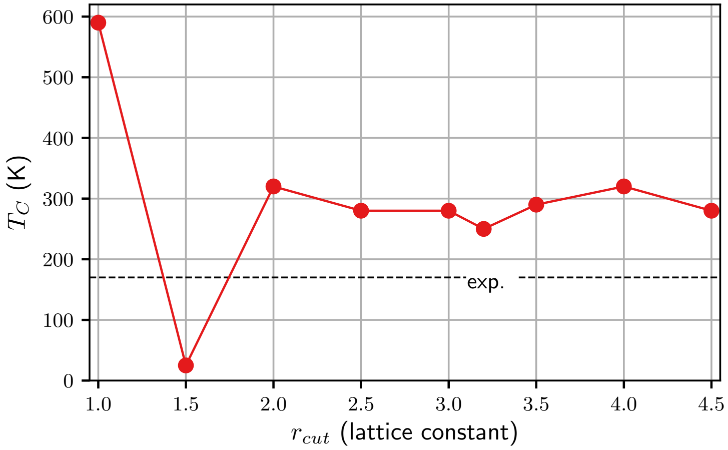

Figure 7.8.: Curie temperature T_C obtained with a Monte Carlo method by usage of the isotropic exchange interactions J_{ij} from Figure 7.9 for $u = 0.135$. The consideration of interactions above a cut-off distance of $r_{cut} = 2.0$ does not significantly change the resulting T_C. The Monte Carlo simulation was performed by Sergii Grytsiuk.

experimental value $T_{\mathrm{C}}^{\mathrm{exp.}} \approx 170$ K [25].
The capability to correctly predict the Curie temperature can be considered as a quality measure of the extracted isotropic interaction coefficients. In our calculations we see a discrepancy of more than 100 K which is unsatisfactory.

The results of our detailed analysis of the magnetic coupling coefficients can be found in Figure 7.9, where both the atomistic model parameters J_{ij} and $|\vec{D}_{ij}|$ as well as the derived micromagnetic quantities A and D are depicted. For all three u-parameters the first nearest-neighbor interaction is strongly positive which means that ferromagnetic coupling is preferred here. However, the alternating sign of the second nearest-neighbour isotropic exchange interactions indicates magnetic frustration.
The absolute values of $\vec{D}_{ij}$ are two orders of magnitude smaller than the values of J_{ij}. Interestingly, a different choice of the structural parameter u has a strong influence on their behavior between the second and fifth shell.
Neither spin stiffness A nor DM spiralization D converge to a constant value, when shells up to $3a$ are taken into account, where a is the lattice parameter. It is therefore not possible to estimate the helical pitch by the relation of spin-stiffness and micromagnetic DM interaction that is given in eq. (7.10). Note, that estimating the pitch in this manner is only valid, if the magnetic texture is created by the competition of spin-stiffness and DM interaction in the micromagnetic model. If frustration plays a crucial role, as described in [132], eq. (7.10) is no longer applicable. While the absolute values of $\vec{D}_{ij}$ are very similar for the first shell, the values of D differ if only the first shell is taken into account. This can be attributed to the scalar product in eq. (7.16) which makes D dependent not only on the absolute value of $\vec{D}_{ij}$ but also on its direction with respect to the corresponding atomic bond vectors. Conclusively, it can be observed that a change of the u-parameter results in a global shift of D. Its value can be increased by decreasing u.
Note that the different values of the atomistic parameters for the same spatial distance are possibly caused by numerical inaccuracies in the calculation of the infinitesimal rotations in connection with the PBEsol functional. This issue is not present, when LDA is used.

Another structural parameter whose effect on the magnetic model parameters can be studied is the lattice constant. Our results of this analysis are shown in Figure 7.10. We performed calculations for $a = 4.85, 4.90, 5.00$ and 5.10 Å. All of these lie above the equilibrium lattice constant. Our interest in this regime was triggered by the results of KKR`nano` calculations presented in section 7.3.1, where non-trivial magnetic states are favoured, when a larger lattice constant is assumed.
By increasing a, and therefore the inter-atomic distances, the first nearest-neighbor isotropic exchange can be reduced. The J_{ij}-couplings between the neighbours that lay further apart are less affected.
The behaviour of the absolute values of $\vec{D}_{ij}$ differs between the two smaller ($a = 4.85, 4.90$ Å) and the two larger ($a = 5.00, 5.10$ Å) lattice constants. For the smaller lattice constants the first nearest-neighbor contribution dominates. Interestingly, the

behaviour changes for the larger lattice constants. Here, the most significant $\vec{D}_{ij}$ values are found for $|\vec{r}_j - \vec{r}_i| = 1.0\ a$.

Similar to the data obtained with varied u-parameter in Figure 7.9, the spin stiffness parameter A cannot be converged for any data set. Nevertheless, it is interesting that A becomes increasingly negative with larger lattice constants. A comparison with eq. (7.14) shows that a negative spin stiffness $A < 0$ would favour a magnetic configuration where $\vec{q} \neq \vec{0}$. This could be a hint to the existence of a helical magnetic texture. Similarly, to the spin stiffness tensor, the micromagnetic DM interaction D does not converge either. However, it is interesting to see that its sign differs between different lattice parameters if we consider only the first shell for a moment. This indicates that there is also a sign change in the components of $\vec{D}_{ij}$.

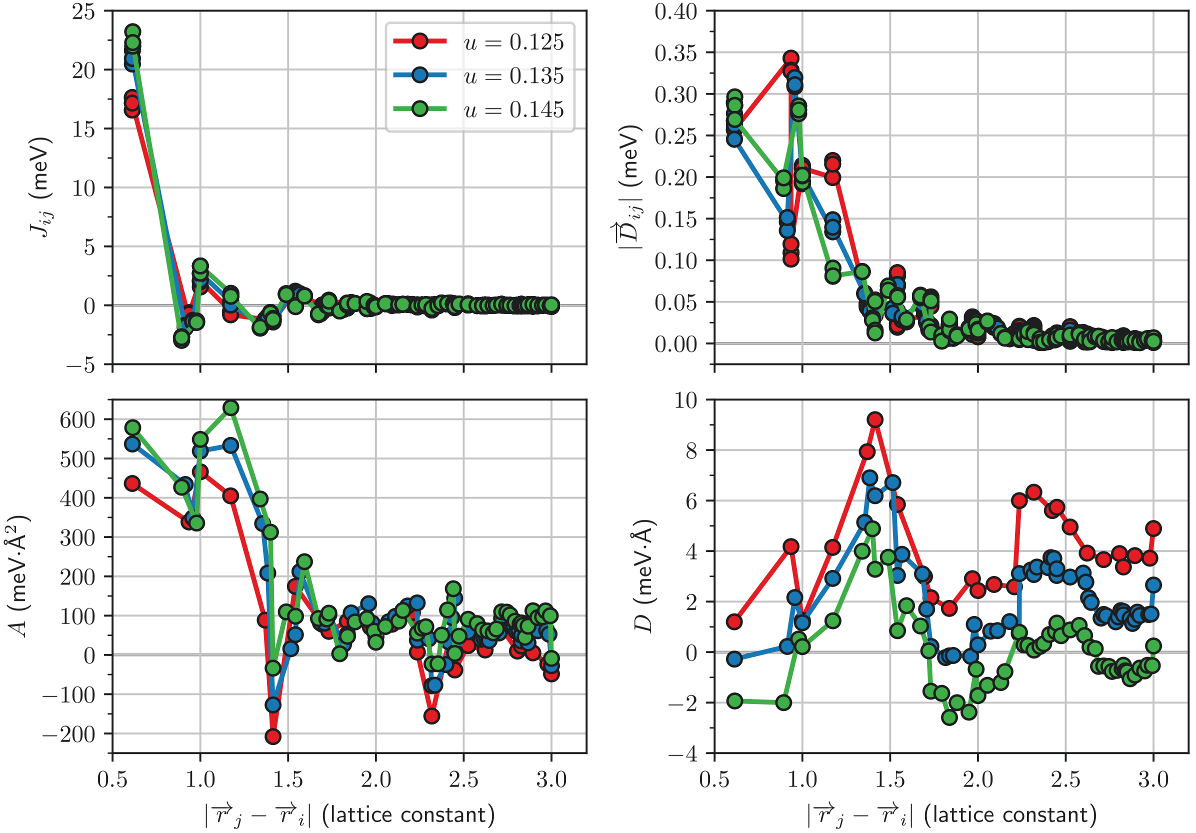

Figure 7.9.: Isotropic magnetic exchange couplings (J_{ij}) and absolute values of the DMI vectors ($\left|\vec{D_{ij}}\right|$) as function of distance between atoms i and j derived from an ab initio calculation with KKR using the PBEsol functional. The colors indicate the chosen structural u-parameter. For the next nearest neighbour the isotropic exchange interaction is considerably larger than the DMI. For more remote atomic pairs the difference in magnitude between the two decreases. The sign of J_{ij} alternates with distance giving rise to magnetic frustration as a positive (negative) value corresponds to (anti-)ferromagnetic coupling between two atoms. The micromagnetic spin-stiffness A and the DMI do not converge to a constant value with the inclusion of more shells.

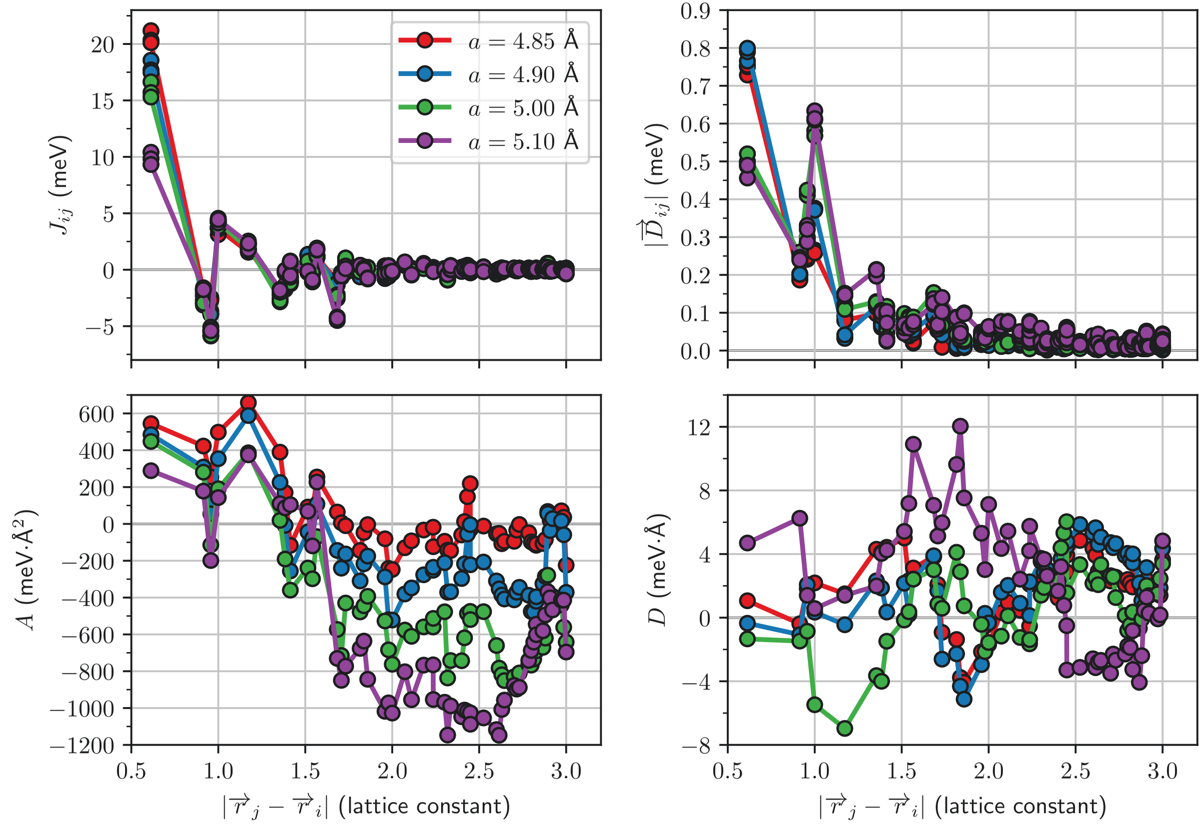

Figure 7.10.: Isotropic magnetic exchange couplings (J_{ij}) and absolute values of the DMI vectors ($\left|\vec{D_{ij}}\right|$) as function of distance between atoms i and j derived from an ab initio calculation with KKR using the PBEsol functional. The colors indicate the chosen lattice parameter. For the next nearest neighbour the isotropic exchange interaction is considerably larger than the DMI. For more remote atomic pairs the difference in magnitude between the two decreases. The sign of J_{ij} alternates with distance giving rise to magnetic frustration as a positive (negative) value corresponds to (anti-)ferromagnetic coupling between two atoms. The micromagnetic spin-stiffness A and the DMI do not converge to a constant value with the inclusion of more shells.

7.2.2. Atomistic Spin Dynamics Results

Another reason for extracting the model parameters J_{ij} and $\vec{D}_{ij}$ is to be able to perform Atomistic Spin Dynamics (ASD) simulations by solving the Landau-Lifshitz-Gilbert (LLG) equation as explained in section 6.1. For that purpose we use the software package SPIRIT [23] which is capable of simulating the dynamics of each spin via the LLG equation and additionally features a real-time visualization of the spin system. The model parameters are obtained from juKKR for $a = 4.795$ with LDA as exchange-correlation functional and interactions up to $r_{\text{cut}} = 2.0a$ are taken into account. This is a configuration for which the following observations can be made, although it should be mentioned that slightly varied lattice constants and u-parameters yield qualitatively similar results in ASD.

For our first setup we initialize a $6 \times 6 \times 1$ supercell grid of B20-MnGe unit cells with open boundary conditions. In ASD we only consider the Mn atoms since the Ge atoms have merely a small induced magnetic moment which we neglect. Furthermore, it should be noted that in layered systems the uniaxial magnetocrystalline anisotropy can be of importance [125] but is neglected for simplicity in our simulations. Several runs from random magnetic starting configurations indicate that the ground state is ferromagnetic which contradicts the findings of recent experimental works [28, 119]. Further, relaxation of several random initial configurations reveals that two non-trivial objects are found to be metastable, i.e. they exist at a higher total energy than the ferromagnet but are confined in a local energy minimum. These two objects are a chiral vortex and an achiral antivortex (see Figure 7.11). In the literature these two objects are also referred to as *skyrmion* and *antiskyrmion*. To further analyse this discovery the energy landscape between the two states is of special interest.

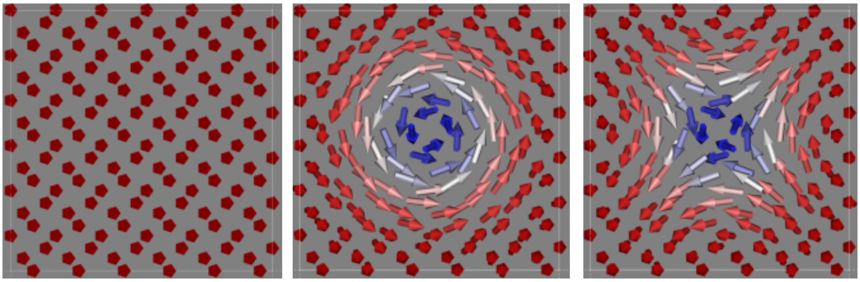
(a) (b) (c)

Figure 7.11.: Magnetic moments of the Mn atoms for three (meta-)stable magnetic states in a grid of $6 \times 6 \times 1$ unit cells of B20-MnGe: a) Ferromagnet, b) Skyrmion with left-handed chirality, c) Achiral antiskyrmion. Positive (negative) z-direction of the spins is coded in red (blue).

The geodesic nudged elastic band (GNEB) method [133] provides a concept to perform

such an analysis. Here, the energetically optimal transition path between two *a priori* defined states is calculated so that an energy landscape can be determined. This allows to identify local energy minima where magnetic textures can exist in a metastable state.
The result of the application of GNEB to our problem is depicted in Figure 7.12. It shows that there is a small local minimum of the spin dynamics energy E_{SD} for the skyrmion and the antiskyrmion at the 10th GNEB frame. Globally, both skyrmion (red) and antiskyrmion (blue) state are approximately 1.8 meV per Mn site higher in energy than the ferromagnetic state. The energy barrier is centered around the 8th GNEB frame of the transition path. Its height can be approximated to be 0.1 meV for both skyrmion and antiskyrmion.

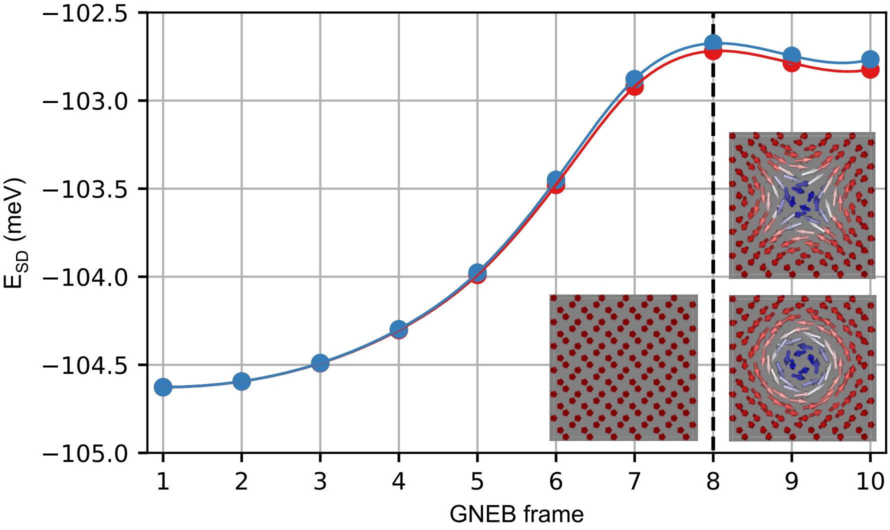

Figure 7.12.: Energy landscape between ferromagnetic (frame 1) and skyrmionic/antiskyrmion (frame 10) state obtained with GNEB. Red (blue) markers denote points in the transition path from the skyrmion (antiskyrmion) state to the ferromagnetic state. The data points are interpolated with a cubic spline. Both skyrmion and antiskyrmion state are approximately 1.8 meV per site higher in energy than the ferromagnetic state. The energy barrier separating both states is given by the energy difference of frame 8 and 10 and has a height of roughly 0.1 meV for both textures.

Another simulation using a 25 × 25 × 1 grid, that is open in z-direction and periodic in x- and y-direction, allows to investigate the impact of the DM interaction on the chirality of the skyrmions. Figure 7.13 shows an example simulation (a), where the coefficients $\vec{D}_{ij}$ are considered and a simulation (b), where they are not included in

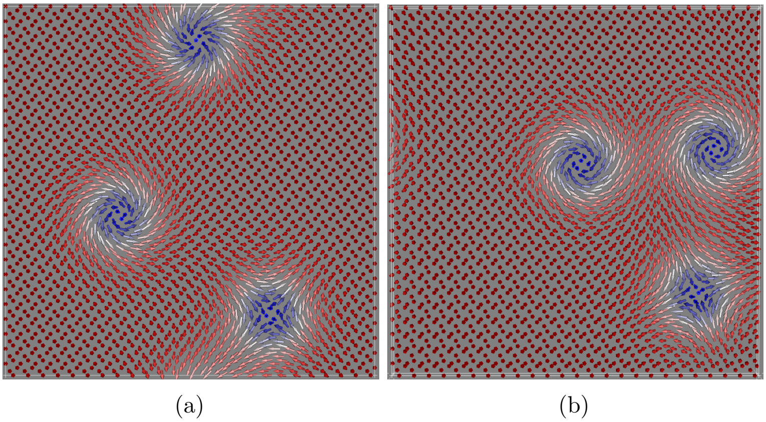
(a) (b)

Figure 7.13.: Result of a spin dynamics simulation on a $25 \times 25 \times 1$ grid of MnGe unit cells with an applied magnetic field $B_z = 2.4$ T, a damping parameter $\alpha = 0.5$ and periodic boundary conditions in all three spatial directions. a) DM interaction is considered in the Hamiltonian: Two skyrmions with left-handed chirality and an antiskyrmion emerge from the random starting configuration. The applied magnetic field ensures a background polarized in positive z-direction. b) DM interaction is neglected: There are two skyrmions with opposite chirality and the antiskyrmion.

the model Hamiltonian. From this it can be deduced that the creation mechanism can be attributed to the frustrated isotropic exchange interactions, while the chirality of the skyrmions is determined by the DM interaction. In the case of B20-MnGe the magnetic chirality corresponds to the crystal chirality [117]. Our SPIRIT calculations confirm this since our unit cell describes left-handed B20-MnGe and the skyrmions that can be observed with included DM interaction are exclusively left-handed.

Finally, we perform an ASD simulation with SPIRIT starting from randomized spin directions on a periodic grid of $25 \times 25 \times 1$ MnGe unit cells (2500 magnetic Mn atoms) with periodic boundary conditions, an applied external B-field in z-direction $\vec{B} = (0, 0, 2.4)$ T and a damping parameter $\alpha = 0.5$. The magnetic field coincides with the maximum field strength at which the 3Q state was observed in B20-MnGe [28]. The large damping parameter of 0.5 fosters a quick relaxation of the system into the ground state. At this point both isotropic and antisymmetric exchange are taken into account. The system is initialized with the magnetic moments pointing in random directions (Figure 7.14a). After some time steps magnetic domains form (Figure 7.14b) During the relaxation process the two familiar non-trivial textures from Figure 7.11 form spontaneously at *a priori* indeterminate positions (see Figure 7.14c). Once formed with sufficiently large spacing between one another they remain stable due to their inherent topological protection. If textures with opposite topological charge, i.e. a skyrmion and an antiskyrmion form in immediate proximity, they annihilate each other. Here, this is the case as eventually one skyrmion and one antiskyrmion remain, approach each other and eventually annihilate. Therefore, it seems like there is an attractive force between skyrmion and antiskyrmion. The process is visualized in Figures 7.14c to 7.14e. Energetically, such an annihilation is preferable over an individual dissolution of each texture as the energy barrier that needs to be overcome is smaller. Without any topologically protected objects, the spins finally align in positive z-direction (Figure 7.14f), which is the preferred axis due to the imposed magnetic field.

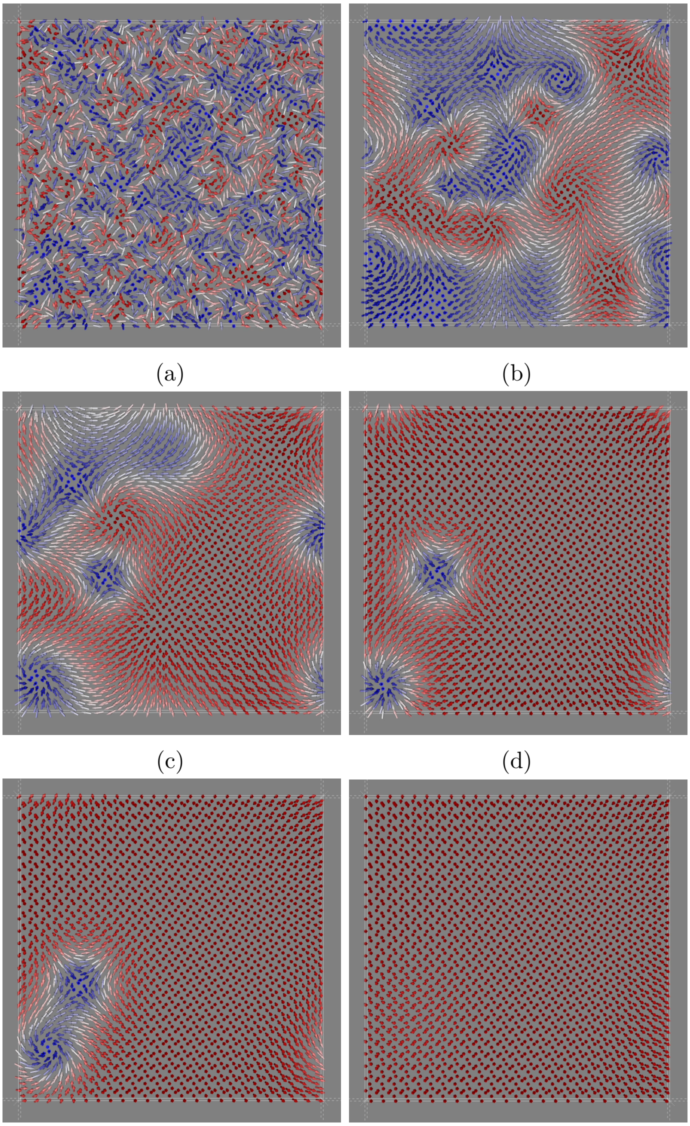

(a) (b)

(c) (d)

(e) (f)

Figure 7.14.: Evolution of the magnetic moments of a periodic 25 × 25 × 1 grid of B20-MnGe unit cells in a SPIRIT simulation. The system is initialized with the moments pointing in random directions. Skyrmions and antiskyrmions form during the relaxation process and then annihilate each other so that the final state is ferromagnetic.

7.3. Large-Scale KKR`nano` Calculations for MnGe

In this section we present the large-scale DFT results that we obtained with KKR`nano` for B20-MnGe. We commence with a comparison of energy profiles of three different non-trivial magnetic states: The helical spiral, the hedgehog lattice and the Bloch point state. In this study, the lattice constant is varied and the total energies corresponding to the three states are tracked. Subsequently, an attempt is made to stabilize the Bloch point state as the ground state by artificially increasing the strength of spin-orbit coupling in a KKR`nano` calculation. Furthermore, a layered system of B20-MnGe is investigated to gather information on the enhancement of the magnetic moment on a B20-MnGe surface.

We conclude this section with an analysis of variations of the crystallographic structure of B20-MnGe. Based on a result from experiment, we allow more structural degrees of freedom by assuming that the material crystallizes according to the properties of the $P2_12_12_1$ space group.

In all following calculations we use supercells built of $6 \times 6 \times 6$ unit cells so that 1728 atoms are treated. Such calculations can *de facto* only be conducted in the context of High Performance Computing (HPC) and are in our case performed on the supercomputers Hazel Hen in Stuttgart and QPACE3 in Jülich.

7.3.1. Helical Spiral (1Q), Hedgehog Lattice (3Q) and Bloch Point (BP) State

The main reason that motivates the usage of KKR`nano` in conjunction with B20-MnGe is that Tanigaki et al. [28] reported on the existence of the 3Q hedgehog lattice state in this material. A detailed explanation of this magnetic state was already given in section 7.1.

Koretsune et al. [29] used a tight-binding model with Wannier functions and found the DM interaction to be larger than 100 meVÅ which is large enough to explain the short pitch of the predicted helical spiral or the hedgehog lattice in B20-MnGe. However, other works [134] report a minor DM interaction of less than 5 meV Å. Our approach with juKKR does not reproduce a large DM interaction, but estimates it to be at most around 10 meV Å(see Figures 7.9 and 7.10). A DFT calculation with KKR`nano` is more sophisticated than the extended Heisenberg model approach in section 7.2 and could therefore give valuable insights that cannot be obtained otherwise. In the following, calculations are presented with which we attempt to fathom the nature of magnetism in B20-MnGe by imposing non-trivial magnetic textures on the system and comparing them to the trivial ferromagnetic state. These non-trivial textures are the helical 1Q spiral, the hedgehog 3Q lattice and the Bloch point. In the context of these studies we monitor the total energy difference between the three magnetic states by varying the lattice constant and artificially changing the strength of spin-orbit coupling in the system.

Energy profiles for varied lattice constant

We begin by setting up a 6 × 6 × 6 B20-MnGe supercell, where we use PBEsol as exchange-correlation functional and include only a single k-point, i.e. the Γ-point. In this initial comparison of ferromagnetic, 1Q and 3Q state using the equilibrium lattice constant $a = 4.80$ Å, the ferromagnet is the one with the lowest total energy. The respective states are imposed on the system by forcing the atomic exchange-correlation B-fields to point into specific directions. As this contradicts experimental observations we take into consideration that in experiment the crystal structure might inadvertently differ from the ideal structure. Such discrepancies can for instance be caused by strain that originates from the manufacturing process of the sample.
Therefore, it is reasonable to check whether the magnetic materials properties change, when the lattice constant is varied. The result of such a variation is reported in the

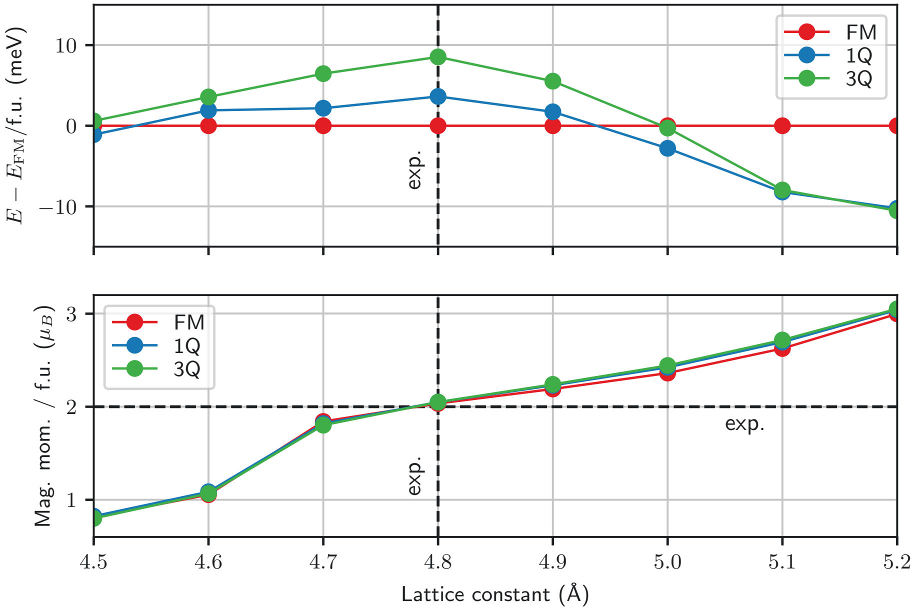

Figure 7.15.: Comparison of Ferromagnetic (FM), helical spiral (1Q) and hedgehog lattice (3Q) state with KKR`nano`. Top: Difference of total energies with respect to the FM state as reference state for different lattice constants. The experimental lattice constant is $a = 4.80$ Å. 1Q and 3Q state are energetically preferable for $a > 5.0$ Å. Bottom: Magnetic moment per Mn atom increases with lattice constant. High-spin/Low-spin transition is clearly visible between $a = 4.60$ and $a = 4.70$ Å. Experimentally, the magnetic moment is measured to be around $2\mu_B$.

upper part of Figure 7.15, where the total energy is evaluated for FM, 1Q and 3Q state. Clearly, neither the 1Q nor the 3Q state constitutes the ground state, when the experimental lattice constant is assumed. Yet, by increasing or decreasing the lattice constant the energetic difference can be made smaller.

We focus on an increase of the lattice constant rather than a decrease since the system goes into the low-spin state below $a = 4.65$ Å and according to experiment the non-trivial textures exist in the high-spin regime. A crucial transition point is found around $a = 5.0$ Å, where by imposing the 1Q or 3Q state the energy can be made smaller than for the ferromagnetic state. In general, for $a > 5.0$ Å both helical states are favored over the ferromagnetic one.

Obviously, an artificial increase of the lattice constant by 0.2 Å ($\approx 4\%$) or more is fairly large. However, probes in experiment are seldom if ever perfectly clean and impurities in the sample need to be considered as a source of error in the final analysis. One potential effect of impurities is chemical pressure that causes a spatial expansion of the lattice structure. An example of the possible effects of positive chemical pressure can be found in Co-doped B20-FeGe [135]. Here, it was experimentally observed that doping can increase the melting temperature and change the magnetic properties of a B20 alloy.

In the lower part of Figure 7.15 the evolution of the magnetic moment with varying lattice constant is tracked. The resulting magnetic moment for the experimental lattice constant nicely falls on top of the magnetic moment of approximately $2\mu_B$/f.u., which is reported by experimentalists [119].

In the lower part of Figure 7.15 the high-spin/low-spin transition is recognizable between $a = 4.60$ and $a = 4.70$ Å.

Furthermore, the magnetic moment increases, when the lattice constant is increased. This is a common behaviour which is often observed in metallic systems. For larger lattice constants the magnetic moments of the three different magnetic textures differ more than for the smaller lattice constants. This might be connected to the observation of the differences in the total energy.

Bloch point with scaled spin-orbit coupling strength

Spin-orbit coupling (SOC) in KKR`nano` is implemented such that its contribution is simply added to the scalar-relativistic potential. This allows to scale its strength by tuning the prefactor so that SOC can artificially be made stronger which enables us to investigate a system's behaviour if this parameter is altered with respect to its proper value.

In this context we perform a comparison of the Bloch point (BP) state and the ferromagnetic (FM) state. The BP texture is defined by means of the four spherical parameters ϕ, θ, Φ and Θ. ϕ and θ designate the position of an **individual atom** in the unit cell which is described by the radius r and the common polar and azimuthal angle

$$\phi = \arctan\left(y/x\right) \tag{7.17}$$

and

$$\theta = \arccos\left(\frac{z}{\sqrt{x^2+y^2+z^2}}\right). \tag{7.18}$$

The BP texture does not depend on r and we can therefore neglect it in the following. Usually, the atomic positions are given in the Cartesian coordinates x, y and z. In the definition above, we define the origin of the coordinate system, i.e. the tuple ($x = 0$, $y = 0$, $z = 0$), to be at the center of the unit cell. In this frame of reference all atoms that lay in an x-y-plane that intersects with the center are described by $\theta = \pi/2$. The orientation of the **individual atomic magnetic moments** for a BP texture is then defined by the polar angle

$$\Phi = \phi + \phi_1 \tag{7.19}$$

and the azimuthal angle

$$\Theta = 2\arctan\left(\cot\frac{\theta}{2}\right), \tag{7.20}$$

where the angles designating the atomic position enter as arguments. ϕ_1 is a phase factor. An illustration of a BP is given in Figure 7.16. Note, that in contrast to that illustration we conduct our investigation for a BP with $\phi_1 = \pi$, where magnetic moments are inverted, i.e. all moments point into instead of out of the center.

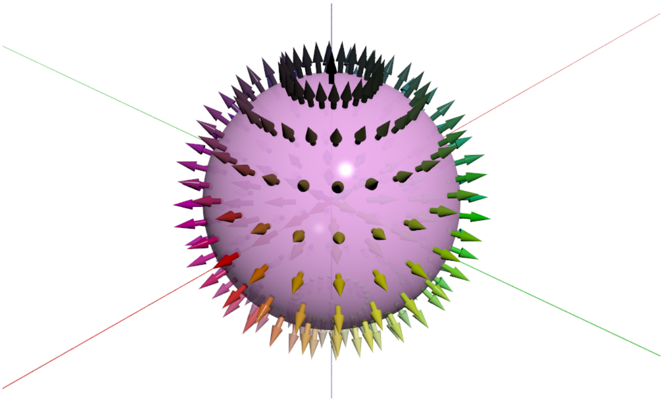

Figure 7.16.: Illustration of a Bloch point in real space with all magnetic moments pointing out of the center of the Bloch sphere. We use the same magnetic configuration but invert the spin direction so that all moments point into the center. Figure provided by Nikolai Kiselev.

For our calculations we again use a $6 \times 6 \times 6$ supercell but this time with a $2 \times 2 \times 2$ k-point-mesh and LDA as exchange-correlation functional. Here, LDA is used because it has been used extensively in all KKR codes in the past and we want to eliminate the possibility of numerical problems that could occur when SOC is artificially enhanced. The magnetic moments are allowed to relax during the convergence process. This leads to a small canting of the moments which is a known effect in B20 materials [136]. A

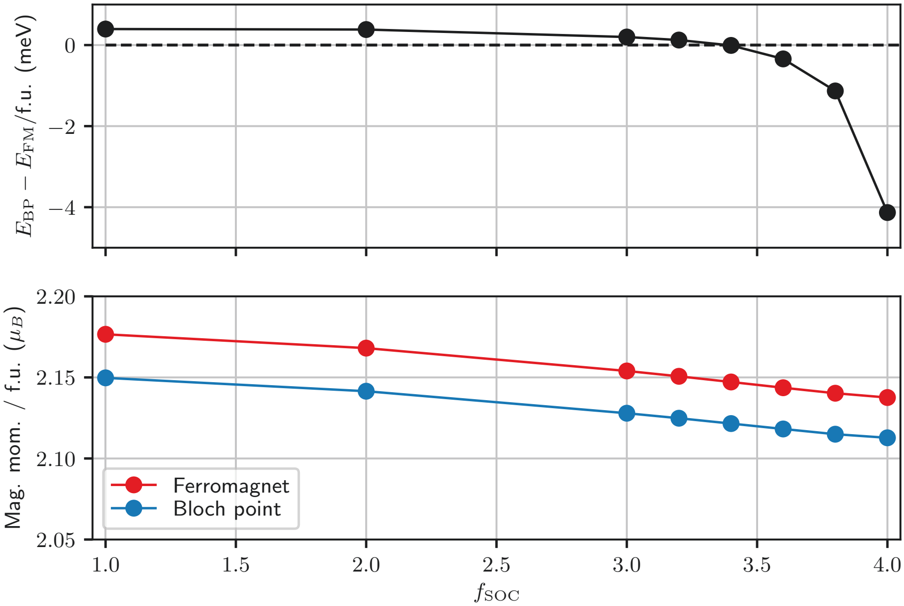

Figure 7.17.: Effect of increased SOC on B20-MnGe in a $6 \times 6 \times 6$ supercell. Top: Total energy difference between (relaxed) Bloch point and (relaxed) ferromagnet. Bottom: Magnetic moment of ferromagnet and Bloch point.

series of calculations is conducted ranging from the physical value of the SOC to an enhancement of it by a factor of $f_{\mathrm{SOC}} = 4.0$ (see Figure 7.17). As could be expected from the investigation of 1Q and 3Q state before, the BP state is energetically not preferred over the FM state for a small scaling of SOC. However, when SOC is scaled further up to $f_{\mathrm{SOC}} = 3.5$, both states are energetically more or less equivalent. Above $f_{\mathrm{SOC}} = 3.5$ the BP state is clearly preferred over the FM state with an energy difference of up to 4 meV/f.u. Within the parameter range that we checked in this study, the most beneficial scaling value for the BP is found to be $f_{\mathrm{SOC}} = 4.0$. The effect of SOC scaling on the magnetic moment can be deemed negligible. Over the whole range it decreases by 0.07 μ_B for each of the two states (see again Figure 7.17). It would be interesting to check whether a global minimum of $E_{\mathrm{BP}} - E_{\mathrm{FM}}$ can be found for $f_{\mathrm{SOC}} > 4.0$. This would hint to an optimal scaling at which also other non-collinear magnetic textures, e.g. 1Q spin spiral or 3Q hedgehog lattice, can possibly be stabilized. However, this is not possible as our method becomes increasingly numerically unstable for such strong scaling factors, i.e. the total energy does not converge anymore. The reason for this is currently under investigation.

7.3.2. Layers

Recently, Kanazawa et al. [125] reported on their research of skyrmions in thin films of B20-MnGe. They found that the 3Q hedgehog-antihedgehog lattice changes depending on the epitaxial-film thickness and attribute this to a change in the magnetic anisotropy. KKR`nano` was not designed for the treatment of thin films as its superior efficiency over other codes is most pronounced for 3D systems. Still, we can simulate a surface by using the familiar $6 \times 6 \times 6$ supercell from before and replacing one layer of MnGe unit cells with vacuum cells. We use a $2 \times 2 \times 2$ k-point-mesh and the PBEsol functional and only consider the collinear ferromagnetic state for this analysis. The magnetic moment is tracked for each layer of Mn atoms so that a layer-resolved impression of the variability of the moments with increasing sample depth is obtained (see Figure 7.18). In the figure the well-known effect of magnetic moment enhancement at a surface can be recognized. This effect can be understood by considering a single Mn atom that is not confined in a solid. The magnetic moment of it is approximately given by

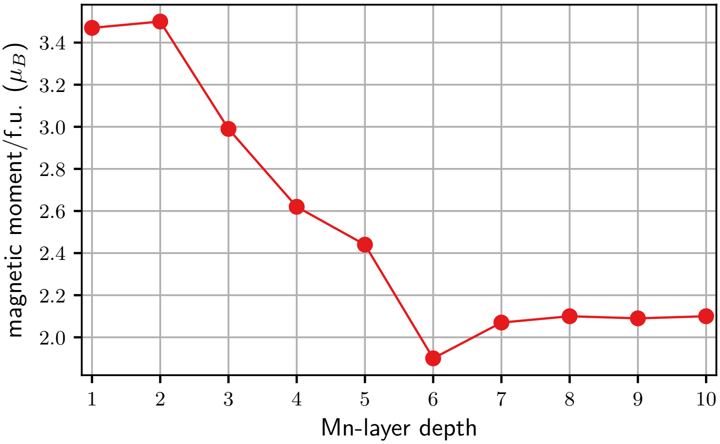

Figure 7.18.: Dependence of the magnetic moment of the Mn atoms on the distance to the artificially constructed surface of B20-MnGe. A Mn-layer depth of 1 designates the first layer of Mn that is adjacent to the vacuum region.

$$\mu_{eff} \approx n\mu_B, \tag{7.21}$$

where n is the number of unpaired electrons and orbital contributions are neglected. A single Mn ion has five unpaired electrons in the 3d-shell and hence $\mu_{eff} \approx 5\ \mu_B$. This is considerably larger than it is in bulk B20-MnGe, where it is found to be $\mu_{\mathrm{Mn},eff} \approx 2\ \mu_B$. This difference can be explained by the competition of kinetic and exchange energy. In the bulk, electrons delocalize and form bands which means that it costs more energy to populate states of the same spin projection. Hence, the magnetic moment is reduced. In the first Mn layer in Figure 7.18 the atoms are exposed to vacuum on one side so that they can be considered half-free in this context. Hence, their magnetic moment is increased to roughly 3.4 μ_B per Mn atom. This surface effect propagates through 6 layers, i.e. one and a half reduced unit cells. Below this depth, the familiar magnetic moment in bulk B20-MnGe is restored which is approximately 2.1 μ_B. Note, that the total number of Mn layers in the system is 20 but that the pattern is symmetric so that there is no need to include more than 10 layers in the plot.

We can conclude from this study that the magnetic characteristics of B20-MnGe are indeed changed, if a thin film is considered. According to our results in section 7.3.1 and particularly in Figure 7.15 the enhancement of the magnetic moment close to the surface could facilitate the existence of non-trivial magnetic textures. There, we observed that an increase of the lattice parameter coincides with an increase of the magnetic moment and that this combined increase promotes the formation of the 1Q and 3Q helical state.

7.3.3. $P2_13$ vs. $P2_12_12_1$ Space Group

In most scientific publications as well as in the established literature B20-MnGe is described within the parameter range of the $P2_13$ space group.

In 2012 Makarova *et al.* found out by means of neutron diffraction studies that around a temperature of 50 K and below B20-MnGe is best described by the more general $P2_12_12_1$ space group [120]. Here, the parameters u_{Mn} and u_{Ge} (see introduction to Chapter 7) are replaced by parameters x_{Mn}, y_{Mn} and z_{Mn} which determine the position of the individual atoms within the unit cell according to

$$\begin{aligned}
\vec{r}_{\text{Mn},1} &= (x_{\text{Mn}}, y_{\text{Mn}}, z_{\text{Mn}}) \\
\vec{r}_{\text{Mn},2} &= (0.5 - x_{\text{Mn}}, 1.0 - y_{\text{Mn}}, 0.5 + z_{\text{Mn}}) \\
\vec{r}_{\text{Mn},3} &= (1.0 - x_{\text{Mn}}, 0.5 + y_{\text{Mn}}, 0.5 - z_{\text{Mn}}) \\
\vec{r}_{\text{Mn},4} &= (0.5 + x_{\text{Mn}}, 0.5 - y_{\text{Mn}}, 1.0 - z_{\text{Mn}}) \,.
\end{aligned}$$

The Ge atoms occupy their positions according to the same provision but with their own parameters x_{Ge}, y_{Ge} and z_{Ge}. The neutron diffraction data of Makarova (see Table 7.1) also reveals that the unit cell is elongated along the c-axis for low temperatures. The direction of the c-axis coincides with the propagation direction of the 1Q helical spin spiral. The structural difference is most prominent for the measurement that was made at a temperature of 6 K.

Per se, a DFT calculation with KKR`nano` does not account for temperature effects like e.g. lattice vibrations. It is therefore advisable to compare DFT results with experimental results that are obtained at low temperatures. In this spirit we analyze the ferromagnetic state and the 1Q state with varying geometry, i.e. a transition from the $P2_13$ to the $P2_12_12_1$ space group. Subsequently, we shed light on the impact that a variation of the parameters x_{Mn}, y_{Mn} and z_{Mn} can have on the energy difference

	200 K	50 K	6 K
Space group	$P2_13$	$P2_12_12_1$	$P2_12_12_1$
Lattice parameters			
a (Å)	4.7925(25)	4.7808(24)	4.7806(30)
b (Å)		4.7807(22)	4.7805(29)
c (Å)		4.7938(30)	4.7939(10)
Atomic coordinates			
x_{Mn}	0.136(30)	0.145(40)	0.142(12)
y_{Mn}		0.129(41)	0.131(16)
z_{Mn}		0.136(36)	0.136(11)
x_{Ge}	0.846(9)	0.846(9)	0.845(6)
y_{Ge}		0.843(9)	0.843(7)
z_{Ge}		0.843(8)	0.842(6)

Table 7.1.: Structural parameters of B20-MnGe at 200 K, 50 K and 6 K. The structure can be best described by the $P2_13$ and the $P2_12_12_1$ space group, respectively. The data is deduced from the refinements of high-resolution neutron diffraction patterns. Data is taken from [120].

between these two states. The positions of the Ge atoms remain fixed and are given by $x_{\mathrm{Ge}} = y_{\mathrm{Ge}} = z_{\mathrm{Ge}} = 0.846$.

The KKR`nano` calculations are done for a $6 \times 6 \times 6$ supercell using only the Γ-point for the Brillouin zone integration. The experimentally observed slight elongation along the c-axis is accounted for by defining the Bravais matrix as

$$\begin{pmatrix} 6.0 & 0.0 & 0.0 \\ 0.0 & 6.0 & 0.0 \\ 0.0 & 0.0 & 6.0168 \end{pmatrix} \tag{7.22}$$

Once again the broadening temperature is set to $T = 800$ K and the exchange-correlation functional PBEsol is used. Linear-scaling behaviour of the multiple-scattering problem is achieved by setting the truncation radius to $r_{\mathrm{tr}} = 2.0\,a$, where a is the lattice constant of the reduced unit cell that comprises 8 atoms.

For each geometrical configuration a calculation imposing the ferromagnetic and the 1Q state is converged. The resulting individual difference of the total energies between both states is visualized in Figure 7.19 for different space group parameters $(x_{\mathrm{Mn}}, y_{\mathrm{Mn}}, z_{\mathrm{Mn}})$. We check various configurations starting with the experimentally reported parameter set $(0.142, 0.131, 0.136)$. Here, we find an energy difference of $E_{1Q} - E_{FM} = 3.5$ meV/f.u., which is not much different from the result for the $P2_13$ space group at equilibrium lattice constant (see Figure 7.15).

A shift of the z-parameter in positive or negative z-direction brings about a sharp increase of the difference of up to 14 meV indicating that the tuning of this parameter does not help in finding a geometric setup in which the 1Q state is the ground state.

Hence, we focus on shifts in the x-y-plane. In this restricted parameter space the energy difference changes only slightly and remains positive. However, minima can be found for $(0.149, 0.138, 0.136)$ and $(0.156, 0.144, 0.136)$, where $E_{1Q} - E_{FM} = 0.5$ meV/f.u.. Thus, a simultaneous increase of the parameters x_{Mn} and y_{Mn} narrows the energetic gap between FM and 1Q state.
Unfortunately, useful data could not be obtained for the parameter sets $(0.142, 0.125, 0.136)$, $(0.149, 0.125, 0.136)$ and $(0.156, 0.125, 0.136)$ as the system went into a paramagnetic state for these. This might be because the magnetic moment of the Mn atoms is sensitive to the distance between Mn and Ge atoms.

In summary it can be stated that the transition from the $P2_13$ space group to the $P2_12_12_1$ space group can narrow the energetic gap between ferromagnet and 1Q state only marginally. We can therefore assume that, at least in a DFT calculation, the observed reordering of the atoms at low temperatures does not provide an explanation to the existence of the helical spin spiral in B20-MnGe. Yet, it is interesting to see that changes of the parameters x_{Mn} and y_{Mn} by 5% do not have a significant impact on the magnetic energy landscape.

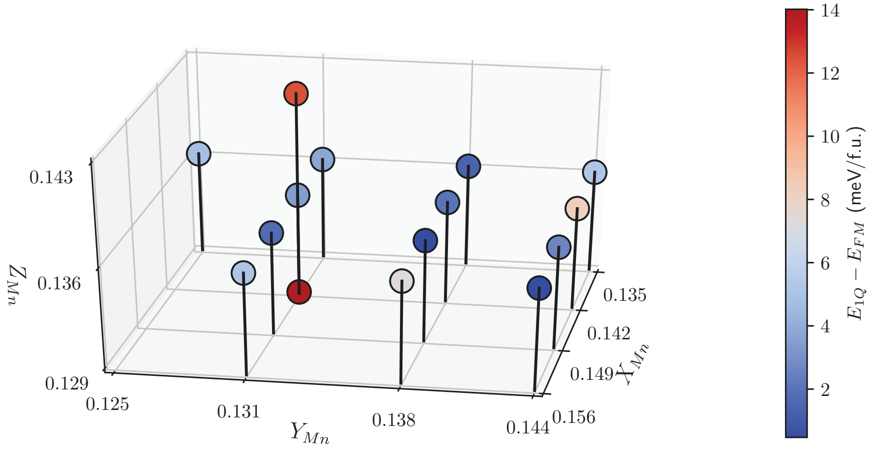

Figure 7.19.: Energy difference between ferromagnetic (FM) and 1Q helical spiral state $E_{1Q} - E_{FM}$ for different $P2_12_12_1$ space group parameter configurations.

7.4. $\mathrm{Mn}_{1-x}\mathrm{Fe}_x\mathrm{Ge}$ Alloys

So far, the focus of this chapter was exclusively on B20-MnGe. B20-FeGe is another compound which has interesting magnetic properties. It exhibits helimagnetism up to a transition temperature of 278 K in bulk crystals [137]. Recently, a new type of chiral object, which was named the chiral bobber, was predicted theoretically in thin films of B20-FeGe and shortly after observed in transmission electron microscopy experiments [27]. In this section we examine the magnetic parameters of B20-$\mathrm{Mn}_{1-x}\mathrm{Fe}_x\mathrm{Ge}$ alloys with varying ratios of Mn and Fe. Subsequently, we investigate the magnetic Bloch point state in B20-FeGe with artificially enhanced spin-orbit coupling.

7.4.1. Magnetic Parameters

Both experimentalists and theoreticians have not only investigated *pure* B20 compounds but also alloys that contain two different transition metals, namely portions of Mn and Fe [117, 138].

The lattice constant of B20-FeGe is $a = 4.7$ Å and its structure is described by the $P2_13$ space group parameters $u_{\mathrm{Fe}} = 0.136$ and $u_{\mathrm{Ge}} = 0.842$ [117]. Like B20-MnGe, B20-FeGe exhibits a chiral magnetic ground state with a pitch of $\lambda = 70$ nm [26]. This is much larger than the helical pitch of 3-6 nm which can be found in B20-MnGe [28]. The magnetic chirality of B20-MnGe coincides with the crystal chirality, i.e. if the crystal is right-handed, the helical spin spiral is right-handed too. Contrarily, in B20-FeGe the chiralities are opposed, so that in a right-handed crystal a left-handed spin spiral is observed [117].

As of today, systems that demand length scales significantly larger than 10 nm cannot be treated with KKR`nano`. This is on the one hand due to the lack of sufficient supercomputing resources and on the other hand aggravated by a slowdown of the convergence of the DFT self-consistency cycle for such super-large systems. We therefore initially restrict our investigations to the familiar atomistic spin model and the micromagnetic model that was introduced in section 7.2 but then make an attempt to stabilize a non-trivial magnetic texture in a $6 \times 6 \times 6$ supercell by tuning the SOC strength in section 7.4.2.

Recently, Gayles et al. [134] and Mankovsky et al. [139] extracted the micromagnetic DMI from DFT calculations for varying amounts of Mn and Fe in the B20-alloy $\mathrm{Mn}_{1-x}\mathrm{Fe}_x\mathrm{Ge}$.

Gayles used the virtual crystal approximation (VCA) in his calculations, i.e. the core charge of each transition metal atom is adjusted to a (non-integer) value that reflects the ratio of Mn and Fe, e.g. for $x_{\mathrm{Fe}} = 0.6$ the charge is set to $Z = 25.6$. Mankovsky relied on the coherent potential approximation (CPA) [140] which is more accurate. In this particular case, CPA means that the Green function G is replaced by an average Green function $< G >$ whose constituents are determined by two independent multiple-scattering calculations, where the transition metal is Mn and Fe, respectively.

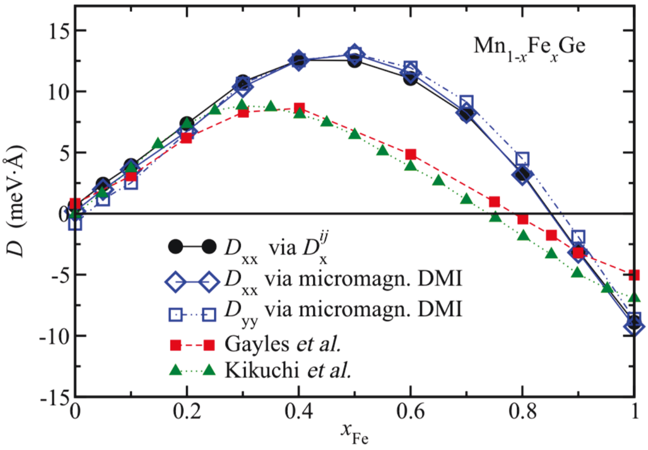

Figure 7.20.: Value of DMI depending on the Fe concentration x_{Fe} as calculated by Mankovsky et al. using CPA compared to results of Gayles and Kuckuchi who use VCA in their calculations. A sign change occurs in all calculations at $x_{\text{Fe}} \approx 0.8$. Reprinted with permission from [139]. Copyright 2018 by the American Physical Society.

The results by Mankovsky [139], Gayles [134] and Kikuchi [141], who also performed a VCA analysis, are depicted in Figure 7.20.

Both CPA and VCA yield qualitatively similar results but the enhancement of the DMI around $x = 0.5$ is more pronounced in CPA. The DMI in B20-MnGe is particularly small but has a positive sign, i.e. the magnetic chirality corresponds to the crystal chirality, while for B20-FeGe the sign is clearly negative and hence the chiralities are opposed, as reported from experiment.

We extract magnetic coupling parameters with KKR using VCA for nuclear charges of $Z = 25.0$, $Z = 25.2$, $Z = 25.4$, $Z = 25.6$, $Z = 25.8$ and $Z = 26.0$. The lattice constant is adjusted linearly depending on the Fe concentration x so that $a = x \cdot a_{\text{FeGe}} + (1-x) \cdot a_{\text{MnGe}}$, where $a_{\text{FeGe}} = 4.7$ Å and $a_{\text{MnGe}} = 4.8$ Å. We use a mesh with 60x60x60 k-points. Since the parameters $u_{\text{Fe/Mn}}$ and u_{Ge} do not differ much between B20-FeGe and B20-MnGe we keep them fixed at $u_{\text{Fe/Mn}} = 0.135$ and $u_{\text{Ge}} = 0.842$. LDA is used as exchange-correlation functional.

The results of our detailed analysis of the magnetic coupling coefficients can be found in Figure 7.21, where the atomistic model parameters for the isotropic exchange J_{ij} and the absolute values of the DM interaction vectors $\left|\vec{D}_{ij}\right|$ as well as the derived micromagnetic quantities A for the spin-stiffness and D for the DM interaction are depicted. These quantities were already introduced in section 7.2.1.

The isotropic Heisenberg coupling strength between first-nearest neighbours ranges from slightly more than 7 meV for $x_{\mathrm{Fe}} = 1.0$ and almost 20 meV for $x_{\mathrm{Fe}} = 0.2$. All alloys show magnetic frustration, i.e. the coupling to the next-nearest neighbour is anti-ferromagnetic for any x_{Fe}. However, the sign fluctuation of interactions between more remote neighbours is stronger for small x_{Fe}, i.e. for an alloy whose properties are comparable to pure B20-MnGe.

For the absolute values of the DMI vectors it can be observed that the amplitude of the third-nearest neighbour interaction differs substantially depending on x_{Fe}. While for $x_{\mathrm{Fe}} = 1$ the DMI vector is just slightly larger than it is for the second-nearest neighbour, for $x_{\mathrm{Fe}} = 0.2$ a peak at 0.35 meV is found which is not that much smaller than the first-nearest neighbour DMI vector with 0.5 meV.

Converging the spin-stiffness A for B20-MnGe has already turned out to be difficult in section 7.2. It is therefore not surprising that A is fluctuating for alloys with a large portion of Mn, even if distances of up to $4a$ are taken into account.

Interestingly, this issue does not seem to be conveyed to B20-FeGe. For $x_{\mathrm{Fe}} = 1.0$ the spin-stiffness is almost constant beyond a neighbour distance of approximately $2.5a$.

A similar convergence problem can be observed for the micromagnetic DMI. The fluctuations with increasing distance are more pronounced for alloys with a large Mn ratio.

The pitch of the helical spiral in B20-FeGe in the picture of competing isotropic and asymmetric interaction is given by eq. (7.10). From Figure 7.21 we can estimate $A = 250\ \mathrm{meV{\cdot}\mathring{A}}^2$ and $D = -2\ \mathrm{meV{\cdot}\mathring{A}}$ which yields $\lambda = 150$ nm. This is more than twice the pitch that is reported in experiment. An explanation for this is yet to be found.

In order to illustrate the evolution of the micromagnetic DMI in KKR with increasing substitution of Mn by Fe and to better compare with Figure 7.20 the DMI converged up to $4a$ is depicted in Figure 7.22.

In comparison with Figure 7.20 we find a similar behaviour, where DMI is small for $x_{\mathrm{Fe}} = 0$ and peaks around $x_{\mathrm{Fe}} = 0.4$. The maximum DMI value of about 10 $\mathrm{meV{\cdot}\mathring{A}}$ is comparable to the results obtained by Mankovski and Gayles. Note, that also the sign change that occurs close to $x_{\mathrm{Fe}} = 1.0$ is predicted correctly.

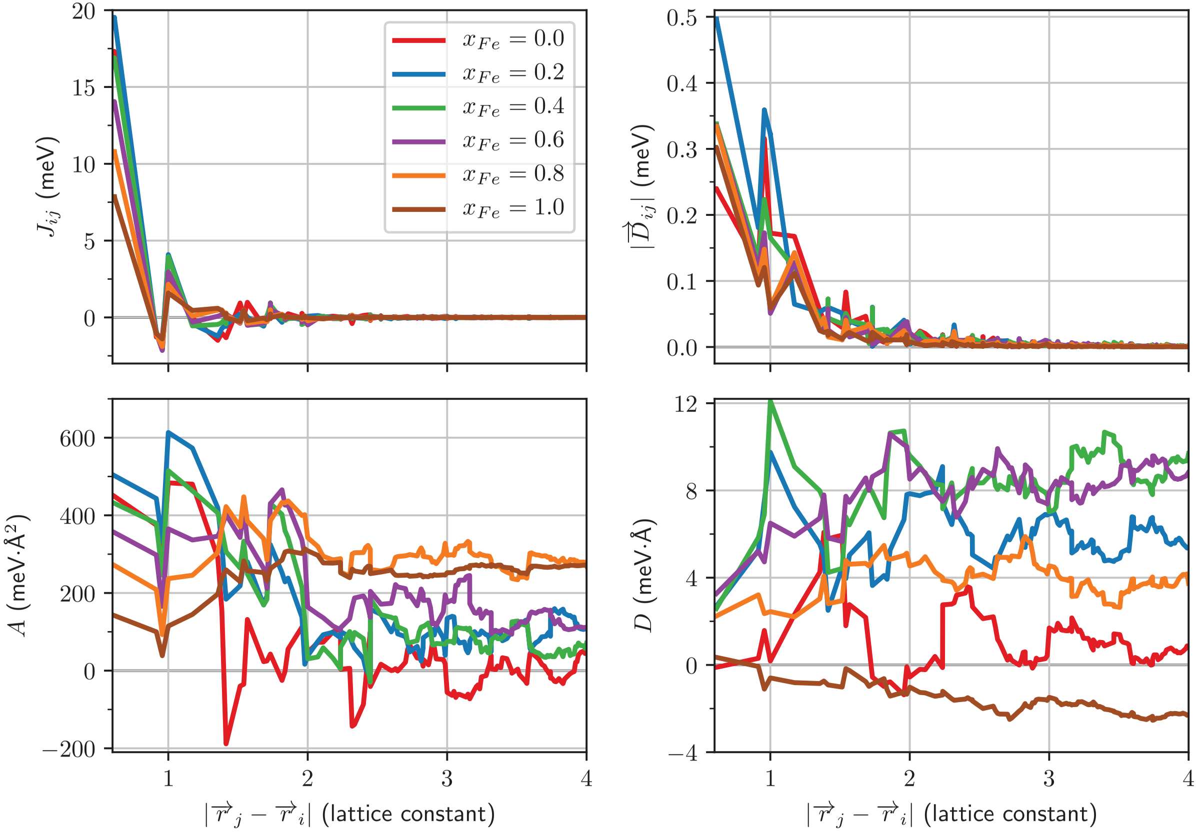

Figure 7.21.: Isotropic magnetic exchange couplings (J_{ij}) and absolute values of the DMI vectors ($\left|\vec{D_{ij}}\right|$) as function of distance between atoms i and j derived from an ab initio calculation with KKR using the LDA functional as function of distance between atoms i and j. The colors indicate the nuclear charge which is tuned from Mn ($x_{\mathrm{Fe}} = 0.0$) to Fe ($x_{\mathrm{Fe}} = 1.0$). For all nuclear charges the sign of J_{ij} alternates with distance giving rise to magnetic frustration as a positive (negative) value corresponds to (anti-)ferromagnetic coupling between two atoms. This long-range behaviour is particularly pronounced for $x_{\mathrm{Fe}} \leq 0.4$. The micromagnetic spin-stiffness A and the micromagnetic DMI D converges only nicely for $x_{\mathrm{Fe}} = 1.0$.

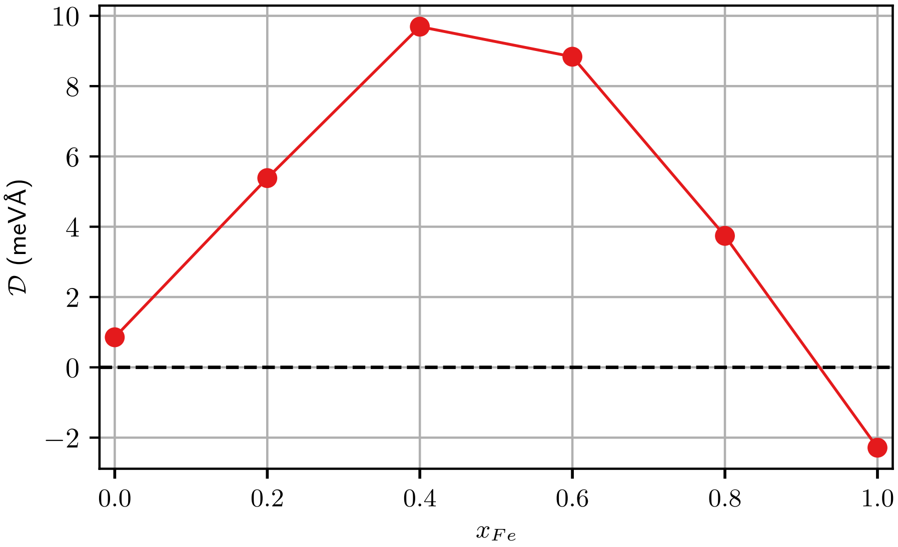

Figure 7.22.: Micromagnetic DMI D of the B20-alloy $\mathrm{Mn}_{1-x}\mathrm{Fe}_x\mathrm{Ge}$ for x ranging from 0 to 1. The DMI is converged up to an interatomic distance of $4a$, where a is the lattice constant. For B20-MnGe the sign of the DMI is positive while it is negative for B20-FeGe.

7.4.2. Bloch Point State

We once more investigate the Bloch point (BP) as a magnetic texture but this time in B20-FeGe. A description of the BP and an analysis of it in B20-MnGe is given in section 7.3.1.

To this aim we initialize a KKR`nano` calculation for a $6 \times 6 \times 6$ supercell with a $2 \times 2 \times 2$ k-point-mesh and the LDA exchange-correlation functional. As in section 7.3.1 the SOC strength is scaled by a factor f_{SOC} from 1.0 (no enhancement) to 4.0. The magnetic moments are allowed to relax.

The energy difference $E_{\mathrm{BP}} - E_{\mathrm{FM}}$ between Bloch point state and ferromagnet as well as the magnetic moment of both states with varied SOC strength is depicted in Figure 7.23. For a scaling factor of up to $f_{\mathrm{SOC}} = 3.4$ the difference is constant and amounts to $E_{\mathrm{BP}} - E_{\mathrm{FM}} = 0.5$ meV per formula unit. As for B20-MnGe (see Figure 7.17) the ferromagnet remains the ground state unless SOC is enhanced by almost a factor of 4. At this point the BP is energetically preferable. Yet, while an enhancement by $f_{\mathrm{SOC}} = 3.5$ is sufficient to drive B20-MnGe into a non-trivial ground state, for B20-FeGe it must be enhanced by $f_{\mathrm{SOC}} = 4.0$. Note, that the former exhibits a shorter helical pitch than the latter. It is therefore consistent that a non-trivial texture can be

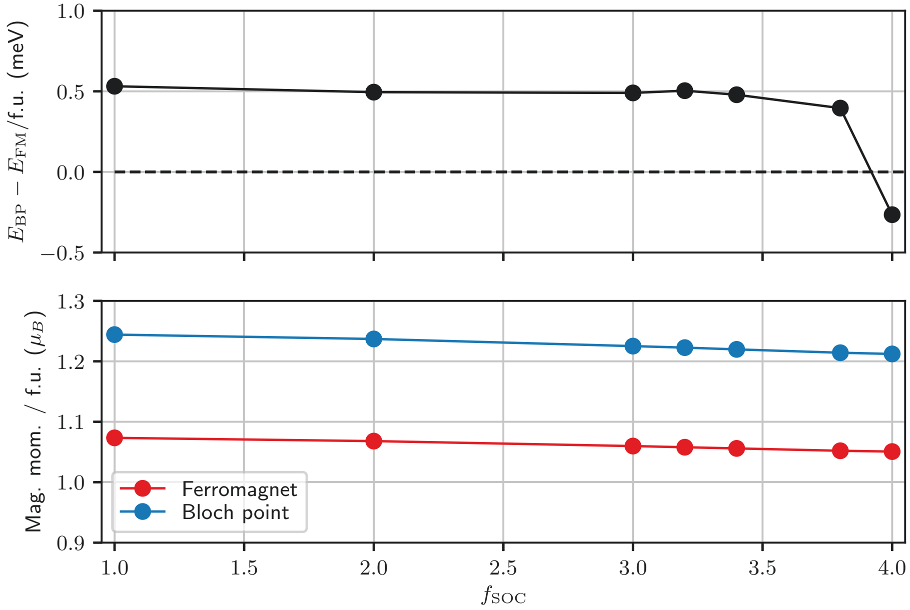

Figure 7.23.: Effect of increased SOC on B20-FeGe in a $6 \times 6 \times 6$ supercell. Top: Total energy difference between (relaxed) Bloch point and (relaxed) ferromagnet. Bottom: Magnetic moment of ferromagnet and Bloch point.

stabilized with less enhancement of SOC in B20-MnGe.
The total magnetic moment differs between the two states by roughly 0.15 μ_B. Both in absolute as well as relative values this is more than what we found for B20-MnGe.

8

Conclusions

The work that is presented in this thesis covers on the one hand the further development of the large-scale Density Functional Theory code KKR`nano`. On the other hand, results of simulations of exotic magnetic textures that are of the size of several nanometers are presented. This has become feasible only due to the implementation of an extended Korringa-Kohn-Rostoker (KKR) scheme in KKR`nano` that accounts for non-collinear magnetism and spin-orbit coupling (SOC).

The rather large portion of methodological work that was done is reflected in the chapters on Density Functional Theory (DFT), the KKR Green function method and KKR`nano`. The KKR method and its linear-scaling variant, which is used in KKR`nano`, are presented. Furthermore, matters concerning high performance computing (HPC) are discussed. These are mainly the parallelization strategy and the preparation for upcoming heterogeneous supercomputers that will heavily rely on Graphics Processing Units (GPUs). The newly added functionality to solve the multiple-scattering problem on GPUs is presented and the potential pitfall of floating-point accuracy is exemplified. Additionally, it is shown that KKR`nano` can be used for systems that contain up to 230,000 atoms on the supercomputer JUQUEEN. In the chapter on new methodological implementations, it is described how non-collinear magnetism was implemented by introducing the concept of local and global spin frame of reference. This is followed by an explanation of relativistic effects and in particular of how SOC was added to KKR`nano`. A subsequent attempt to correctly capture the large magnetocrystalline anisotropy energy (MCE) in $IrMn_3$ shows that the implementation works accurately. Apart from this, three important extensions to KKR`nano` that were (re-)established are presented. The generalized gradient approximation (GGA) offers an additional and usually preferable way of approximating the exchange-correlation functional as calculations of the equilibrium lattice constant with KKR`nano` show. In order to calculate the electronic charge density correctly, Lloyd's formula was re-implemented in KKR`nano`. Sample calculations of the density of states of $SrTiO_3$ show how the Fermi level is placed correctly inside the band gap, when Lloyd's formula is used. The newly added possibility to split the energy integration contour into a semi-core contour and a valence contour provides a tool to use broad energy contours without having to add many more integration points to it.

Finally, the last chapter is focused on the magnetic B20 materials, in particular

B20-MnGe and B20-FeGe and the B20-$\mathrm{Mn}_{1-x}\mathrm{Fe}_x\mathrm{Ge}$ alloys. An initial calculation of the energy-resolved density of states shows that in B20-MnGe the 3d-states of Mn are the important states for the investigation of magnetic phenomena as only these states contribute significantly to the electronic density around the Fermi level. The experimentally confirmed pressure-induced transition from a high-spin to a low-spin regime in this material is correctly predicted by KKR`nano` as an analysis with varied lattice parameters shows. Here, the description of the exchange-correlation potential with GGA works better since it yields a global energy minimum for the high-spin state while LDA falsely predicts the low-spin state to be the ground state. A closer look at the MCE of B20-MnGe showed that the magnetic force theorem does not yield reasonable results for this system. Instead, a comparison of converged total energies reproduces more or less the correct cubic anisotropy characteristics, apart from some deviations that require further investigation. The atomistic magnetic model parameters that can be obtained with KKR do not give a satisfactory answer to the question of how helical magnetism comes about in B20-MnGe. The magnetic ordering temperature which is estimated by a Monte-Carlo simulation in combination with the magnetic model parameters is 100 K higher than it should be according to experiment. The micromagnetic quantities cannot be fully converged but anyway the conclusion can be drawn that the atomic Dzyaloshinskii-Moriya interaction is small and does not play a decisive role in the formation of the short-pitch helical objects which are reported from experiment. Rather, the magnetic frustration that is shown by the isotropic exchange interaction parameters appears to be a crucial effect in B20-MnGe. This frustration alone gives rise to metastable topologically protected objects in B20-MnGe. In atomistic spin dynamics simulations a Bloch-type skyrmion and an antiskyrmion can be observed. In a KKR`nano` calculation it is found that the helical spiral state and the skyrmion lattice state are energetically preferable over the trivial ferromagnetic state, if the lattice parameter is increased by roughly 5% compared to the equilibrium lattice constant. This result could potentially explain the experimental observation of the skyrmion lattice since in experiment the crystal structure often deviates from the ideal structure due to the preparation process of the sample. Instead of varying the lattice constant, also the strength of spin-orbit coupling can artificially be increased. An increase by at least a factor of 3.5 makes the Bloch point energetically preferable over the ferromagnet in B20-MnGe. In a layered system with 5 layers of B20-MnGe unit cells it can be observed that the magnetic moment of the Mn atoms almost doubles in the transition layer next to the vacuum. The introduction of further spatial degrees of freedom by adopting the $P2_12_12_1$ space group coordinates allows one to reduce the energy gap between helical and ferromagnetic state but does not provide a way to close it completely.

An Investigation of the B20-$\mathrm{Mn}_{1-x}\mathrm{Fe}_x\mathrm{Ge}$ alloys with varied concentration of Mn and Fe showed that KKR can reproduce the findings of other groups, i.e. the amplitude and the sign of the Dzyaloshinskiii-Moriya interaction. The sign change between pure B20-MnGe and pure B20-FeGe explains why helical spirals with opposite chirality are observed in both systems. Like in B20-MnGe, it is found that the Bloch point texture can also be stabilized in B20-FeGe, albeit with a stronger scaling of SOC than in B20-MnGe.

A Appendix

A.1. Equation of Motion for Spin Densities in a Magnetic Field

In this appendix it is shown that

$$\begin{aligned}&\frac{1}{2i}\left\{\psi_i^\dagger(\vec{r},t)\hat{\sigma}H_{KS}^{\alpha\beta}\psi_i(\vec{r},t)-\left[H_{KS}^{\alpha\beta}\psi_i(\vec{r},t)\right]^\dagger\hat{\sigma}\psi_i(\vec{r},t)\right\}\\ =&\frac{1}{4i}\nabla\cdot\left\{\left[\nabla\psi_i^\dagger(\vec{r},t)\hat{\sigma}\right]\psi_i(\vec{r},t)-\psi_i^\dagger(\vec{r},t)\hat{\sigma}\nabla\psi_i(\vec{r},t)\right\}-\gamma\vec{s}\times\vec{B}_{eff}(\vec{r},t),\end{aligned}\tag{A.1}$$

where the Kohn-Sham Hamiltonian is given by

$$\begin{aligned}H_{KS}^{\alpha\beta}&=-\nabla^2\delta^{\alpha\beta}+V_{\text{eff}}^{\alpha\beta}(\vec{r},t)\\ &=-\nabla^2\delta^{\alpha\beta}+V_0(\vec{r},t)\delta^{\alpha\beta}+\hat{\sigma}\cdot\vec{B}_{\text{eff}}(\vec{r},t).\end{aligned}\tag{A.2}$$

To this aim we first show that $H_{KS,1}^{\alpha\beta}=-\nabla^2$, which accounts for the kinetic energy in the Hamiltonian, fulfills the relation

$$\begin{aligned}&\frac{1}{2i}\left\{\psi_i^\dagger(\vec{r},t)\hat{\sigma}H_{KS,1}^{\alpha\beta}\psi_i(\vec{r},t)-\left[H_{KS,1}^{\alpha\beta}\psi_i(\vec{r},t)\right]^\dagger\hat{\sigma}\psi_i(\vec{r},t)\right\}\\ =&\frac{1}{4i}\nabla\cdot\left\{\left[\hat{\sigma}\nabla\psi_i^\dagger(\vec{r},t)\right]\psi_i(\vec{r},t)-\psi_i^\dagger(\vec{r},t)\hat{\sigma}\nabla\psi_i(\vec{r},t)\right\}.\end{aligned}\tag{A.3}$$

The right side of the equation can be converted to the left side as follows:

$$\begin{aligned}&\frac{1}{4i}\nabla\cdot\left\{\left[\nabla\psi_i^\dagger(\vec{r},t)\hat{\sigma}\right]\psi_i(\vec{r},t)-\psi_i^\dagger(\vec{r},t)\hat{\sigma}\nabla\psi_i(\vec{r},t)\right\}\\ =&\frac{1}{4i}\left[\nabla^2\psi_i^\dagger(\vec{r},t)\hat{\sigma}\psi_i(\vec{r},t)+\nabla\psi_i^\dagger(\vec{r},t)\hat{\sigma}\nabla\psi_i(\vec{r},t)-\nabla\psi_i^\dagger(\vec{r},t)\hat{\sigma}\nabla\psi_i(\vec{r},t)-\psi_i^\dagger(\vec{r},t)\hat{\sigma}\nabla^2\psi_i(\vec{r},t)\right]\\ =&\frac{1}{4i}\left[\nabla^2\psi_i^\dagger(\vec{r},t)\hat{\sigma}\psi_i(\vec{r},t)-\psi_i^\dagger(\vec{r},t)\hat{\sigma}\nabla^2\psi_i(\vec{r},t)\right]\\ =&\frac{1}{4i}\left[2\psi_i^\dagger(\vec{r},t)\hat{\sigma}H_{KS,1}^{\alpha\beta}\psi_i(\vec{r},t)-2H_{KS,1}^{\alpha\beta}\psi_i^\dagger(\vec{r},t)\hat{\sigma}\psi_i(\vec{r},t)\right]\\ =&\frac{1}{2i}\left[\psi_i^\dagger(\vec{r},t)\hat{\sigma}H_{KS,1}^{\alpha\beta}\psi_i(\vec{r},t)-H_{KS,1}^{\alpha\beta}\psi_i^\dagger(\vec{r},t)\hat{\sigma}\psi_i(\vec{r},t)\right]\qquad\square.\end{aligned}\tag{A.4}$$

The constant potential in the Hamiltonian is modelled by $H^{\alpha\beta}_{KS,2} = V_0(\vec{r},t)$. We exploit that $[V_0(\vec{r},t), \hat{\sigma}] = 0$ and can thus show that the dynamics are not affected by V_0:

$$\begin{aligned}
&\frac{1}{2i}\left\{\psi_i^\dagger(\vec{r},t)\hat{\sigma}H^{\alpha\beta}_{KS,2}\psi_i(\vec{r},t) - \left[H^{\alpha\beta}_{KS,2}\psi_i(\vec{r},t)\right]^\dagger\hat{\sigma}\psi_i(\vec{r},t)\right\}\\
=&\frac{1}{2i}\left\{\psi_i^\dagger(\vec{r},t)\hat{\sigma}V_0(\vec{r},t)\psi_i(\vec{r},t) - \left[V_0(\vec{r},t)\psi_i(\vec{r},t)\right]^\dagger\hat{\sigma}\psi_i(\vec{r},t)\right\}\\
=&\frac{1}{2i}\left\{\psi_i^\dagger(\vec{r},t)\hat{\sigma}V_0(\vec{r},t)\psi_i(\vec{r},t) - \psi_i^\dagger(\vec{r},t)V_0(\vec{r},t)\hat{\sigma}\psi_i(\vec{r},t)\right\}\\
=&\frac{1}{2i}\left\{\psi_i^\dagger(\vec{r},t)\hat{\sigma}V_0(\vec{r},t)\psi_i(\vec{r},t) - \psi_i^\dagger(\vec{r},t)\hat{\sigma}V_0(\vec{r},t)\psi_i(\vec{r},t)\right\}\\
=&0 \qquad \square.
\end{aligned} \tag{A.5}$$

Showing that for $H^{\alpha\beta}_{KS,3} = \hat{\sigma}\cdot\vec{B}_{\text{eff}}(\vec{r},t)$

$$\begin{aligned}
&\frac{1}{2i}\left\{\psi_i^\dagger(\vec{r},t)\hat{\sigma}H^{\alpha\beta}_{KS,3}\psi_i(\vec{r},t) - \left[H^{\alpha\beta}_{KS,3}\psi_i(\vec{r},t)\right]^\dagger\hat{\sigma}\psi_i(\vec{r},t)\right\}\\
=&-\gamma\vec{s}\times\vec{B}_{eff}(\vec{r},t),
\end{aligned} \tag{A.6}$$

requires knowledge of the two algebraic relations

$$\hat{\sigma}\left(\hat{\sigma}\cdot\vec{B}_{\text{eff}}\right) = \vec{B}_{\text{eff}} - i\left(\hat{\sigma}\times\vec{B}_{\text{eff}}\right) \tag{A.7}$$

$$\hat{\sigma}\left(\vec{B}_{\text{eff}}\cdot\hat{\sigma}\right) = \vec{B}_{\text{eff}} + i\left(\hat{\sigma}\times\vec{B}_{\text{eff}}\right) \tag{A.8}$$

which can be derived by applying the commutation and anticommuntation relations of the Pauli matrices. Then, the correctness of eq. (A.6) can be confirmed by

$$\begin{aligned}
&\frac{1}{2i}\left\{\psi_i^\dagger(\vec{r},t)\hat{\sigma}H^{\alpha\beta}_{KS,3}\psi_i(\vec{r},t) - \left[H^{\alpha\beta}_{KS,3}\psi_i(\vec{r},t)\right]^\dagger\hat{\sigma}\psi_i(\vec{r},t)\right\}\\
=&\frac{1}{2i}\left\{\psi_i^\dagger(\vec{r},t)\hat{\sigma}\hat{\sigma}\vec{B}_{\text{eff}}(\vec{r},t)\psi_i(\vec{r},t) - \left[\hat{\sigma}\vec{B}_{\text{eff}}(\vec{r},t)\psi_i(\vec{r},t)\right]^\dagger\hat{\sigma}\psi_i(\vec{r},t)\right\}\\
=&\frac{1}{2i}\left\{\psi_i^\dagger(\vec{r},t)\hat{\sigma}\hat{\sigma}\vec{B}_{\text{eff}}(\vec{r},t)\psi_i(\vec{r},t) - \psi_i^\dagger(\vec{r},t)\hat{\sigma}\vec{B}_{\text{eff}}(\vec{r},t)\hat{\sigma}\psi_i(\vec{r},t)\right\}\\
=&\frac{1}{2i}\left\{\psi_i^\dagger(\vec{r},t)\left(\vec{B}_{\text{eff}} - i\left(\hat{\sigma}\times\vec{B}_{\text{eff}}\right)\right)\psi_i(\vec{r},t) - \psi_i^\dagger(\vec{r},t)\left(\vec{B}_{\text{eff}} + i\left(\hat{\sigma}\times\vec{B}_{\text{eff}}\right)\right)\psi_i(\vec{r},t)\right\}\\
=&-\psi_i^\dagger(\vec{r},t)\left(\hat{\sigma}\times\vec{B}_{\text{eff}}\right)\psi_i(\vec{r},t)\\
=&-\left(\psi_i^\dagger(\vec{r},t)\hat{\sigma}\psi_i(\vec{r},t)\right)\times\vec{B}_{\text{eff}}\\
=&-2\vec{s}\times\vec{B}_{\text{eff}}\\
\approx&-\gamma\vec{s}\times\vec{B}_{\text{eff}} \qquad \square.
\end{aligned} \tag{A.9}$$

In the end we substitute $\hat{\sigma}$ with the electronic spin $\vec{s} = \frac{1}{2}\langle\hat{\sigma}\rangle$ and replace 2 with the gyromagnetic ratio $\gamma \approx 2.00232$ which accounts for effects that go beyond the Dirac picture.

Bibliography

[1] E. Schrödinger, “Quantisierung als Eigenwertproblem”, Annalen der Physik **384**, 361–376 (1926).

[2] P. A. M. Dirac, “The Quantum Theory of the Electron”, Proceedings of the Royal Society A: Mathematical, Physical and Engineering Sciences **117**, 610–624 (1928).

[3] F. Bloch, “Über die Quantenmechanik der Elektronen in Kristallgittern”, Zeitschrift für Physik **52**, 555–600 (1929).

[4] R. P. Feynman, “Simulating physics with computers”, International Journal of Theoretical Physics **21**, 467–488 (1982).

[5] P. Hohenberg and W. Kohn, “Inhomogeneous Electron Gas”, Physical Review **136**, B864–B871 (1964).

[6] R. O. Jones, “Density functional theory: Its origins, rise to prominence, and future”, Reviews of Modern Physics **87**, 897–923 (2015).

[7] P. J. Hasnip, K. Refson, M. I. J. Probert, J. R. Yates, S. J. Clark, and C. J. Pickard, “Density functional theory in the solid state”, Philosophical Transactions of the Royal Society A: Mathematical, Physical and Engineering Sciences **372**, 20130270–20130270 (2014).

[8] R. Car and M. Parrinello, “Unified Approach for Molecular Dynamics and Density-Functional Theory”, Physical Review Letters **55**, 2471–2474 (1985).

[9] G. Binasch, P. Grünberg, F. Saurenbach, and W. Zinn, “Enhanced magnetoresistance in layered magnetic structures with antiferromagnetic interlayer exchange”, Physical Review B **39**, 4828–4830 (1989).

[10] M. N. Baibich, J. M. Broto, A. Fert, F. N. Van Dau, F. Petroff, P. Etienne, G. Creuzet, A. Friederich, and J. Chazelas, “Giant Magnetoresistance of (001)Fe/(001)Cr Magnetic Superlattices”, Physical Review Letters **61**, 2472–2475 (1988).

[11] M. Bode, M. Heide, K. von Bergmann, P. Ferriani, S. Heinze, G. Bihlmayer, A. Kubetzka, O. Pietzsch, S. Blügel, and R. Wiesendanger, “Chiral magnetic order at surfaces driven by inversion asymmetry”, Nature **447**, 190–193 (2007).

[12] P. Ferriani, K. von Bergmann, E. Y. Vedmedenko, S. Heinze, M. Bode, M. Heide, G. Bihlmayer, S. Blügel, and R. Wiesendanger, “Atomic-Scale Spin Spiral with a Unique Rotational Sense: Mn Monolayer on W(001)”, Physical Review Letters **101**, 027201 (2008).

[13] T. Skyrme, “A unified field theory of mesons and baryons”, Nuclear Physics **31**, 556–569 (1962).

[14] A. Bogdanov and A. Hubert, “Thermodynamically stable magnetic vortex states in magnetic crystals”, Journal of Magnetism and Magnetic Materials **138**, 255–269 (1994).

[15] S. Mühlbauer, B. Binz, F. Jonietz, C. Pfleiderer, A. Rosch, A. Neubauer, R. Georgii, and P. Boni, “Skyrmion Lattice in a Chiral Magnet”, Science **323**, 915–919 (2009).

[16] S. Heinze, K. von Bergmann, M. Menzel, J. Brede, A. Kubetzka, R. Wiesendanger, G. Bihlmayer, and S. Blügel, “Spontaneous atomic-scale magnetic skyrmion lattice in two dimensions”, Nature Physics **7**, 713–718 (2011).

[17] A. Fert, N. Reyren, and V. Cros, “Magnetic skyrmions: advances in physics and potential applications”, Nature Reviews Materials **2**, 17031 (2017).

[18] Reinsel, David, Gantz, John, and Rydning, John, *Data Age 2025: The Evolution of Data to Life-Critical Don’t Focus on Big Data; Focus on the Data That’s Big*, White Paper (IDC, Apr. 2017).

[19] A. Thiess, R. Zeller, M. Bolten, P. H. Dederichs, and S. Blügel, “Massively parallel density functional calculations for thousands of atoms: KKRnano”, Physical Review B **85**, 235103 (2012).

[20] J. Dongarra et al., “The International Exascale Software Project roadmap”, The International Journal of High Performance Computing Applications **25**, 3–60 (2011).

[21] N. Papanikolaou, R. Zeller, and P. H. Dederichs, “Conceptual improvements of the KKR method”, Journal of Physics: Condensed Matter **14**, 2799–2823 (2002).

[22] D. S. G. Bauer, *Development of a relativistic full-potential first-principles multiple scattering Green function method applied to complex magnetic textures of nano structures at surfaces*, Schriften des Forschungszentrums Jülich Reihe Schlüsseltechnologien Bd. 79 (Forschungszentrum Jülich, Jülich, 2014).

[23] *Spirit spin simulation framework (see spirit-code.github.io).*

[24] N. Kanazawa, S. Seki, and Y. Tokura, “Noncentrosymmetric Magnets Hosting Magnetic Skyrmions”, Advanced Materials **29**, 1603227 (2017).

[25] N. Kanazawa, J.-H. Kim, D. S. Inosov, J. S. White, N. Egetenmeyer, J. L. Gavilano, S. Ishiwata, Y. Onose, T. Arima, B. Keimer, and Y. Tokura, “Possible skyrmion-lattice ground state in the B 20 chiral-lattice magnet MnGe as seen via small-angle neutron scattering”, Physical Review B **86**, 134425 (2012).

[26] X. Z. Yu, N. Kanazawa, Y. Onose, K. Kimoto, W. Z. Zhang, S. Ishiwata, Y. Matsui, and Y. Tokura, “Near room-temperature formation of a skyrmion crystal in thin-films of the helimagnet FeGe”, Nature Materials **10**, 106–109 (2011).

[27] F. Zheng, F. N. Rybakov, A. B. Borisov, D. Song, S. Wang, Z.-A. Li, H. Du, N. S. Kiselev, J. Caron, A. Kovács, M. Tian, Y. Zhang, S. Blügel, and R. E. Dunin-Borkowski, "Experimental observation of chiral magnetic bobbers in B20-type FeGe", Nature Nanotechnology **13**, 451–455 (2018).

[28] T. Tanigaki, K. Shibata, N. Kanazawa, X. Yu, Y. Onose, H. S. Park, D. Shindo, and Y. Tokura, "Real-Space Observation of Short-Period Cubic Lattice of Skyrmions in MnGe", Nano Letters **15**, 5438–5442 (2015).

[29] T. Koretsune, N. Nagaosa, and R. Arita, "Control of Dzyaloshinskii-Moriya interaction in Mn1-xFexGe: a first-principles study", Scientific Reports **5**, 13302 (2015).

[30] E. Altynbaev, S.-A. Siegfried, E. Moskvin, D. Menzel, C. Dewhurst, A. Heinemann, A. Feoktystov, L. Fomicheva, A. Tsvyashchenko, and S. Grigoriev, "Hidden quantum phase transition in Mn1-xFexGe evidenced by small-angle neutron scattering", Physical Review B **94**, 174403 (2016).

[31] M. Deutsch, O. L. Makarova, T. C. Hansen, M. T. Fernandez-Diaz, V. A. Sidorov, A. V. Tsvyashchenko, L. N. Fomicheva, F. Porcher, S. Petit, K. Koepernik, U. K. Rößler, and I. Mirebeau, "Two-step pressure-induced collapse of magnetic order in the MnGe chiral magnet", Physical Review B **89**, 180407(R) (2014).

[32] S. Blügel, Institute for Advanced Simulation, and Peter Grünberg Institut, eds., *Computing solids: models, ab-initio methods and supercomputing ; lecture notes of the 45th IFF Spring Schoool 2014, on March 10 - 21, 2014*, Schriften des Forschungszentrums Jülich Reihe Schlüsseltechnologien Bd. 74 (Forschungszentrum Jülich GmbH, Jülich, 2014).

[33] A. R. Thieß, *Development and application of a massively parallel KKR Green function method for large scale systems*, Schriften des Forschungszentrums Jülich Reihe Schlüsseltechnologien Bd. 71 (Forschungszentrum Jülich, Jülich, 2013).

[34] S. Lounis, *Theory of magnetic transition metal nanoclusters on surfaces*, Schriften des Forschungszentrums Jülich Materie und Material Bd. 41 (Forschungszentrum, Zentralbibliothek, Jülich, 2007).

[35] M. Born and R. Oppenheimer, "Zur Quantentheorie der Molekeln", Annalen der Physik **389**, 457–484 (1927).

[36] M. Levy, "Universal variational functionals of electron densities, first-order density matrices, and natural spin-orbitals and solution of the v-representability problem", Proceedings of the National Academy of Sciences **76**, 6062–6065 (1979).

[37] W. Kohn and L. J. Sham, "Self-Consistent Equations Including Exchange and Correlation Effects", Physical Review **140**, A1133–A1138 (1965).

[38] R. M. Martin, *Electronic structure: basic theory and practical methods* (Cambridge University Press, Cambridge, UK ; New York, 2004).

[39] M. Pant and A. Rajagopal, “Theory of inhomogeneous magnetic electron gas”, Solid State Communications **10**, 1157–1160 (1972).

[40] J. P. Perdew, K. Burke, and M. Ernzerhof, “Generalized Gradient Approximation Made Simple”, Physical Review Letters **77**, 3865–3868 (1996).

[41] J. P. Perdew, A. Ruzsinszky, G. I. Csonka, O. A. Vydrov, G. E. Scuseria, L. A. Constantin, X. Zhou, and K. Burke, “Restoring the Density-Gradient Expansion for Exchange in Solids and Surfaces”, Physical Review Letters **100**, 136406 (2008).

[42] J. P. Perdew, J. A. Chevary, S. H. Vosko, K. A. Jackson, M. R. Pederson, D. J. Singh, and C. Fiolhais, “Atoms, molecules, solids, and surfaces: Applications of the generalized gradient approximation for exchange and correlation”, Physical Review B **46**, 6671–6687 (1992).

[43] A. D. Becke, “Density-functional thermochemistry. III. The role of exact exchange”, The Journal of Chemical Physics **98**, 5648–5652 (1993).

[44] F. Aryasetiawan and O. Gunnarsson, “The $\boldsymbol{GW}$ method”, Reports on Progress in Physics **61**, 237–312 (1998).

[45] J. Korringa, “On the calculation of the energy of a Bloch wave in a metal”, Physica **13**, 392–400 (1947).

[46] W. Kohn and N. Rostoker, “Solution of the Schrödinger Equation in Periodic Lattices with an Application to Metallic Lithium”, Physical Review **94**, 1111–1120 (1954).

[47] J. L. Beeby, “The Density of Electrons in a Perfect or Imperfect Lattice”, Proceedings of the Royal Society A: Mathematical, Physical and Engineering Sciences **302**, 113–136 (1967).

[48] H. Shiba, “A Reformulation of the Coherent Potential Approximation and Its Applications”, Progress of Theoretical Physics **46**, 77–94 (1971).

[49] R. Zeller, P. H. Dederichs, B. Újfalussy, L. Szunyogh, and P. Weinberger, “Theory and convergence properties of the screened Korringa-Kohn-Rostoker method”, Physical Review B **52**, 8807–8812 (1995).

[50] B. Zimmermann, *Ab initio description of transverse transport due to impurity scattering in transition-metals*, Schriften des Forschungszentrums Jülich : Reihe Schlüsseltechnologien 89 (Forschungszentrum Jülich, Zentralbibliothek, Jülich, 2014).

[51] R. Zeller, “Projection potentials and angular momentum convergence of total energies in the full-potential Korringa–Kohn–Rostoker method”, Journal of Physics: Condensed Matter **25**, 105505 (2013).

[52] K. Wildberger, P. Lang, R. Zeller, and P. H. Dederichs, “Fermi-Dirac distribution in ab initio Green’s-function calculations”, Physical Review B **52**, 11502–11508 (1995).

[53] S. Heers, *Effect of spin-orbit scattering on transport properties of low-dimensional dilute alloys*, Schriften des Forschungszentrums Jülich Reihe Schlüsseltechnologien Bd. 31 (Forschungszentrum, Jülich, 2011).

[54] R. Zeller, “Multiple-scattering solution of Schrodinger’s equation for potentials of general shape”, Journal of Physics C: Solid State Physics **20**, 2347–2360 (1987).

[55] B. H. Drittler, *KKR-Greensche Funktionsmethode für das volle Zellpotential*, Berichte des Forschungszentrums Jülich (Forschungszentrum Jülich, 1991).

[56] R. Zalesny, M. G. Papadopoulos, P. G. Mezey, and J. Leszczynski, eds., *Linear-Scaling Techniques in Computational Chemistry and Physics* (Springer Netherlands, Dordrecht, 2011).

[57] E. Prodan and W. Kohn, “Nearsightedness of electronic matter”, Proceedings of the National Academy of Sciences **102**, 11635–11638 (2005).

[58] Y. Wang, G. M. Stocks, W. A. Shelton, D. M. C. Nicholson, Z. Szotek, and W. M. Temmerman, “Order-N Multiple Scattering Approach to Electronic Structure Calculations”, Physical Review Letters **75**, 2867–2870 (1995).

[59] D. R. Bowler and T. Miyazaki, “O(N) methods in electronic structure calculations”, Reports on Progress in Physics **75**, 036503 (2012).

[60] V. Rokhlin, “Rapid solution of integral equations of classical potential theory”, Journal of Computational Physics **60**, 187–207 (1985).

[61] D. G. Anderson, “Iterative Procedures for Nonlinear Integral Equations”, Journal of the ACM **12**, 547–560 (1965).

[62] Y. Saad, *Iterative methods for sparse linear systems*, 2nd ed (SIAM, Philadelphia, 2003).

[63] R. W. Freund and N. M. Nachtigal, “QMR: a quasi-minimal residual method for non-Hermitian linear systems”, Numerische Mathematik **60**, 315–339 (1991).

[64] M. Bolten, A. Thiess, I. Yavneh, and R. Zeller, “Preconditioning systems arising from the KKR Green function method using block-circulant matrices”, Linear Algebra and its Applications **436**, 436–446 (2012).

[65] N. M. Nachtigal, W. A. Shelton, and G. M. Stocks, *Combining the QMR method with first principles electronic structure codes*, tech. rep. ORNL/TM-12873 (1994).

[66] R. Zeller, “Towards a linear-scaling algorithm for electronic structure calculations with the tight-binding Korringa–Kohn–Rostoker Green function method”, Journal of Physics: Condensed Matter **20**, 294215 (2008).

[67] *Top 500 List (see www.top500.org).*

[68] P. F. Baumeister, M. Bornemann, M. Bühler, T. Hater, B. Krill, D. Pleiter, and R. Zeller, “Addressing Materials Science Challenges Using GPU-accelerated POWER8 Nodes”, in *Euro-Par 2016: Parallel Processing*, Vol. 9833, edited by P.-F. Dutot and D. Trystram (Springer International Publishing, Cham, 2016), pp. 77–89.

[69] C. McClanahan, *History and Evolution of GPU Architecture*, tech. rep. (2010).

[70] “IEEE Standard for Binary Floating-Point Arithmetic”, (1985).

[71] S. Gupta, *What Is NVLink? And How Will It Make the World’s Fastest Computers Possible?*

[72] *Whitepaper: NVIDIA’s Next Generation CUDA Compute Architecture: Kepler GK110/210.*

[73] *cuSPARSE Documentation (see docs.nvidia.com/cuda/cusparse).*

[74] G. M. Amdahl, “Validity of the Single Processor Approach to Achieving Large Scale Computing Capabilities”, in Proceedings of the April 18-20, 1967, Spring Joint Computer Conference, AFIPS ’67 (Spring) (1967), p. 483.

[75] *The MPI Forum: The Message Passing Interface (MPI) (see mpi-forum.org/docs).*

[76] *OpenMP Application Program Interface, Version 4.5 (see openmp.org).*

[77] *CUDA Documentation (see docs.nvidia.com/cuda).*

[78] D. Goldberg, “What every computer scientist should know about floating-point arithmetic”, ACM Computing Surveys **23**, 5–48 (1991).

[79] N. Whitehead and A. Fit-Florea, *Precision & Performance: Floating Point and IEEE 754 Compliance for NVIDIA GPUs*, tech. rep. (2011).

[80] D. Brömmel, W. Frings, and B. J. N. Wylie, *JUQUEEN Extreme Scaling Workshop 2017*, tech. rep. (2017), 47 pp.

[81] H. Ebert, H. Freyer, and M. Deng, “Manipulation of the spin-orbit coupling using the Dirac equation for spin-dependent potentials”, Physical Review B **56**, 9454–9460 (1997).

[82] T. Takeda, “The scalar relativistic approximation”, Zeitschrift für Physik B Condensed Matter and Quanta **32**, 43–48 (1978).

[83] J. Zabloudil, R. Hammerling, P. Weinberger, L. Szunyogh, M. Cardona, P. Fulde, K. von Klitzing, H.-J. Queisser, R. Merlin, and H. Störmer, eds., *Electron Scattering in Solid Matter*, Vol. 147, Springer Series in Solid-State Sciences (Springer Berlin Heidelberg, Berlin, Heidelberg, 2005).

[84] R. Zeller, “Dirac Green function for angular projection potentials”, Journal of Physics: Condensed Matter **27**, 465201 (2015).

[85] S. Blügel, ed., *Topological matter - topological insulators, skyrmions and majoranas lecture notes of the 48th IFF Spring School 2017* (2017).

[86] J. E. Hirsch, “Spin Hall Effect”, Physical Review Letters **83**, 1834–1837 (1999).

[87] L. Szunyogh, B. Lazarovits, L. Udvardi, J. Jackson, and U. Nowak, “Giant magnetic anisotropy of the bulk antiferromagnets IrMn and IrMn 3 from first principles”, Physical Review B **79**, 020403(R) (2009).

[88] D. C. Langreth and J. P. Perdew, “Theory of nonuniform electronic systems. I. Analysis of the gradient approximation and a generalization that works”, Physical Review B **21**, 5469–5493 (1980).

[89] J. P. Perdew, “Generalized gradient approximations for exchange and correlation: A look backward and forward”, Physica B: Condensed Matter **172**, 1–6 (1991).

[90] Y. Wang and J. P. Perdew, “Spin scaling of the electron-gas correlation energy in the high-density limit”, Physical Review B **43**, 8911–8916 (1991).

[91] M. Gell-Mann and K. A. Brueckner, “Correlation Energy of an Electron Gas at High Density”, Physical Review **106**, 364–368 (1957).

[92] M. Levy, “Asymptotic coordinate scaling bound for exchange-correlation energy in density-functional theory”, International Journal of Quantum Chemistry **36**, 617–619 (2009).

[93] C. Bowen, G. Sugiyama, and B. J. Alder, “Static dielectric response of the electron gas”, Physical Review B **50**, 14838–14848 (1994).

[94] E. H. Lieb and S. Oxford, “Improved lower bound on the indirect Coulomb energy”, International Journal of Quantum Chemistry **19**, 427–439 (1981).

[95] P. Lloyd, “Wave propagation through an assembly of spheres: II. The density of single-particle eigenstates”, Proceedings of the Physical Society **90**, 207–216 (1967).

[96] R. Zeller, “Improving the charge density normalization in Korringa–Kohn–Rostoker Green-function calculations”, Journal of Physics: Condensed Matter **20**, 035220 (2008).

[97] R. Zeller, “An elementary derivation of Lloyd s formula valid for full-potential multiple-scattering theory”, Journal of Physics: Condensed Matter **16**, 6453–6468 (2004).

[98] D. Ielmini and R. Waser, eds., *Resistive switching: from fundamentals of nanoionic redox processes to memristive device applications* (Wiley-VCH Verlag GmbH & Co. KGaA, Weinheim, 2016).

[99] K. Krieger, J. K. Dewhurst, P. Elliott, S. Sharma, and E. K. U. Gross, “Laser-Induced Demagnetization at Ultrashort Time Scales: Predictions of TDDFT”, Journal of Chemical Theory and Computation **11**, 4870–4874 (2015).

[100] M. Stamenova, J. Simoni, and S. Sanvito, “Role of spin-orbit interaction in the ultrafast demagnetization of small iron clusters”, Physical Review B **94** (2016).

[101] V. P. Antropov, M. I. Katsnelson, B. N. Harmon, M. van Schilfgaarde, and D. Kusnezov, “Spin dynamics in magnets: Equation of motion and finite temperature effects”, Physical Review B **54**, 1019–1035 (1996).

[102] O. Eriksson, A. Bergman, L. Bergqvist, and J. Hellsvik, *Atomistic spin dynamics: foundations and applications*, First edition (Oxford University Press, Oxford, 2017).

[103] J. P. Chico Carpio, *Magnetization dynamics on the nanoscale : From first principles to atomistic spin dynamics*, Digital Comprehensive Summaries of Uppsala Dissertations from the Faculty of Science and Technology (2016).

[104] T. Gilbert, "Classics in Magnetics A Phenomenological Theory of Damping in Ferromagnetic Materials", IEEE Transactions on Magnetics **40**, 3443–3449 (2004).

[105] I. Dzyaloshinsky, "A thermodynamic theory of "weak" ferromagnetism of antiferromagnetics", Journal of Physics and Chemistry of Solids **4**, 241–255 (1958).

[106] T. Moriya, "Anisotropic Superexchange Interaction and Weak Ferromagnetism", Physical Review **120**, 91–98 (1960).

[107] A. Liechtenstein, M. Katsnelson, V. Antropov, and V. Gubanov, "Local spin density functional approach to the theory of exchange interactions in ferromagnetic metals and alloys", Journal of Magnetism and Magnetic Materials **67**, 65–74 (1987).

[108] L. Udvardi, L. Szunyogh, K. Palotás, and P. Weinberger, "First-principles relativistic study of spin waves in thin magnetic films", Physical Review B **68**, 104436 (2003).

[109] H. Ebert and S. Mankovsky, "Anisotropic exchange coupling in diluted magnetic semiconductors: *Ab initio* spin-density functional theory", Physical Review B **79**, 045209 (2009).

[110] J. F. DiTusa, S. B. Zhang, K. Yamaura, Y. Xiong, J. C. Prestigiacomo, B. W. Fulfer, P. W. Adams, M. I. Brickson, D. A. Browne, C. Capan, Z. Fisk, and J. Y. Chan, "Magnetic, thermodynamic, and electrical transport properties of the noncentrosymmetric B 20 germanides MnGe and CoGe", Physical Review B **90**, 144404 (2014).

[111] A. Fert, V. Cros, and J. Sampaio, "Skyrmions on the track", Nature Nanotechnology **8**, 152–156 (2013).

[112] D. Castelvecchi, "The strange topology that is reshaping physics", Nature **547**, 272–274 (2017).

[113] N. Nagaosa and Y. Tokura, "Topological properties and dynamics of magnetic skyrmions", Nature Nanotechnology **8**, 899–911 (2013).

[114] E. Feldtkeller, "Continuous and Singular Micromagnetic Configurations", IEEE Transactions on Magnetics **53**, 1–8 (2017).

[115] F. N. Rybakov, A. B. Borisov, S. Blügel, and N. S. Kiselev, "New spiral state and skyrmion lattice in 3d model of chiral magnets", New Journal of Physics **18**, 045002 (2016).

[116] N. Kanazawa, Y. Onose, T. Arima, D. Okuyama, K. Ohoyama, S. Wakimoto, K. Kakurai, S. Ishiwata, and Y. Tokura, “Large Topological Hall Effect in a Short-Period Helimagnet MnGe”, Physical Review Letters **106**, 156603 (2011).

[117] S. V. Grigoriev, N. M. Potapova, S.-A. Siegfried, V. A. Dyadkin, E. V. Moskvin, V. Dmitriev, D. Menzel, C. D. Dewhurst, D. Chernyshov, R. A. Sadykov, L. N. Fomicheva, and A. V. Tsvyashchenko, “Chiral Properties of Structure and Magnetism in Mn1-xFexGe Compounds: When the Left and the Right are Fighting, Who Wins?”, Physical Review Letters **110**, 207201 (2013).

[118] N. Martin, M. Deutsch, F. Bert, D. Andreica, A. Amato, P. Bonfà, R. De Renzi, U. K. Rößler, P. Bonville, L. N. Fomicheva, A. V. Tsvyashchenko, and I. Mirebeau, “Magnetic ground state and spin fluctuations in MnGe chiral magnet as studied by muon spin rotation”, Physical Review B **93**, 174405 (2016).

[119] A. Yaouanc, P. Dalmas de Réotier, A. Maisuradze, and B. Roessli, “Magnetic structure of the MnGe helimagnet and representation analysis”, Physical Review B **95**, 174422 (2017).

[120] O. L. Makarova, A. V. Tsvyashchenko, G. Andre, F. Porcher, L. N. Fomicheva, N. Rey, and I. Mirebeau, “Neutron diffraction study of the chiral magnet MnGe”, Physical Review B **85**, 205205 (2012).

[121] U. K. Rößler, “Ab initio study on magnetism and pressure-induced transitions in cubic MnGe”, Journal of Physics: Conference Series **391**, 012104 (2012).

[122] K. Koepernik and H. Eschrig, “Full-potential nonorthogonal local-orbital minimum-basis band-structure scheme”, Physical Review B **59**, 1743–1757 (1999).

[123] S. H. Vosko, L. Wilk, and M. Nusair, “Accurate spin-dependent electron liquid correlation energies for local spin density calculations: a critical analysis”, Canadian Journal of Physics **58**, 1200–1211 (1980).

[124] A. Chacon, L. Heinen, M. Halder, A. Bauer, W. Simeth, S. Mühlbauer, H. Berger, M. Garst, A. Rosch, and C. Pfleiderer, “Observation of two independent skyrmion phases in a chiral magnetic material”, Nature Physics (2018).

[125] N. Kanazawa, J. S. White, H. M. Rønnow, C. D. Dewhurst, D. Morikawa, K. Shibata, T. Arima, F. Kagawa, A. Tsukazaki, Y. Kozuka, M. Ichikawa, M. Kawasaki, and Y. Tokura, “Topological spin-hedgehog crystals of a chiral magnet as engineered with magnetic anisotropy”, Physical Review B **96**, 220414(R) (2017).

[126] S. V. Grigoriev, A. S. Sukhanov, and S. V. Maleyev, “From spiral to ferromagnetic structure in B20 compounds: Role of cubic anisotropy”, Physical Review B **91**, 224429 (2015).

[127] R. Skomski, *Simple Models of Magnetism.* (Oxford University Press, UK, Oxford, 2008).

[128] J. Trygg, B. Johansson, O. Eriksson, and J. M. Wills, “Total Energy Calculation of the Magnetocrystalline Anisotropy Energy in the Ferromagnetic 3d Metals”, Physical Review Letters **75**, 2871–2874 (1995).

[129] G. H. O. Daalderop, P. J. Kelly, and M. F. H. Schuurmans, “First-principles calculation of the magnetocrystalline anisotropy energy of iron, cobalt, and nickel”, Physical Review B **41**, 11919–11937 (1990).

[130] X. Wang, D.-s. Wang, R. Wu, and A. Freeman, “Validity of the force theorem for magnetocrystalline anisotropy”, Journal of Magnetism and Magnetic Materials **159**, 337–341 (1996).

[131] K. Binder and D. W. Heermann, *Monte Carlo simulation in statistical physics: an introduction*, 5. ed, Graduate texts in physics (Springer, Heidelberg, 2010).

[132] A. O. Leonov and M. Mostovoy, “Multiply periodic states and isolated skyrmions in an anisotropic frustrated magnet”, Nature Communications **6**, 8275 (2015).

[133] P. F. Bessarab, V. M. Uzdin, and H. Jónsson, “Method for finding mechanism and activation energy of magnetic transitions, applied to skyrmion and antivortex annihilation”, Computer Physics Communications **196**, 335–347 (2015).

[134] J. Gayles, F. Freimuth, T. Schena, G. Lani, P. Mavropoulos, R. A. Duine, S. Blügel, J. Sinova, and Y. Mokrousov, “Dzyaloshinskii-Moriya Interaction and Hall Effects in the Skyrmion Phase of Mn1-xFexGe”, Physical Review Letters **115**, 036602 (2015).

[135] M. J. Stolt, X. Sigelko, N. Mathur, and S. Jin, “Chemical Pressure Stabilization of the Cubic B20 Structure in Skyrmion Hosting Fe1–xCoxGe Alloys”, Chemistry of Materials **30**, 1146–1154 (2018).

[136] V. A. Chizhikov and V. E. Dmitrienko, “Multishell contribution to the Dzyaloshinskii-Moriya spiraling in MnSi-type crystals”, Physical Review B **88**, 214402 (2013).

[137] B. Lebech, J. Bernhard, and T. Freltoft, “Magnetic structures of cubic FeGe studied by small-angle neutron scattering”, Journal of Physics: Condensed Matter **1**, 6105–6122 (1989).

[138] K. Shibata, X. Z. Yu, T. Hara, D. Morikawa, N. Kanazawa, K. Kimoto, S. Ishiwata, Y. Matsui, and Y. Tokura, “Towards control of the size and helicity of skyrmions in helimagnetic alloys by spin–orbit coupling”, Nature Nanotechnology **8**, 723–728 (2013).

[139] S. Mankovsky, S. Wimmer, S. Polesya, and H. Ebert, “Composition-dependent magnetic response properties of Mn1-xFex Ge alloys”, Physical Review B **97**, 024403 (2018).

[140] R. J. Elliott, J. A. Krumhansl, and P. L. Leath, “The theory and properties of randomly disordered crystals and related physical systems”, Reviews of Modern Physics **46**, 465–543 (1974).

[141] T. Kikuchi, T. Koretsune, R. Arita, and G. Tatara, “Dzyaloshinskii-Moriya Interaction as a Consequence of a Doppler Shift due to Spin-Orbit-Induced Intrinsic Spin Current”, Physical Review Letters **116**, 247201 (2016).

Acknowledgements

I would like to thank Prof. Dr. Stefan Blügel for agreeing to be my supervisor and giving me the opportunity to write this PhD thesis at his institute. His strong believe in the KKR`nano` project as well as his valuable advice were a source of motivation, especially when there were things that did not work out as planned.

I am also indebted to Prof. Dr. Riccardo Mazzarello who agreed to examine this thesis as a second referee.

My sincere thanks goes to Dr. Rudolf Zeller for co-supervising this project. His admirable knowledge of theoretical physics in general and his unrivaled expertise in the KKR method in particular are indeed impressive. It was essential to my work that his door was always open to discuss ways of proceeding. There was hardly any meeting that I did not leave without feeling a bit wiser.

I wish to thank Dr. Sergii Grytsiuk for his collaboration on the B20 materials and the fruitful scientific exchange we had regarding this topic.

Dr. Manuel dos Santos Dias provided some very important ideas on how my investigations of magnetic materials could be steered and frequently made time for discussing results.

Dr. Rudolf Zeller, Prof. Dr. Peter H. Dederichs, Dr. Paul F. Baumeister, Dr. Jonathan Chico, Dr. Manuel dos Santos Dias, Dr. Imara Lima Fernandes, Dr. Sergii Grytsiuk, Prof. Dr. Phivos Mavropoulos and Dr. Robert O. Jones proofread a manuscript of this thesis and gave valuable feedback for which I am very grateful as it certainly led to some improvements.

During my time at the Peter Grünberg Institute I benefited a lot from the vast expertise that is concentrated at this place. Especially, Prof. Dr. Phivos Mavropolous, Prof. Dr. Samir Lounis, Dr. Nikolai Kiselev, Dr. Gustav Bihlmayer and Prof. Dr. Peter H. Dederichs often helped me to come up with new ideas.

I very often visited the office of Juba Bouaziz to seek advice related to the fields of magnetism and spintronics. The conversations with him helped to solve several issues that one naturally encounters during a PhD project.

Furthermore, I would like to thank Dr. Roman Kovacik, Dr. Bernd Zimmermann, Dr. Philipp Rüßmann and Markus Hoffmann for fruitful discussions.

I also thank Gideon Müller for providing the SPIRIT code and introducing it to me.

Dr. Robert O. Jones deserves credit for helping with the preparation of the successful computing time proposal for *Hazel Hen*.

During my first months in Jülich, Elias Rabel taught me the basics of KKR`nano` and I want to express my gratitude to him for this since it facilitated my subsequent work.

I would also like to mention our very helpful collaboration with the Jülich Supercomputing Centre, where Dr. Paul F. Baumeister and Thorsten Hater helped to future-proof KKR`nano`.

I wish to thank Ute Winkler for taking care of many administrative issues.

Apart from scientific activities, there are many current and former members of the institute that made my stay here more enjoyable. Among them are my office mate Dr. Imara Lima Fernandes as well as my former office mate Dr. Jeiran Jokar, Dr. Filipe Guimaraes, Dr. Julen Ibanez Azpiroz, Flaviano José Dos Santos, Marta Gibertini and Dr. Benedikt Schweflinghaus.

Furthermore, the computing time that was provided for this project on *Hazel Hen* in Stuttgart (project ID 44129) and *QPACE3* in Jülich is gratefully acknowledged.

Last but not least, I would like to thank my family for the constant support that allowed me to write this thesis in the first place.

Band / Volume 182
8^{th} Georgian-German School and Workshop in Basic Science
A. Kacharava (Ed.) erscheint nur als CD (2018)
ISBN: 978-3-95806-353-2

Band / Volume 183
Topological properties of complex magnets from an advanced *ab-initio* Wannier description
J.-P. Hanke (2018), xi, 173 pp
ISBN: 978-3-95806-357-0

Band / Volume 184
Translation Initiation with 70S Ribosomes: A Single Molecule Study
C. Remes (2018), iv, 113 pp
ISBN: 978-3-95806-358-7

Band / Volume 185
Scanning tunneling potentiometry at nanoscale defects in thin films
F. Lüpke (2018), iv, 144 pp (untersch. Pag.)
ISBN: 978-3-95806-361-7

Band / Volume 186
Inelastic neutron scattering on magnetocaloric compounds
N. Biniskos (2018), iii, 92 pp
ISBN: 978-3-95806-362-4

Band / Volume 187
Magnetic Order and Excitation in Frustrated Pyrochlore 5d - Transition Metal Oxides
E. Feng (2018), iv, 182 pp
ISBN: 978-3-95806-365-5

Band / Volume 188
Finite-Difference Time-Domain Simulations Assisting to Reconstruct the Brain's Nerve Fiber Architecture by 3D Polarized Light Imaging
M. Menzel (2018), ix, 296 pp
ISBN: 978-3-95806-368-6

Band / Volume 189
Characterization of the cell-substrate interface using surface plasmon resonance microscopy
E. M. Kreysing (2018), xiii, 260 pp
ISBN: 978-3-95806-369-3

Schriften des Forschungszentrums Jülich
Reihe Schlüsseltechnologien / Key Technologies

Band / Volume 190
Scattering! Soft, Functional and Quantum Materials
Lecture Notes of the 50th IFF Spring School 2019
11 – 22 March 2019, Jülich, Germany
ed. by M. Angst, T. Brückel, S. Förster, K. Friese, R. Zorn (2019),
ca 1000 pp
ISBN: 978-3-95806-380-8

Band / Volume 191
Absolute scale off-axis electron holography of thin dichalcogenide crystals at atomic resolution
F. Winkler (2019), xxiii, 187 pp
ISBN: 978-3-95806-383-9

Band / Volume 192
High-resolution genome and transcriptome analysis of *Gluconobacter oxydans* 621H and growth-improved strains by next-generation sequencing
A. Kranz (2019), III, 182 pp
ISBN: 978-3-95806-385-3

Band / Volume 193
Group IV (Si)GeSn Light Emission and Lasing Studies
D. Stange (2019), vi, 151 pp
ISBN: 978-3-95806-389-1

Band / Volume 194
Construction and analysis of a spatially organized cortical network model
J. Senk (2019), 245 pp
ISBN: 978-3-95806-390-7

Band / Volume 195
Large-scale Investigations of Non-trivial Magnetic Textures in Chiral Magnets with Density Functional Theory
M. Bornemann (2019), 143 pp
ISBN: 978-3-95806-394-5

Weitere ***Schriften des Verlags im Forschungszentrum Jülich*** unter
http://wwwzb1.fz-juelich.de/verlagextern1/index.asp

Schlüsseltechnologien / Key Technologies
Band / Volume 195
ISBN 978-3-95806-394-5

Mitglied der Helmholtz-Gemeinschaft

JÜLICH
Forschungszentrum